UNIVERSITY OF LIVERPOOL

Probing low energy particle production in neutrino interactions through the vertex activity in the Fine Grained Detector at the T2K experiment

Thesis submitted in accordance with the requirements of the University of Liverpool for the degree of Doctor in Philosophy by

Pratiksha Paudyal

Department of Physics,
Oliver Lodge Laboratory
University of Liverpool

March 2019

Abstract

The Tokai-to-Kamioka (T2K) experiment is a long baseline neutrino oscillation experiment based in Japan. An intense neutrino beam is directed over a 295 km baseline from J-PARC based in Tokai, on the east coast of Japan, and reaches Super-Kamiokande, the far detector, on the west coast of Japan. The neutrino beam is directed 2.5° off-axis, in order to produce a narrow-band beam, and also so that the peak of the neutrino energy distribution maximises the ν_μ disappearance probability of T2K.

This thesis describes the first T2K studies into low energy particle production in neutrino interactions within the Fine Grained Detectors at the Near Detector (ND280) via the Vertex Activity (VA) variable, a measure of energy deposited in a vertex region. The VA is the only way in which low energy particles produced in neutrino-nucleon interactions can be investigated at T2K, as well as other experiments, and is therefore a useful candidate to constrain low energy particle production in the ND280 during neutrino interactions.

A disagreement in data and MC at low VA regions was observed in the ν_μ CC0π sample, and this thesis explores the reasons behind the excess in broad detail. It is expected that the excess is due to a mismodelling of low energy protons in MC generators. This thesis investigates the sensitivity of the VA to additional protons added to MC and presents results of the optimal percentage of protons added to the final state in the MC to improve the discrepancy observed.

Declaration

For the channel swap analysis in the ECal calibration Chapter 5, the determination of the swaps was performed by a previous analyst but the process of implementing the swaps was work I was responsible for. For the bar-to-bar calibration in Chapter 5, I adapted a previously exisiting analysis to produce new constants.

The Vertex Activity analysis presented in Chapters 6 - 8 is my original work that has not been undergone by anyone else previously.

All work contained in this thesis that was not created by me has been properly cited and referenced.

Pratiksha Paudyal

Contents

List of Figures

List of Tables

Chapter 1

Introduction

The Standard Model (SM) of physics was developed in the early 1970s and has been the key to linking fundamental particles and their governing forces, however the SM does not describe the subatomic world in a foolproof manner. Neutrino physics which is the focus of this thesis, is a theory that needs to be developed beyond the SM, after neutrino oscillations were postulated and experimentally proven in the early 2000s. Chapter 2 will delve deeper into a history of neutrino physics, spanning from early days of postulation right through to discovery of the three neutrino flavours, and oscillations, as well as the future outlook of neutrino physics.

Chapter 3 will discuss neutrino-nucleon interactions and why it is crucial that our current understanding of the nuclear model is improved, as well as the limitations and future prospects of new models. Chapter 4 summarises the T2K (Tokai-to-Kamioka) experiment in Japan, including the near and far detector, beam and current status. Chapter 5 outlines the ECal calibration studies, including the mismapped channel swap analysis, as well as the bar-to-bar calibration. Chapter 6 is the start of the Vertex Activity (VA) analysis, beginning with a description of VA, moving onto a definition of the analysis and distributions. Chapter 7 discusses response functions and how they can be used to probe low energy production, Chapter 8 describes the proton VA analysis, including results and systematics, and finally Chapter 9 provides conclusions and an outlook to future VA work.

Chapter 2

Neutrino Oscillations

2.1 The Standard Model

The Standard Model (SM) of particle physics, developed in the early 1970s, is a unified theory of elementary particles and the forces that govern them; Figure 2.1 shows the currently understood SM. The SM predicts that particles are composed of a combination of 12 fundamental spin-$\frac{1}{2}$ particles, known as fermions, that can undergo interactions mediated by bosons, which are particles with integer spins. The interactions that are predicted by the SM are the: strong force, mediated by the gluon, weak force, mediated by the $W^{+/-}$ and Z^0 boson, and finally the electromagnetic force, mediated by the photon. There is a fourth interaction, known as the gravitational force, that is thought to be mediated by a spin-2 particle known as a Graviton, but this is not theorised by the SM. The final particle predicted by the SM, the Higgs boson, was discovered in 2012, at the Large Hadron Collider (LHC) at CERN [1].

Fermions can be separated into two distinct groups, known as quarks and leptons. There are 6 types of quarks, that can interact by any of the three forces, and can be categorised into up-type with a charge of $+\frac{2}{3}$e (where e is the absolute electron charge), and down-type quarks with a charge of $-\frac{1}{3}$e. The second group of fermions, known as leptons, do not interact via the strong interaction, and have a charge of -1e. Each fermion has a corresponding antiparticle with the opposite charge.

Neutrinos, which are the main topic of this thesis, do not strongly interact and are known as neutral leptons. There are 3 flavours of neutrinos (each with a corresponding antiparticle with the same mass): electron (anti)neutrino ($\nu_e/\bar{\nu}_e$), muon (anti)neutrino ($\nu_\mu/\bar{\nu}_\mu$), and tau (anti)neutrino ($\nu_\mu/\bar{\nu}_\tau$). The SM predicts that neutrinos do not have a mass, but as neutrinos can oscillate (which will be discussed in Section 2.7), this means that their mass and flavour eigenstates are different, therefore they must have a non-zero mass.

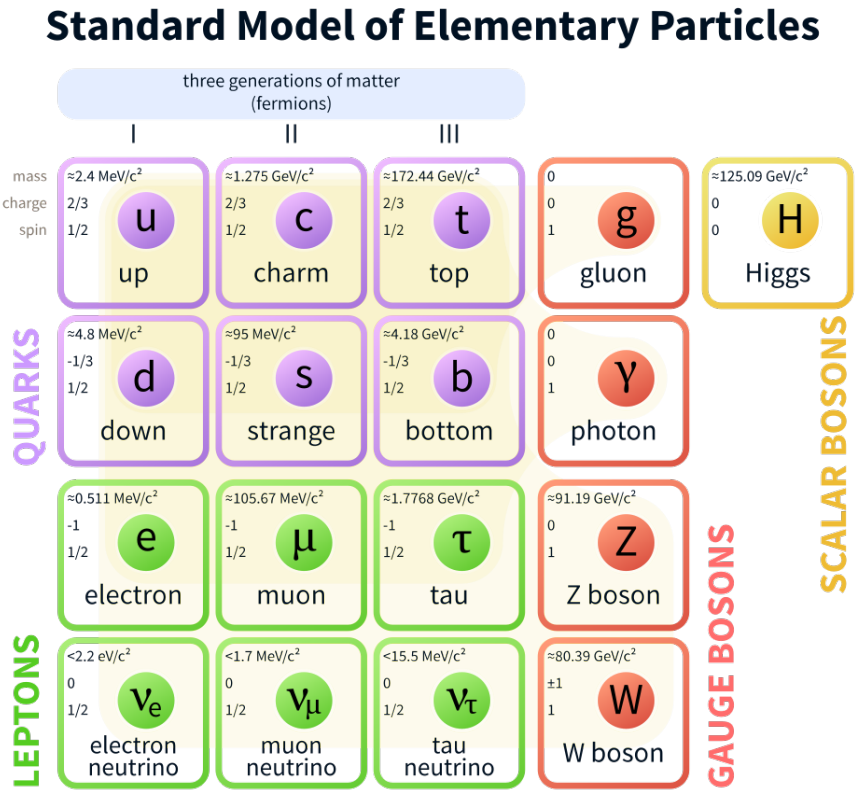

Figure 2.1: The Standard Model prediction for elementary particles of matter and their bosons [2].

The following section will discuss the history of the neutrino, from its early prediction, to the discovery of all neutrino flavour types, neutrino oscillations and finally to the present day understanding of the elusive particles.

2.2 The history of the neutrino

Weak interactions were first discovered in the late 1890s from radioactive decays by Henri Becquerel [3], and this was followed by Ernest Rutherford's discoveries of α and β in 1899 [4], with γ rays being discovered later. James Chadwick, in 1914 discovered that the electrons emitted in β-decay have a continuous energy spectrum [5]; this was contrasting to α and γ rays, which have a discrete spectra due to energy conservation.

In 1930, in order to remedy this momentum and energy conservation problem, as well as the issue of spin statistics in β-decay, Wolfgang Pauli postulated the existence of a weakly interacting, neutral fermion, called a neutron [6]. The neutron, as we know it today, was discovered in 1932 by Chadwick which led to Enrico Fermi renaming the Pauli particle, the neutrino. In 1934 Fermi formulated a theory of β-decay (Fermi Theory), which included the production of an electron-neutrino pair and a proton when a neutron decays [7], as a solution of momentum and energy conservation of β-decay

$$n \rightarrow p + e^- + \bar{\nu}. \tag{2.1}$$

It took more than two decades, in 1956, in order to observe this reaction, when Reines and Cowan developed the first reactor-neutrino experiment to measure
inverse β-decay

$$\bar{\nu}_e + p^+ \rightarrow e^+ + n \tag{2.2}$$

during which an antineutrino can produce a positron. Their setup used scintillator in a water tank, doped with cadmium chloride ($CdCl_2$) positioned by a nuclear reactor to detect antineutrino interactions. A definite signal for the interaction was observed via two γ-rays produced from e^+-e^- annihilation proceeding neutron capture on cadmium.

In 1962 at Brookhaven National Laboratory, L.M. Lederman, M. Schwartz, J. Steinberger et al. observed evidence of a second neutrino type, the muon neutrino, ν_μ, during the first accelerator neutrino experiment [8]. Protons with an energy of 15 GeV, were fired at a Be target to produce a beam of pions, which decayed to produce muons and muon neutrinos

$$\pi^+ \rightarrow \mu^+ + \nu_\mu. \tag{2.3}$$

In 1975, a third lepton flavour, tau, τ was discovered by M. Perl [9] at SPEAR, the $e^+ - e^-$ colliding ring. This led to the prediction of a third neutrino, tau neutrino, ν_τ, which was discovered in Fermilab in 2000 by the DONUT experiment [10]. A neutrino beam, formed using 800 GeV protons from the Fermilab Tevatron, passed through a three foot long DONUT target of iron plates sandwiched between layers of emulsion, which was used to locate and resolve decays. The τ leaves a track with a kink in the nuclear emulsion that indicates the decay of the tau lepton; Figure 2.2 shows the decay of the τ particle.

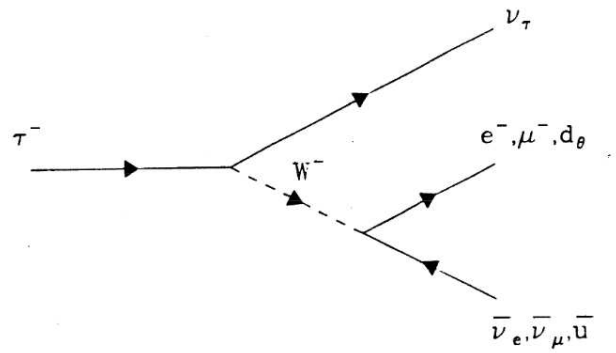

Figure 2.2: Feynman diagram for the decay of a tau, showing how tau neutrinos are produced [11].

Although the SM is consistent with the presence of 3 light active neutrino flavours, postulations regarding a fourth neutrino type have been made. Light sterile neutrinos were introduced to explain the experimental anomaly detected at The Liquid Scintillator Neutrino Detector (LSND) in Los Alamos in the 1990s [12]. LSND observed an excess in events for the $\nu_\mu \rightarrow \nu_e$ oscillation search which led to the construction of the Mini Booster Neutrino Experiment (MiniBooNE) at Fermilab [13]; MiniBooNE began taking data in 2002. MiniBooNE has recently published results [14], which are consistent with the LSND results by suggesting an excess in ν_e events, however these results have been controversial, and previous results from other experiments disagree with both LSND and MiniBooNE.

2.3 Solar Neutrinos

The Sun is a source of electron neutrinos with energy of the order $\sim$ 1 MeV, produced in the thermonuclear fusion reactions in the solar core. The solar neutrino flux on the Earth is around 6 x 10^{20} $cm^{-2}s^{-1}$ but solar neutrinos mainly pass by unnoticed, as they have a small neutrino interaction cross section, resulting in the requirement of large detectors placed underground to detect them.

Homestake and the Solar Neutrino Problem

The Homestake experiment [15], located in South Dakota and led by Ray Davis in the late 1960s, was the first to detect solar neutrinos, specifically ν_e from the sun, through the Pontecorvo-Alvarez inverse β-decay process

$$\nu_e + {}^{37}Cl \rightarrow {}^{37}Ar + e^-. \tag{2.4}$$

The experiment used a large cylindrical steel tank containing 615 tonnes of tetrachloroethylene, C_2Cl_4, in order to count the number of ^{37}Ar atoms produced by solar neutrinos through the Cl-Ar reaction. The initial data from Homestake found a neutrino flux value much less than the rate predicted by the Standard Solar Model (SSM),[1] of less than 3 Solar Neutrino Units (SNU), where 1 SNU = 10^{-36} events $atom^{-1}s^{-1}$. Davis et al. continued to take data at Homestake for over 25 years, but still found the solar neutrino rate to be around a third of that predicted by Bachall. This discrepancy between the predicted and observed rates of neutrinos produced in the sun is known as the Solar Neutrino Problem (SNP).

The energy spectra of neutrino fluxes from the pp chain [2], is shown in Figure 2.3, and the top label shows which experiments are sensitive to the particular processes and energy ranges.

[1] The SSM is a model used to understand the physics of the sun, including the energy spectra of neutrino fluxes of the proton-proton cycle as shown by Figure 2.3. The SSMs used in neutrino physics have been largely developed by J. N. Bachall since 1962 [16].

[2] The thermonuclear reactions that power the Sun are known as the pp chain and the CNO cycle, which result in the conversion of 4 protons and 2 electrons into a ^{4}He nucleus and two ν_es

$$4p + 2e^- \rightarrow {}^4He + 2\nu_e + Q \tag{2.5}$$

where Q, the Q-value, is the thermal energy release of the process.

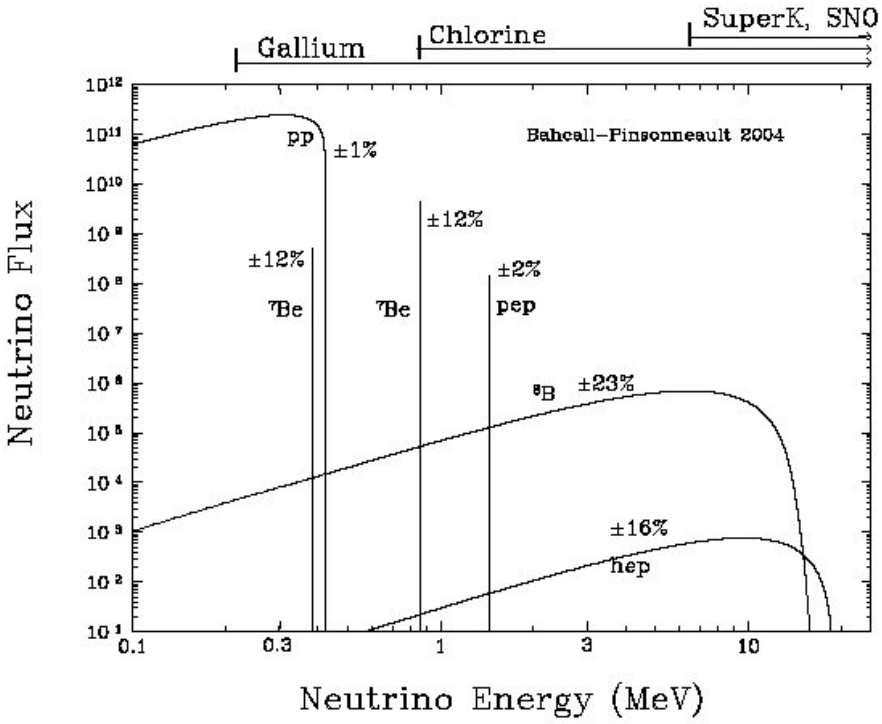

Figure 2.3: Energy spectra of neutrino fluxes from the pp chain as predicted by the SSM. It is clear to see the processes which are dominated by specific solar neutrino experiments [17].

Kamiokande

After Homestake, the Kamioka Nucleon Decay Experiment (Kamiokande) [18], a water Cherenkov experiment, was used to observe the most energetic ^{8}B solar neutrinos, at an energy of the order 10 MeV. The Kamiokande experiment, located 1 km underground in the zinc Kamioka mine in Japan, was a large cylindrical cavity containing around 3000 tonnes of water surrounded by 1000 PMTs. Kamiokande was originally built to detect nucleon decay but from 1987, Kamiokande detected ^{8}B solar neutrinos via the neutrino-electron elastic scattering reaction

$$\nu_e + e^- \rightarrow \nu_e + e^-. \tag{2.6}$$

The flux of ^{8}B solar neutrinos measured by Kamiokande was around half the SSM flux with a discrepancy of more than 2σ. The importance of the Kamiokande result was that although the missing solar neutrinos were unaccounted for, it was possible to reconstruct the directional correlation of the incoming neutrino and the Sun, via the recoil electron producing Cherenkov light; Figure 2.4 represents this. This means that the direction of the incident neutrinos can be determined and the signal from the sun can be identified clearly.

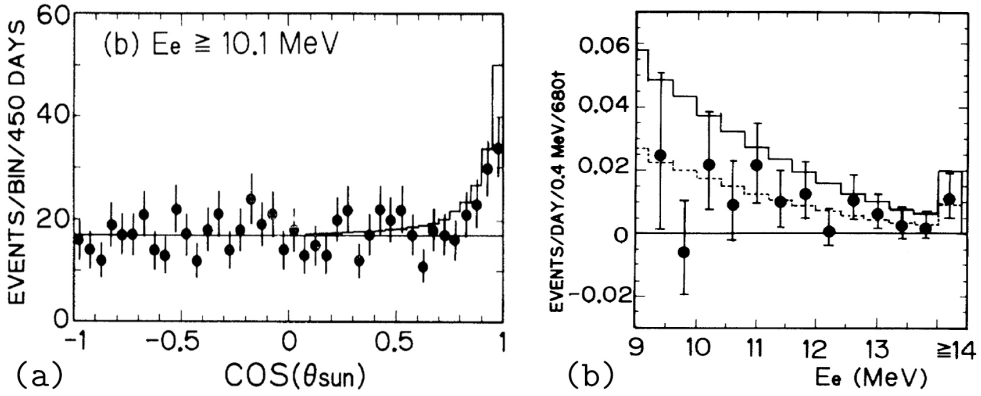

Figure 2.4: The ^{8}B solar neutrino results from the Kamiokande experiment. Kamiokande was able to reconstruct the directional information of the incoming neutrino [19].

Gallium Experiments

In the early 1990s, many gallium experiments were designed to measure the solar neutrino flux, including: the GALLium Experiment (GALLEX) [20] and its successor Gallium Neutrino Observatory (GNO) [21] and the Soviet-American Gallium Experiment (SAGE) [22]. The gallium experiments, crucially, are the only experiments sensitive to the solar flux of pp solar neutrinos (0 - 4.2 MeV), which are neutrinos produced at the start of the pp cycle

$$p + p \rightarrow^2 H + e^+ + \nu_e, \tag{2.7}$$

where 2 protons fuse into a deuteron, 99.76% of the time.

The gallium experiments can detect solar neutrinos via the inverse nuclear β decay of gallium

$$\nu_e +^{71} Ga \rightarrow^{71} Ge + e^-. \tag{2.8}$$

The gallium experiments rely on the atoms of ^{71}Ge to be extracted by chemical methods from large detectors, and combining the neutrino capture rate from all three experiments gives a value around half of the SSM prediction.

Super-Kamiokande

Super-Kamiokande (SK) [23], the successor to Kamiokande, is a 50 kton water Cherenkov detector, also located in the Kamiokande mine. SK initially began taking solar neutrino data from 1996-2001, again specifically searching for the most energetic ^{8}B solar neutrinos. SK found a flux rate of around half the SSM, thus confirming the solar neutrino deficit that was observed by Kamiokande and the gallium experiments.

SNO

In 2002, the Sudbury Neutrino Observatory (SNO) [24], a heavy-water [3] Cherekenkov detector located in the Creighton mine in Canada, observed high-energy ^{8}B solar neutrinos via charged-current (CC), neutral-current (NC) and elastic scattering (ES) reactions

$$\nu_e + d \rightarrow p + p + e^-(CC) \tag{2.9}$$

$$\nu_\alpha + d \rightarrow p + n + \nu_\alpha(NC) \tag{2.10}$$

$$\nu_\alpha + e^- \rightarrow \nu_\alpha + e^-(ES) \tag{2.11}$$

where α is e, μ, τ.

The CC reactions only occur for ν_e, allowing a measurement for the ν_e flux, whereas the NC reaction allows the measurement of ν_e, ν_μ and ν_τ, or in other words the total flux of neutrinos from the Sun. It is therefore possible to calculate the flux of ν_e separately from the total neutrino flux, and it was measured that the flux of solar ν_es were approximately three times smaller than the flux of ν_e, ν_μ and ν_τ. SNO showed that ν_es can change flavour to ν_μs and ν_τs, thus solving the SNP and also providing a key piece of evidence for neutrino oscillations.

Figure 2.5 shows the SNO result, in which the total neutrino flux summed over all flavours is consistent with the SSM prediction.

[3] The term heavy water is used to describe the target material used in the water for the SNO detector, D_2O consisting of a deuterium atom, ^{2}H, in contrast to the water previously used in Cherenkov detectors which contained a ^{1}H atom.

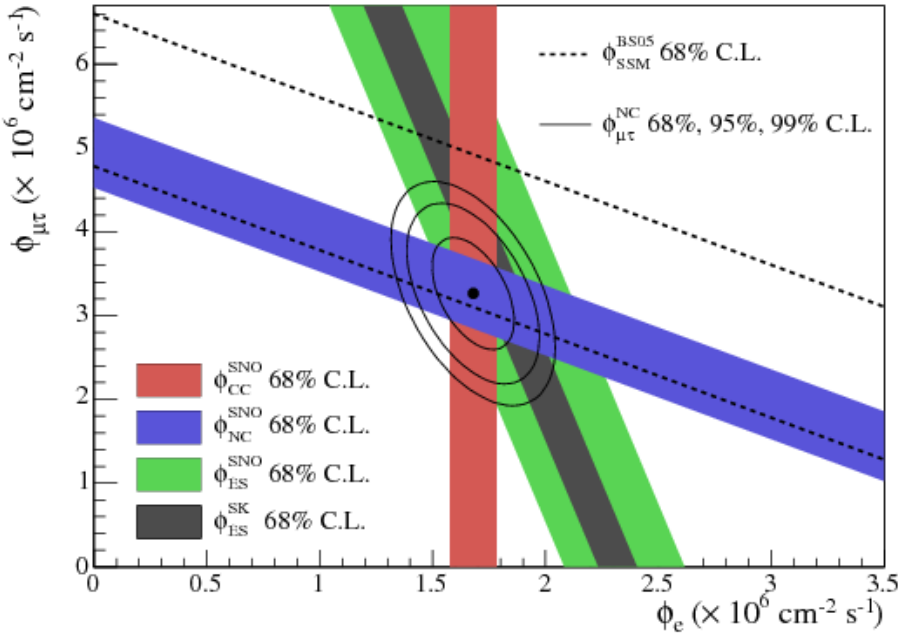

Figure 2.5: Muon neutrino and tau neutrino flux versus electron neutrino flux. The bands represent the charged current (red), neutral current (blue) and elastic scattering (light green) flux measurements. The total ^{8}B solar neutrino model as predicted by the standard solar model is shown as dashed lines [25].

2.4 Atmospheric Neutrinos

Atmospheric neutrinos occur when cosmic rays interact with nuclei in the upper atmosphere to produce π that decay to μ and ν_μ which then decay to e and ν_e. The atmospheric neutrinos with an energy range between 100 MeV to 100 GeV can be observed in underground detectors that contain sufficient shielding from cosmic rays. These experiments measure the neutrino flux as a ratio of

$$R \equiv \frac{\nu_\mu + \bar{\nu_\mu}}{\nu_e + \bar{\nu}_e} \tag{2.12}$$

where for low energies R $\simeq$ 2 but, for higher energies, R increases as muons reach the ground before they are able to decay.

Detection techniques of atmospheric neutrinos were theorised in the 1960s and initial observations were made in 1965 by detectors in the Kolar Gold Field Mine in South India [26] and in the East Rand Proprietary Gold Mine in South Africa [27]. In the late 1980s, Kamiokande observed atmospheric neutrinos [28] but initially considered them a background for nucleon decay searches. Kamiokande observed a deficit in muon-like events compared to predictions, but the electron-like events were in agree-

ment. This was followed by results from the Irvine-Michigan-Brookhaven (IMB) detector [29], located deep underground in a salt mine near Ohio in the USA, that were compatible with the "atmospheric neutrino anomaly" observed by Kamiokande.

In 1998, SK published a measurement of atmospheric muon neutrino disappearance [30], and a discrepancy in the number of muons passing upwards through the ground, compared to the number of muons observed passing downwards from the atmosphere was observed. This is known as the up-down asymmetry, in which the flux of atmospheric neutrinos is directionally correlated. Vertically down-going neutrinos are produced in the atmosphere above the detector and can travel for around 15 km before interacting, whereas up-going neutrinos can travel for around 13000 km through the Earth before detection. The most likely solution to the discrepancy observed by SK was to attribute the "missing" muon neutrinos to neutrino oscillations, and Figures 2.6 and 2.7 show the dependency of muon-like events on the function L/E. Figure 2.6 shows that for L/E below $\sim 10^2$ kmGeV^{-1} there is agreement with the MC prediction, as the neutrinos do not have enough time to oscillate, however for L/E $\geq$ 10^2 kmGeV^{-1} there is a deficit compared to the prediction as the oscillation phase is large enough for oscillations to occur. Similarly, for Figure 2.7, at high L/E there is a deficit in the atmospheric muon neutrino flux, consistent with neutrino oscillations.

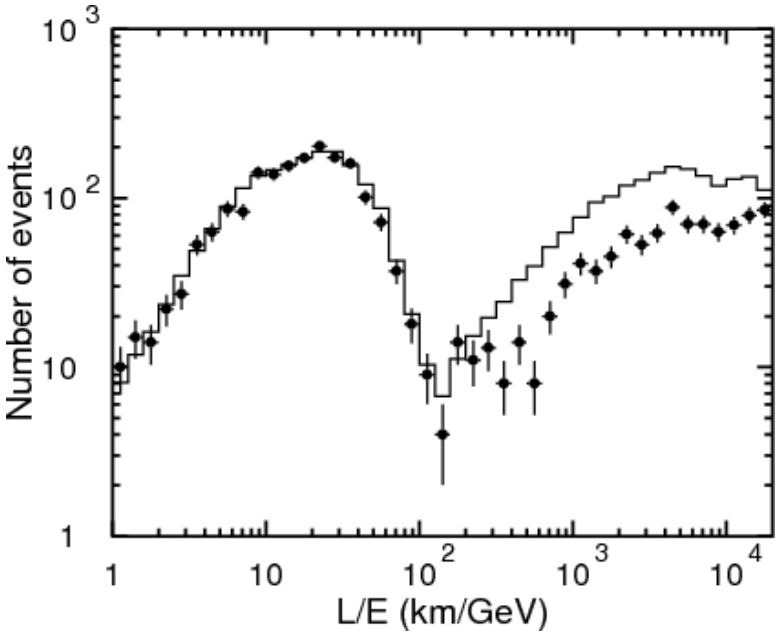

Figure 2.6: The number of μ-like events compared to the unoscillated prediction as a function of L/E at SK [31].

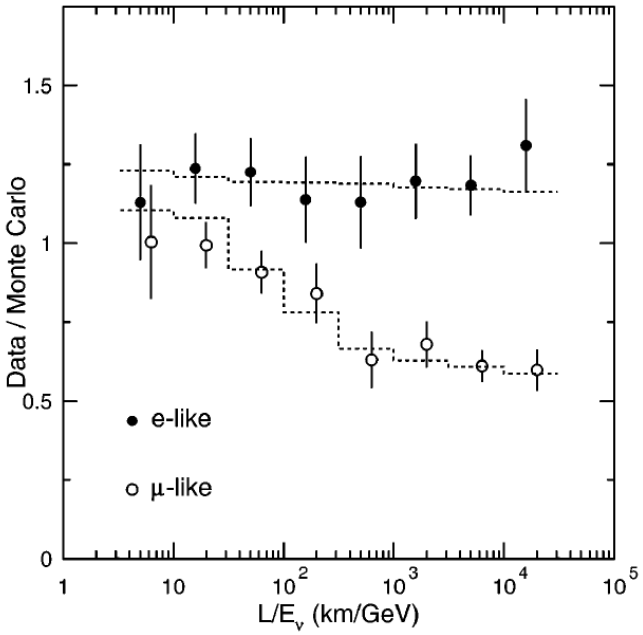

Figure 2.7: Results from SK showing the ratio of observed electron-like and muon-like events compared to the unoscillated MC prediction versus L/E. The dashed lines represent the expected shape for the $\nu_\mu \rightarrow \nu_\tau$ oscillation at Δm^2 = 2.2 x 10^{-3} eV^2 and $\sin^2 2\theta = 1$ [30].

2.5 Reactor Neutrinos

Reactor neutrinos are $\bar{\nu}_e$ produced via the inverse β-decay (Equation 2.2), originally detected by Reines and Cowan, as was discussed in Section 2.2. Neutrino oscillation experiments require an appropriate source-detector distance in order to observe oscillations, which causes an issue for reactor experiments, as although reactor antineutrinos have a low energy, the antineutrino flux decreases rapidly with distance, making it difficult to observe oscillations, and only $\bar{\nu}_e$ oscillations can be observed. This was an issue for short-baseline (SBL) reactor experiments, (L $\sim$ 10 - 100 m), and also long-baseline (LBL) experiments such as Chooz [32] and Palo Verde [33]; who were unable to observe $\bar{\nu}_e$ disappearance, but as the $\bar{\nu}_e$ disappearance channel is sensitive to the third mixing angle, (θ_{13}), Chooz was able to provide a limit on this angle.

The Kamioka Liquid scintillator AntiNeutrino Detector (KamLAND) [34] is located in the Kamioka mine, where Kamiokande was previously located, and consists of 1200 m^3 of liquid scintillator housed in a balloon-shaped volume. KamLAND was designed to measure electron antineutrinos produced by 53 nuclear power reactors in Japan, and from data collected between 2002 - 2004, KamLAND measured the disappearance of $\bar{\nu}_e$. Figure 2.8 shows the ratio of the observed $\bar{\nu}_e$ spectrum to the unoscillated prediction as a function of L/E, and there is quite clearly a variation in the ratio,

thus confirming the oscillation solution from the SNP.

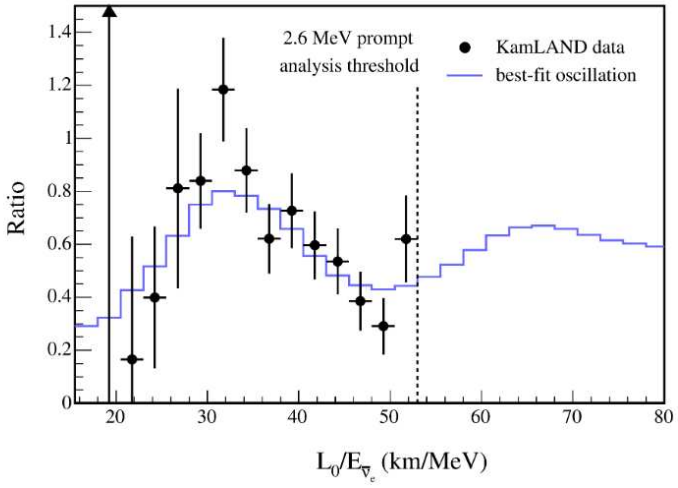

Figure 2.8: Results from KamLAND showing the ratio of $\bar{\nu}_e$ compared to the unoscillated prediction as a function of L/E. There is quite clearly a shape dependence on the ratio, which represents the disappearance and reappearance of $\bar{\nu}_e$ as a function of energy [34].

The more recent reactor neutrino experiments, Daya Bay [35] based in China, Double Chooz [36], the upgrade of the Chooz experiment, and Reactor Experiment for Neutrino Oscillation (RENO) [37], based in South Korea, were designed with further precision, and were able to rule out the hypothesis of no oscillations, and measure the best results of θ_{13}; Figure 2.9 shows the result from Daya Bay, where the ratio of the far and near spectra is in agreement with the oscillation prediction. The Jiangmen Underground Neutrino Observatory (JUNO) [38], a proposed medium baseline reactor neutrino experiment based in China, is likely to further improve the oscillation parameters, and is expected to commence data taking in 2020.

2.6 Accelerator Neutrinos

It is possible to create a high energy neutrino beam by colliding protons on a fixed nuclear target, which produces pions, that then decay and subsequently lead to muons and muon neutrinos; this procedure is the basis of accelerator experiments. Typically, there will be a ”near” detector close to the neutrino beam production, and a ”far” detector located at an ideal distance to probe the relevant neutrino oscillation parameters. The fact that the distance the neutrino travels, between the source and detector, is fixed, means that there is control over the neutrino energy, which leads to a reduction in the uncertainties due to cross sections. Accelerator neutrino experiments are sensitive to the atmospheric neutrino oscillation parameters via ν_μ disappearance (and ν_e

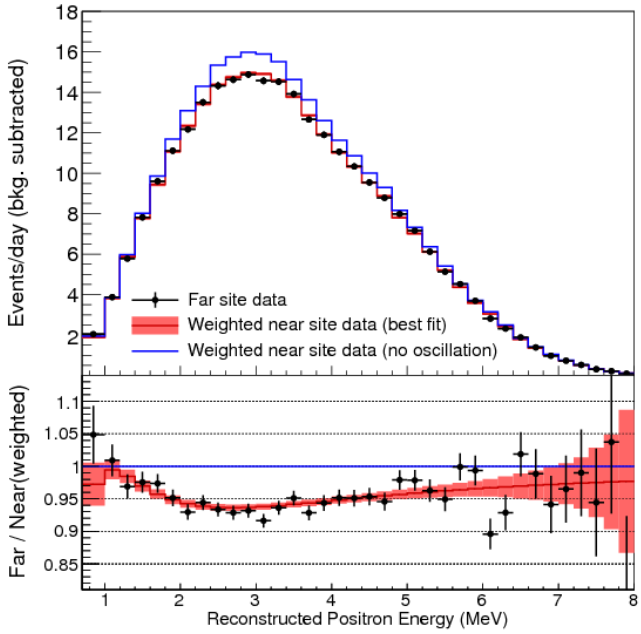

Figure 2.9: Result from Daya Bay, top plot shows the background subtracted positron energy (MeV) observed in the far site (black) and derived expectation of near site, in red (with oscillation) and blue (without oscillation). The bottom plot shows that the ratio of far and near spectra is consistent with that predicted for oscillation [39].

appearance) by measuring the θ_{13} mixing angle.

K2K [40], based in Japan was a long baseline accelerator experiment, with the neutrino source located in KEK and the far detector, 250 km away, in SK. K2K was the first accelerator experiment to observe muon neutrino disappearance in good agreement with neutrino atmospheric experiments, which provided confirmation of neutrino oscillations.

The Main Injector Neutrino Oscillation Search (MINOS) [41], ran from 2003 - 2012, and utilised the NuMI beam at Fermilab to produce muon neutrinos that were then detected by the Far Detector in the Soudan mine, 735 km away from the production target. MINOS confirmed muon neutrino disappearance in good agreement with the atmospheric neutrino observation, and further improved the oscillation parameters.

Tokai-to-Kamioka (T2K) [42], the first off-axis (the detector is shifted by a small angle from the axis of the beam) accelerator neutrino experiment has been collecting data since 2010. In July 2013, T2K was the first experiment to observe oscillations of ν_μ to ν_e [43]. T2K has also improved the precision in measurements of the oscillation parameters involved in ν_μ disappearance, Δm^2_{23} and θ_{23} [44]. The NuMI Off-Axis ν_e appearance (NOνA) experiment [45] uses the NuMI neutrino beam produced at Fer-

milab, and also utilises an off-axis configuration to study the appearance of electron neutrinos or antineutrinos. NOνA has been running since 2014, and has produced results that are in agreement with T2K but require further statistics.

Future proposed accelerator experiments include the Deep Underground Neutrino Experiment (DUNE) [46], in the USA, currently expected to take data in 2026, and Tokai-to-Hyper-Kamiokande (T2HK) [47], in which the far detector will be the upgrade to SK. The future accelerator experiments will look for further precision in oscillation parameters as well as searching for CP violation in neutrino oscillations.

2.7 Neutrino Oscillation Theory

Neutrino oscillations are a quantum-mechanical phenomenon whereby a neutrino can change its flavour whilst travelling through space. Neutrino oscillations were first proposed by Pontecorvo in 1957 [48], and his idea was considered to be very radical as neutrinos were required to have mass and at the time only one neutrino flavour had been observed. After the discovery of the second neutrino, the muon neutrino, Pontecorvo published a paper which included the $\nu_e \leftrightarrows \nu_\mu$ oscillation.

Neutrinos can interact via Charged Current (CC) and Neutral Current (NC) weak interactions, as shown by the Feynman diagrams in Figure 2.10, and their flavour eigenstates can couple via the weak interaction and be expressed as a superposition of three light neutrino mass eigenstates

$$|v_\alpha\rangle = \sum_{i=1}^{3} U_{\alpha i} |v_i\rangle \tag{2.13}$$

where α = e, μ, τ. $U_{\alpha i}$ is the Pontecorvo-Maki-Nakagawa-Sakata (PMNS) mixing matrix [49], parametrised by three mixing angles $(\theta_{12}, \theta_{13}, \theta_{23})$, and the charge-parity (CP) violating phase δ

$$U = \underbrace{\begin{pmatrix} 1 & 0 & 0 \\ 0 & c_{23} & s_{23} \\ 0 & -s_{23} & c_{23} \end{pmatrix}}_{Atmospheric} \begin{pmatrix} c_{13} & 0 & s_{13}e^{-i\delta} \\ 0 & 1 & 0 \\ -s_{13}e^{i\delta} & 0 & c_{13} \end{pmatrix} \underbrace{\begin{pmatrix} c_{12} & s_{12} & 0 \\ -s_{12} & c_{12} & 0 \\ 0 & 0 & 1 \end{pmatrix}}_{Solar} \tag{2.14}$$

$$= \begin{pmatrix} c_{12}c_{13} & s_{12}c_{13} & s_{13}e^{-i\delta} \\ -s_{12}c_{23} - c_{12}s_{23}s_{13}e^{i\delta} & c_{12}c_{23} - s_{12}s_{23}s_{13}e^{i\delta} & s_{23}c_{13} \\ s_{13}s_{23} - c_{12}c_{23}s_{13}e^{i\delta} & -c_{12}s_{23} - s_{12}c_{23}s_{13}e^{i\delta} & c_{23}c_{13} \end{pmatrix} \tag{2.15}$$

where $c_{ij} = cos(\theta_{ij})$ and $s_{ij} = sin(\theta_{ij})$.

In vacuum, the initial neutrino state at t=0 is given by

$$|\nu(t=0)\rangle = |\nu_\alpha\rangle = \sum_{k=1}^{3} U^*_{\alpha k}|\nu_k\rangle. \tag{2.16}$$

The temporal evolution of the flavour eigenstate is governed by Shrödindger's equation

$$i\frac{d}{dt}|\nu_\kappa(t)\rangle = H|\nu_\kappa(t)\rangle \tag{2.17}$$

where H is the Hamiltonian, and assuming the plane wave approximation

$$|\nu_\kappa(t)\rangle = e^{-iE_\kappa t}|\nu_\kappa\rangle. \tag{2.18}$$

The time evolution of the state is then

$$|\nu(x,t)\rangle = \sum_{i}^{3} U^*_{\alpha i} e^{-i(E_i t - p_i x)}|\nu_i\rangle \tag{2.19}$$

where E_i and p_i are the energy and momentum of a neutrino in the ith mass eigenstate.

The probability of a flavour eigenstate neutrino ν_α to transform to another flavour eigenstate ν_b is

$$P(\nu_\alpha \to \nu_b, t) = |A(\nu_\alpha \to \nu_b, t)|^2, \tag{2.20}$$

where A is the probability amplitude given by

$$A(\nu_\alpha \to \nu_b, t) = \langle\nu_b|\nu(t)\rangle = U^*_{\alpha k} e^{-iE_k t}\langle\nu_b|\nu_k\rangle = U_{bi}U^*_{\alpha k}e^{-iE_k t}\langle\nu_i|\nu_k\rangle = U_{bk}e^{-iE_k t}U^*_{\alpha k}. \tag{2.21}$$

Assuming the neutrino masses are very small or there is no mixing, and as neutrinos are relativistic, one can express the neutrino momentum as

$$p = \sqrt{E^2 - m^2} \sim E + \frac{m^2}{2E} \tag{2.22}$$

$$t \sim L \tag{2.23}$$

where E is the neutrino energy and L is the propagation distance, such that:

$$|\nu_{ij}(L)\rangle = exp\left(-i\frac{m_{ij}^2 L}{2E}\right)|\nu_{ij}(0)\rangle. \tag{2.24}$$

The general form of the neutrino oscillation probability is as follows

$$P_{\nu_\alpha \to \nu_\beta}(L,E) = \sum_{i,j=1}^{3} U_{\alpha i}^* U_{\beta i} U_{\alpha j} U_{\beta j}^* \exp\left(-i\frac{\Delta m_{ij}^2 L}{2E}\right), \tag{2.25}$$

where $\Delta m_{ij}^2 = m_j^2 - m_i^2$, the mass-squared differences:

$$\Delta m_{21}^2 = m_2^2 - m_1^2 \tag{2.26}$$

$$\Delta m_{31}^2 = m_3^2 - m_1^2. \tag{2.27}$$

Using the unitarity of matrix U, the probability can be expressed as:

$$\begin{aligned} P(\nu_\alpha \to \nu_b, t) \quad &= \quad \delta_{\alpha b} - 4\sum_{i>k} Re\left(U_{\alpha k}^* U_{bi} U_{\alpha i} U_{bk}^*\right) \sin^2\left(\frac{\Delta m^2 L}{4E}\right) + \\ &\quad + 2\sum_{i>k} Im\left(U_{\alpha k}^* U_{bi} U_{\alpha i} U_{bk}^*\right) \sin\left(\frac{\Delta m^2 L}{2E}\right). \end{aligned} \tag{2.28}$$

The final independent parameters are the mass-squared differences Δm_{23}^2 and Δm_{12}^2, and it is unknown whether m3 $>$ m2 $>$ m1, known as Normal Hierarchy (NH), or m2 $>$ m1 $>$ m3, known as Inverted Hierarchy (IH), shown by Figure 2.11.

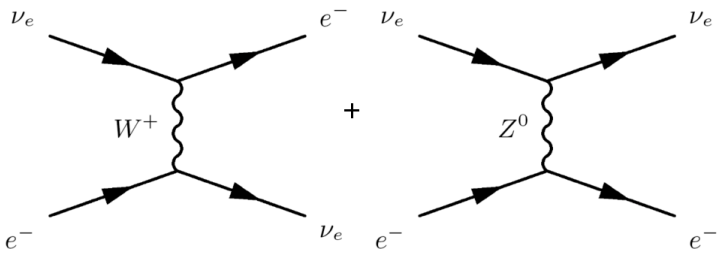

Figure 2.10: Feynman diagrams showing the Charged Current (CC) reaction (left) and Neutral Current (NC) reaction (right) of neutrinos with matter [50].

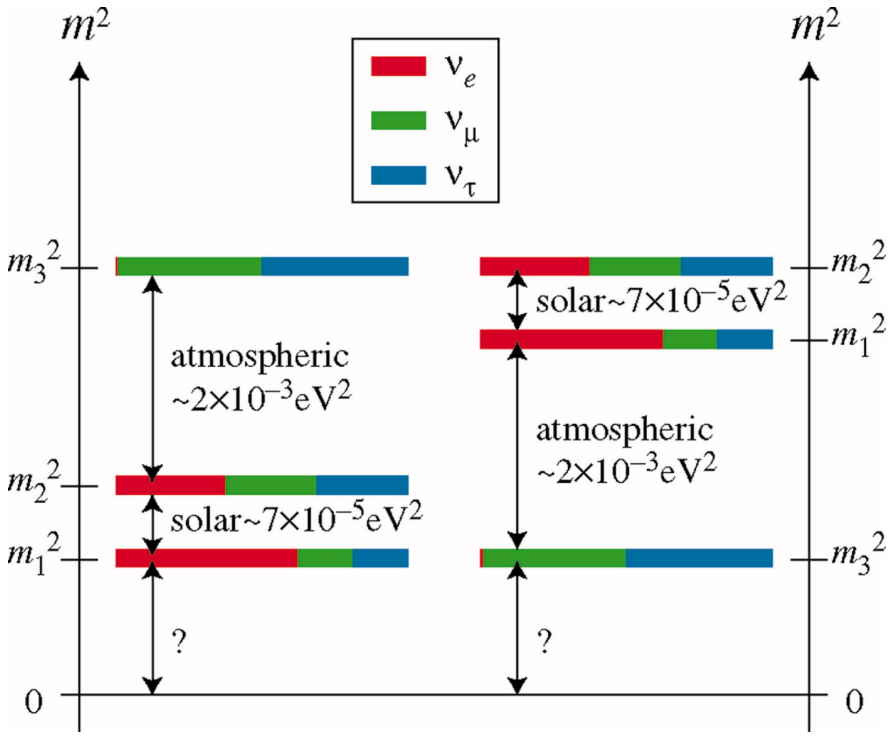

Figure 2.11: A schematic showing the normal (left) and inverted (right) mass hierarchies for the neutrino mass states. In NH the difference between m1 and m2 is much smaller than the difference between m2 and m3 [51].

The oscillation formulas can be simplified if we consider two-neutrino mixing instead, in which, only two massive neutrinos out of three are considered. This is beneficial as many experiments are not sensitive to three neutrino mixing and so can be analysed by a two neutrino model just as effectively.

The two neutrino mixing matrix is given by

$$U = \begin{pmatrix} cos\theta & sin\theta \\ -sin\theta & cos\theta \end{pmatrix} \tag{2.29}$$

where θ is the mixing angle and from this the probability of a neutrino oscillating from $\nu_\alpha \rightarrow \nu_\beta$ is given by

$$P(\nu_\alpha \rightarrow \nu_\beta) \approx sin^2 2\theta_{12} sin^2 \left(1.267 \frac{\Delta m^2_{12} L}{E} \frac{GeV}{eV^2 km} \right) \tag{2.30}$$

where Δm^2 is the mass square difference and gives the amplitude of the oscillations, eV^2, L is the distance travelled by the neutrino in km and E is the energy of the neutrino in GeV.

The oscillation length can be given by:

$$L^{OSC} = \frac{\pi E}{1.267 \Delta m^2_{12}}. \tag{2.31}$$

If $\frac{L}{L^{OSC}} \ll 1$ or if $\frac{L}{L^{OSC}} \gg 1$ then flavour oscillations cannot be measured, the only circumstance in which there is sensitivity to Δm^2 is when $\frac{L}{L^{OSC}} \sim 1$ as the neutrinos have time to oscillate at least once. Experimentally, L and E can be controlled in order to maximise the oscillation signal in the detector.

2.7.1 Current Status

The current best fit values for the oscillation parameters are given by Table 2.1:

Solar neutrino experiments and KamLAND are sensitive to the mass squared difference, Δm^2_{21}, and the mixing angle θ_{12}. The atmospheric parameters, Δm^2_{32} and θ_{23}, have been measured by SK, as well as MINOS, T2K and NOνA. The most precise measurement of θ_{13} comes from the reactor experiments Daya Bay, Double Chooz and Reno. Currently, there are no measurements for δ_{CP}, but T2K hints towards $\delta_{CP} = 0$ and $\delta_{CP} = \pi$ being excluded at a 90 % confidence level [53], [54]. Future experiments such as DUNE and HyperK aim to measure δ_{CP} to precise values.

Parameter	NH or IH	Best fit values
Δm^2_{21}[x10^{-5} eV^2]	-	7.53 ± 0.18
$\Delta m^2_{32(31)}$[x10^{-3} eV^2]	NH	2.51 ± 0.05
$\Delta m^2_{32(31)}$[x10^{-3} eV^2]	IH	-2.56 ± 0.04
$\sin^2\theta_{12}$	-	0.307 ± 0.013
$\sin^2\theta_{23}$	NH	0.425 ± 0.039
$\sin^2\theta_{23}$	IH	0.587 ± 0.038
$\sin^2\theta_{13}$	NH	0.02166 ± 0.00075
$\sin^2\theta_{13}$	IH	0.02179 ± 0.00076

Table 2.1: Best fit values for neutrino oscillation parameters, and where necessary Normal Hierarchy (NH), as well as Inverted Hierarchy (IH) values have been listed. These values have been adapted from [52].

Although the field of neutrino physics has produced many significant results over the past century, there are still some unknown questions:

- the value of δ_{CP}
- the sign of Δm^2_{32}
- the octant is unknown; does θ_{23} deviate from maximal mixing ($\theta_{23} = 45^\circ$), and if so, does it have a low-octant ($\theta_{23} < 45^\circ$) or a high-octant solution ($\theta_{23} > 45^\circ$)?
- the absolute value of the neutrino masses; $\Delta m^2_{31} \simeq \Delta m^2_{32} \geq 0$ (NH) or $\Delta m^2_{31} \simeq \Delta m^2_{32} \leq 0$ (IH)?
- are neutrinos Dirac particles or are they Majorana particles, in which case neutrinos are their own antiparticle?

In addition, measuring θ_{13}, θ_{12}, θ_{23}, Δm^2_{21} and Δm^2_{32} to higher precisions will be made possible by future neutrino experiments.

Chapter 3

Neutrino-nucleus interactions

As neutrino oscillation physics heads towards an era of high statistical precision, cross section uncertainties may soon become the main limiting factor in the precision of measurements of parameters (e.g. δ_{CP}, θ_{23}, Δm^2_{32}), therefore it is crucial to understand neutrino interactions and their cross sections. The uncertainties from the interactions between neutrinos and nucleons will be the main source of the systematic uncertainity in future experiments, so by an improved comprehension of the initial neutrino-nucleus interactions, as well as the final state interactions, future measurements can be improved.

This chapter will describe neutrino-nucleus interactions, giving a history to the interactions and past experiments, and how the interactions are measured experimentally at T2K and at future experiments. A discussion of the nuclear model will also be provided, along with a description of CCQE interactions and other interaction modes.

3.1 Neutrino-nucleus Scattering

Neutrino-nucleus scattering describes events in which a neutrino from a beam hits a target composed of "nucleons" and undergoes a particular type of scattering. The most likely interaction to occur at low neutrino energies is Elastic Scattering (ES), in which the energy transfer to the nucleus is not sufficient enough for an unbound nucleon to escape, and so the nucleus recoils in the same state as it was initially. Moving towards higher energies (E_ν $\sim$1 GeV), quasielastic (QE) scattering is most probable. In QE scattering, a nucleon will scatter off the nucleus and this can occur via a Neutral Current (NC), mediated by a Z boson, with no leptons in the final state, or via a Charged Current (CC) mediated by a $W^\pm$ boson, where there is a lepton in the final

state.

Figure 3.1 summarises the current measurements of CC neutrino and antineutrino cross sections, accumulated over many decades using different neutrino targets, for a full explanation of the experiments that contributed to the figure, the reader is referred to [50].

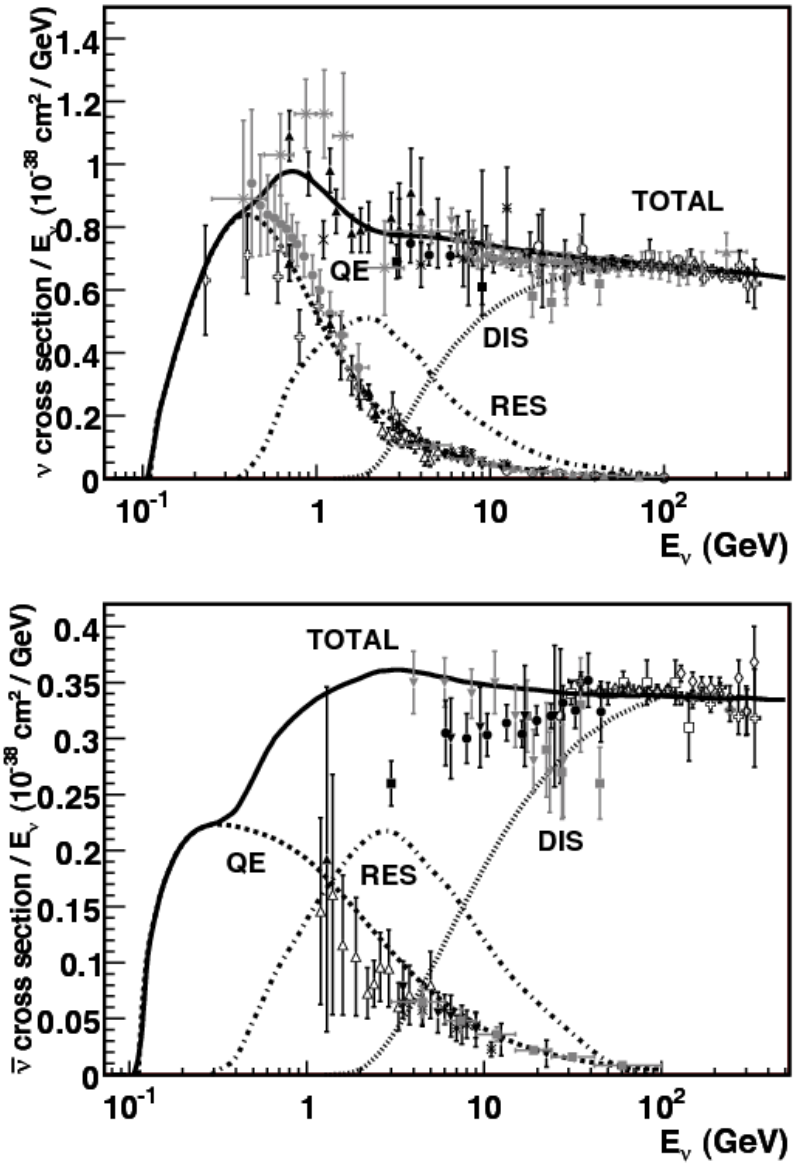

Figure 3.1: Total neutrino (top) and anti-neutrino (bottom) cross section as a function of neutrino energy, for current experimental data, separated by interaction mode: quasi-elastic (dashed), resonance (dot-dash) and deep inelastic scattering (dotted) [50].

The region of interest for T2K interactions is around 1 GeV where interactions mainly occur on nucleons and nuclei and, as Figure 3.1 shows, the main interaction channels are QE, as well as Resonance (RES). The RES processes peak at higher energies than the QE interaction mode. During a resonant process the target nucleon has enough energy to create a baryonic resonance (N^* or Δ), that will then decay to produce a final state consisting of nucleons and mesons. Figure 3.1 also shows that at E_ν >10 GeV, Deep inelastic scattering (DIS) interactions dominate, in which there is enough energy to resolve the inner structure of the nucleon. During DIS interactions, the neutrino is able to scatter directly off the quarks inside the nucelon.

In addition to the interactions described by Figure 3.1, there also exists coherent scattering, which occurs at low energies, where the neutrino will scatter off the whole nucleus. Finally this chapter will discuss multinucleon interactions, including two-body interactions (n particles - n holes, (np-nh)), during which a a weak boson is exchanged by a pair of nucleons, as well as Final State Interactions (FSI).

It should be noted, that it is not possible to measure the interactions themselves, instead the particles that leave the nucleus are measured. At T2K events are categorised using the topology information, where the contribution of each true interaction type is provided by the MC. The set of particles that leave the nucleus after the final state interaction within the target nucleus is defined as the topology. At T2K the topology observed for CCQE events is known as the CC0π topology, where the signal will include all neutrino interactions which do not produce a pion in the final state but also 2p2h contributions. The interactions in which a pion is absorbed before the final state could actually be CC1π events; T2K also defines these as a topology.

3.1.1 Nuclear Model

The nuclear model, which describes the initial state of nucleons within the nucleus, is used for simulation in Monte Carlo (MC) generators. MC generators work by using the input parameters to simulate a variety of neutrino interactions but discrepancies can arise in generator predictions for a single nucleon in the final state compared to what is measured by the data in the final state. There has been a great deal of interest recently in improving the nuclear models that describe the neutrino-nucleus interactions incorporated into MC generators and implementing these improved models will allow for the best measurements possible. At T2K, NEUT [55] is used as the default MC generator and GENIE [56],[57] is used as a cross-check. The simulations at T2K describe neutrino-nucleon interactions based on the “impulse approximation”, in which the total cross section is calculated as an incoherent sum of scattering on free nucleons.

The nuclear model was initially described in NEUT using the Spectral Function (SF) [58]. The SF model considers the nuclear matter to be a two-dimensional distribution of the nucleon momentum and binding energy, however disagreements between this model and experiments have led to a different model to be used instead. This model is the simplest impulse approximation approach and is known as the Global Relativistic Fermi Gas (RFG) model based on the Smith-Moniz model [59]. RFG describes the momentum of the nucleons as behaving flat, up until the the highest momentum nucleon, which has a Fermi momentum, p_F, the value of which depends on the size of the nucleus. The RFG model is now the default model used in NEUT, and GENIE uses a modified RFG model [60] to incorporate short range nucleon-nucleon correlations.

3.1.2 Charged Current Quasi-Elastic Scattering

Charged-Current Quasi-Elastic (CCQE) scattering (Figure 2.10 represents a CCQE reaction), mediated by a $W^{+/-}$ boson, is the primary way in which neutrinos interact with matter at T2K's peak energy range, around 600 MeV. The CCQE reaction involves a neutrino interacting with a neutron in the nucleus to produce a charged lepton and proton in the final state

$$\nu_l + n \rightarrow l^- + p \tag{3.1}$$

or similarly for an antineutrino

$$\bar{\nu}_l + p \rightarrow l^+ + n. \tag{3.2}$$

CCQE is modelled using a Llewellyn-Smith formalism [61] for both NEUT and GENIE, and the differential cross section is expressed as a function of the four momentum transfer squared (Q^2)

$$\frac{d\sigma^{\nu,\bar{\nu}}}{dQ^2} = \frac{M^2 G_F^2 \cos^2\theta_C}{8\pi E_\nu^2}\left(A(Q^2) \pm B(Q^2)\frac{s-u}{M^2} + C(Q^2)\frac{(s-u)^2}{M^4}\right), \tag{3.3}$$

where the sign in front of the B term represents neutrino (-) and antineutrino (+) scattering, M is the nucleon mass, G_F is the Fermi coupling constant, θ_c is the Cabbibo angle, E_ν is the neutrino energy and

$$s - u = 4ME_\nu - Q^2 - m_l^2, \tag{3.4}$$

where s and u are the Mandlestam kinematic variables corresponding to the centre of mass energy squared and the four momentum squared respectively.

The functions A, B and C are given by

$$A(Q^2) = \frac{m_l^2 + Q^2}{M^2}\left\{(1+\tau)F_A^2 - (1-\tau)\left(F_1^V\right)^2 + \tau(1-\tau)\left(F_2^V\right)^2 + 4\tau F_1^V F_2^V - \right.$$
$$\left. - \frac{m_l^2}{4M^2}\left(\left(F_1^V + F_2^V\right)^2 + (F_A + 2F_P)^2 - \left(\frac{Q^2}{M^2} + 4\right)F_P^2\right)\right\}, \quad (3.5)$$

$$B(Q^2) = \frac{Q^2}{M^2}F_A\left(F_1^V + F_2^V\right), \quad (3.6)$$

$$C(Q^2) = \frac{1}{4}\left(F_A^2 + \left(F_1^V\right)^2 + \tau\left(F_2^V\right)^2\right), \quad (3.7)$$

where m_l is lepton mass and τ is a constant, such that

$$\tau = \frac{Q^2}{4M^2}. \quad (3.8)$$

The vector form factors, F_1^V and F_2^V, can be defined in terms of the electromagnetic form factors of electron-nucleon scattering, as a consequence of the *conserved vector current* (CVC) hypothesis [62], and F_P is a pseudoscalar form factor that can be expressed as

$$F_P(Q^2) = \frac{2M^2}{Q^2 + m_\pi^2}F_A(Q^2), \quad (3.9)$$

where m_π is the mass of the pion, and the axial form factor, F_A is usually parameterised with a dipole form

$$F_A(Q^2) = \frac{g_A}{\left(1 + \frac{Q^2}{M_A^{QE2}}\right)^2}, \quad (3.10)$$

where g_A is known as the axial coupling constant, with a value of = - 1.2670 $\pm$ 0.0035, well known from neutron β decay [63], and M_A^{QE} is the axial mass term; for NEUT M_A = 1.21 GeV and for GENIE M_A = 0.99 GeV. Early investigations of the QE scattering date back to the early 1970s when bubble chamber experiments [64] employed deuterium as a nuclear target, and consequently led to initial nucleon form factor measurements. M_A^{QE} constrained from neutrino-deuterium scattering in bubble chamber experiments, was 1.026 $\pm$ 0.021 GeV [65]. Currently, with an improved analysis of the

original data and using updated vector form factors, $M_A^{QE} \sim 1.0$ GeV. The value of M_A changes the scale and shape of the Q^2 distribution and discrepancies have been observed with recent experiments and the bubble chamber results; this will be discussed further in Section 3.2.

3.1.3 Neutral Current Elastic Scattering

Neutral Current Elastic (NCE) processes are similar to CCQE, but are mediated by Z^0 bosons, and a neutrino and nucleon is produced in the final state, as shown below:

$$\nu_l + p \rightarrow \nu_l + p \tag{3.11}$$

$$\nu_l + n \rightarrow \nu_l + n. \tag{3.12}$$

As no lepton is present in the final state, it is difficult to detect these processes.

3.1.4 Resonant Pion Production

The resonant pion production process is dominant for neutrinos with energies around 1.5 GeV to 5 GeV, as shown by Figure 3.1. Resonant pion production processes occur when there is enough energy in a nucleon interaction to create a resonance state (N^* or Δ), that then decays to produce a pion. The single pion production in MC uses a Rein-Sehgal model [66], and the target nucleon can be a proton or a neutron.

Neutrino induced single pion production on nucleons can occur through three charged-current channels:

$$\nu_l + p \rightarrow l^- + \pi^+ + p \tag{3.13}$$

$$\begin{aligned} \nu_l + n &\rightarrow l^- + \pi^+ + n \\ &\quad l^- + \pi^0 + p \end{aligned} \tag{3.14}$$

and four neutral-current channels:

$$\begin{aligned} \nu_l + p &\rightarrow \nu_l + \pi^+ + n \\ &\quad \nu_l + \pi^0 + p \end{aligned} \tag{3.15}$$

$$\begin{aligned} \nu_l + n &\rightarrow \nu_l + \pi^0 + n \\ &\nu_l + \pi^- + p. \end{aligned} \tag{3.16}$$

3.1.5 Coherent Scattering

In a coherent neutrino-nucleus interaction, the neutrino will scatter (via a CC or NC) off the nucleus, but there will be no excitation or fragmentation involved, so the nucleus ends up in the same quantum state as it was initially.

The coherent neutrino-nucleus interaction is also modelled using the Rein-Seghal model and a Feynman diagram for the ν_μ coherent process is shown by Figure 3.2.

The coherent process for CC interactions can be expressed as:

$$\nu_l + A \rightarrow \nu_l + A + \pi^0 \tag{3.17}$$

$$\nu_l + A \rightarrow l^- + A + \pi^+ \tag{3.18}$$

where A is the target nucleus, and the neutrino that is produced will have a very low momentum.

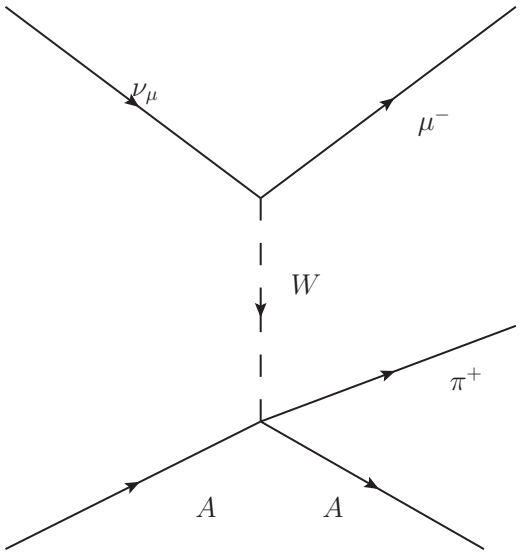

Figure 3.2: Feynman diagram of a CC coherent pion production.

3.1.6 Deep Inelastic Scattering processes

Deep Inelastic Scattering (DIS) processes dominate at high energies, Figure 3.1 shows that this occurs at $E_\nu > 5$ GeV, which is not in T2K's region of sensitivity. DIS occurs

when a neutrino is able to interact with a quark inside a nucleon through a $W^{+/-}$ boson (CC) or Z boson (NC), and can cause the nucleus to fragment and produce a jet of hadrons.

The DIS process can be expressed as:

$$\begin{aligned} \nu_l + N &\rightarrow l^- + X \\ \nu_l + X & \end{aligned} \tag{3.19}$$

$$\begin{aligned} \bar{\nu}_l + N &\rightarrow l^+ + X \\ \bar{\nu}_l + X & \end{aligned} \tag{3.20}$$

where X denotes the hadronic multiple particle system.

3.2 Multinucleon Processes

As experiments move towards nuclear targets that are more complex, a clear understanding of nuclear effects is paramount. External data gave constraints on cross section systematics, starting with bubble chamber experiments (as mentioned previously in Section 3.1.2), and this was followed by investigating lepton-nucleus QE scattering using electrons. The benefit of using electrons is that the properties, such as beam, flux, momentum, among others, are known to precise values, which means that the Q^2 and momentum transferred to the nucleus during an interaction can be precisely measured. In fact, as the form factors are similar to QE, the early electron scattering configurations have been adapted to describe neutrino data at T2K.

Following on from the bubble chamber results, K2K [67], and MiniBooNE [68] found a discrepancy in the absolute QE cross section as a function of energy, based on the standard value of M_A = 1.03 GeV/c^2. For the MiniBooNE results it was necessary to increase the M_A value to 1.35 GeV/c^2, in order to account for the discrepancy observed. It was inferred that there was a problem with the interaction model, and not the flux, as a similar issue is seen in the Q^2 distribution. SciBooNE was able to resolve the final state by identifying the proton track as well as the muon track [69], and this agreed with a higher M_A prediction, which is consistent with the MiniBooNE measurement. NOMAD [70], uses a 2-track event selection with a reconstructed proton track, and the cross section was measured with a best-fit M_A value of 1.05 GeV/c^2, consistent with the world average value. MINOS [71] observes similar shape disagreements as those seen in K2K, MiniBooNE and SciBooNE, and requires a larger M_A value.

The MINOS experiment uses a higher energy and an iron target instead of carbon. T2K has also published results consistent with a high effective M_A value [72].

Evaluating the results from all of these experiments suggests the presence of another interaction model, such as a multinucleon neutrino interaction model, in order to account for the discrepancy observed. Multinucleon processes, which are also known as np-nh[1], occur when a neutrino interacts with more than one nucleon. An example of such an interaction is, a pion produced via the excitation of a Δ resonance escaping detection due to reabsorption into the nucleus, simulating a QE interaction, but is in actual fact a multinucleon process. The cross section of np-nh processes are low and difficult to calculate, but have a significant effect in electron scattering experiments, shown by Figure 3.3.

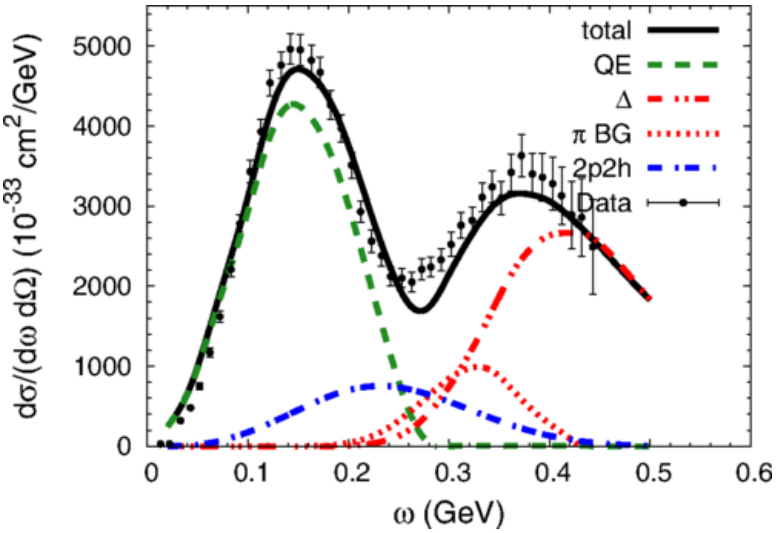

Figure 3.3: Inclusive cross section for electron scattering on carbon with $Q^2 = 0.24$ GeV^2 at the QE peak. The 2p2h interactions (blue) peak in the dip region inbetween the QE peak (green) and the resonance peak (red dash-dotted-dotted line) [73].

Multinucleon effects are being studied in more detail for neutrino scattering, and there are a number of different multinucleon models implemented into neutrino generators, including the one used in NEUT by Nieves et al. [74], which uses a many-body expansion to calculate the total lepton scattering. There is also the Martini et al. [75] model which uses a many-body expansion method as well, with alternative approximations. In addition, both Nieves and Martini require a correction to the nuclear model known as the Random Phase Approximation (RPA) [74]. RPA is a long-range correlation that considers the collective excitation of the nucleus and calculates this as a superposition of 1p1h excitations. Both Nieves and Martini have theorised that, a calculation based on a free local Fermi gas with RPA excitations and 2p2h interactions, can explain the

[1] 1p-1h stands for 1 particle-1 hole and 2p-2h stands for 2 particle-2 hole.

MiniBooNE data [76], [77].

Recent results from MINERνA have shown that for CCQE-like interactions, there is an excess in the energy deposited around the vertex, which can be attributed to an excess of protons in the final state [78], and is consistent with a multinucleon model. T2K has also recently seen results suggesting that multinucleon interactions are misidentified as CCQE events due to misreconstruction of events. In particular the focus of this thesis is a discrepancy observed between data and MC at low VA values for a muon neutrino CC0π sample, which may be explained using a multinucleon model, and will be discussed in further detail in Chapters 6-8.

3.3 Final State Interactions

Neutrino-nucleon interactions are often identified depending on the circumstances of the hadronic final state, which can be adjusted depending on Final State Interactions (FSI). It is difficult to define FSI but it is important to understand them as they can distort the topology and kinematics of nucleon interactions, and so are a significant source of error in cross section measurements. FSI are not able to isolate the initial interaction type, such that for example, a CCRES event in which a pion is absorbed by the nucleus, may look like a CCQE event, in which there is no exiting proton, and only the outgoing lepton will be observed.

NEUT uses a cascade model [55] to simulate FSI, in which the hadrons that are produced at the neutrino interaction vertex propagate through the nucleus step-by-step. GENIE also uses a cascade model, which is called hA, and more details can be found in [79].

In conclusion, the current understanding of multinucleon effects, as well as FSI, are limited but are important to understand as they could help explain the results from certain experiments, where the measured CCQE cross section is significantly higher than expected. Generators are limited in the understanding of these nuclear effects but it is crucial that the multinucleon interaction models as well as further models that can help explain the discrepancies observed in QE interactions, are implemented in event generators. In addition, future experiments that are sensitive to protons produced in a neutrino-nucleon interaction, including at the Fermilab Short Baseline Neutrino Program, where it may be possible to reconstruct low energy protons at the vertex of neutrino events [80], are necessary to help improve the current understanding of 1p1h and 2p2h interactions.

Chapter 4

The T2K Experiment

T2K (Tokai to Kamioka) is a long baseline neutrino oscillation experiment located at the Japan Proton Accelerator Research Complex (J-PARC) in Tokai, Japan. An intense ν beam is produced by the J-PARC accelerator on the east coast of Japan and is directed through a number of near detectors and a far detector, Super-Kamiokande (SK), located 295 km away from J-PARC (shown by Figure 4.1); the beam is directed 2.5°off-axis towards SK.

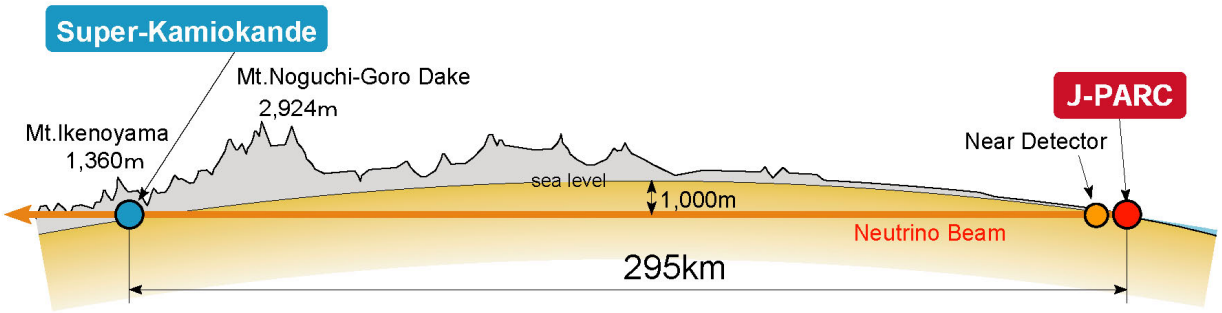

Figure 4.1: Illustration of the T2K beamline direction travelling from J-PARC to SK [42].

4.1 Motivations

The T2K experiment was designed with an emphasis on probing the last unknown lepton sector mixing angle θ_{13} by measuring the oscillation of $\nu_\mu \rightarrow \nu_e$ [81]. It has also investigated $\sin^2\theta_{23}$ and the mass difference Δm^2_{23} through ν_μ disappearance.

Since May 2014, T2K has been running in anti-neutrino mode to give sensitivities and constraints to the CP violation phase δ_{CP}. The sign of the CP-violating term is the

opposite for neutrino and antineutrino oscillations therefore antineutrino beam data allows CP violation effects to be studied directly. The T2K experiment is also involved in measurements of neutrino interaction cross sections and exotic physics such as sterile neutrino and Lorentz Violation searches.

4.2 Neutrino Beam

The T2K neutrino beam is produced at J-PARC and is obtained from the acceleration of protons. The following sections will discuss the J-PARC accelerator complex where the beam originates, as well as a detailed description of the neutrino beam production.

4.2.1 The J-PARC Accelerator

The J-PARC accelerator complex is located in Tokai, Ibaraki and consists of three accelerators: a linear accelerator (LINAC), a rapid-cycling synchrotron (RCS) and the main ring (MR) synchrotron, shown by Figure 4.2.

Figure 4.2: Birds-eye view of the J-PARC facility [82].

A H^- beam is accelerated by the LINAC to a kinetic energy up to 400 MeV and is stripped of electrons by thick carbon foils to be converted into a proton beam, H^+, which is then injected into the RCS and accelerated to 3 GeV. The RCS has a cycle fre-

quency of 25 Hz and contains two bunches in each cycle. Approximately 5% of these bunches are supplied to the MR, the rest of the beam is used in the muon and neutron beamline at J-PARC. The MR accelerates the protons to 30 GeV in a circumference of 1567 m. There are 8 bunches in the MR which are extracted for the neutrino beamline in a single turn.

4.2.2 ν Beamline

The T2K neutrino beamline is composed of a primary beamline and a secondary beamline, as shown by the schematic in Figure 4.3. The purpose of the primary beamline is to ensure the extracted protons from the MR are pointed in the direction of Kamioka where the far detector, SK, is based. The primary beamline consists of three sections: a 54 m preparation section, a 147 m arc section and finally a focusing section that is 37 m long. The extracted proton beam in the preparation section is focused and deflected by 11 magnets ready for the arc section. During the arc section the proton beam is directed towards the location of Kamioka; superconducting magnets bend the proton beam by 80.7°. The final focusing section helps guide the proton beam towards the target where it reaches the secondary beamline. The protons collide with a graphite target to create secondary pions, which are focused by magnetic horns and decay into neutrinos that form the T2K neutrino beam. The secondary beamline, shown by Figure 4.4, consists of three sections: the target station, decay volume and beam dump. The target station contains a collimator, optical transition radiation monitor (OTR),

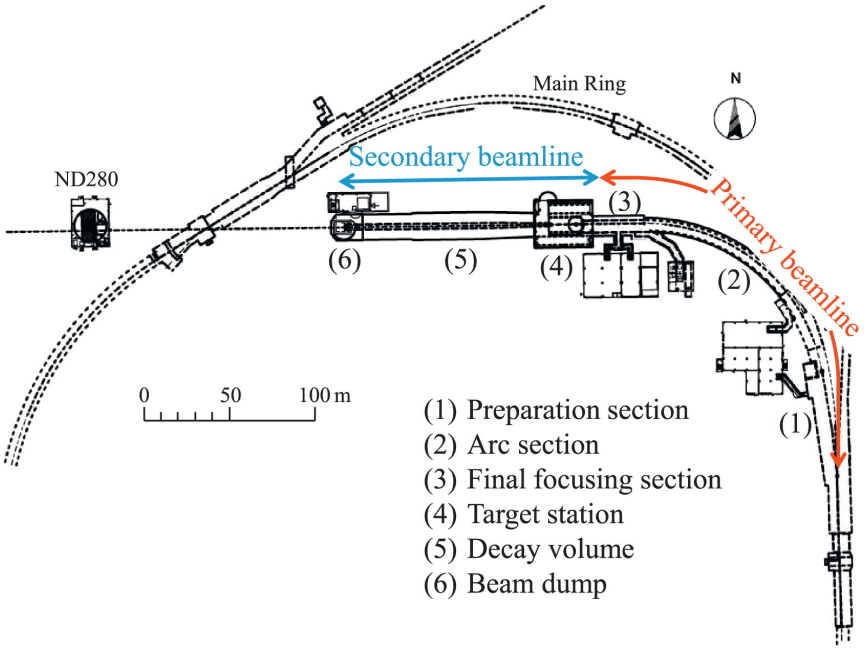

Figure 4.3: Overview of the T2K neutrino beamline, showing the secondary and primary beamline [42].

proton beam target and three magnetic horns, all located inside a helium vessel. A beam window separates the target station from the primary beamline at the upstream end and is connected to the decay volume at the downstream end. The target is made from a graphite rod of length 91.4 cm and diameter 2.6 cm and is sealed inside a 0.3 mm thick titanium case. Each of the three magnetic horns [83] were designed for a pulsed peak current of 320 kA and consist of two, inner and outer, coaxial conductors encompassed in a volume containing a torodial magnetic field of up to 1.7 T. The first horn collects the mesons produced by proton interactions at the target whereas the second and third horns focus the mesons. The horns can be run in either Forward Horn Current (FHC) mode or, if the polarity of the magnetic field is reversed, Reverse Horn Current (RHC) mode. When running in FHC mode, positively charged mesons are collected to produce a neutrino beam whereas in RHC mode negatively charged mesons are collected to produce an antineutrino beam:

$$\begin{aligned} I_{horn} &= +250KA \Longleftrightarrow K^+/\pi^+ \quad \rightarrow \mu^+ + \nu_\mu \\ I_{horn} &= -250KA \Longleftrightarrow K^-/\pi^- \quad \rightarrow \mu^- + \bar{\nu}_\mu. \end{aligned} \tag{4.1}$$

The decay volume is a long steel tunnel approximately 96 m long surrounded by 6 m thick reinforced concrete shielding. The charged meson beam enters this decay volume where they decay to form muon neutrinos (FHC)

$$\pi^+ \rightarrow \mu^+ + \nu_\mu \tag{4.2}$$

or muon antinuetrinos (RHC)

$$\pi^- \rightarrow \mu^- + \bar{\nu}_\mu. \tag{4.3}$$

A small number of muon neutrinos and antineutrinos are also produced from the decay of kaons, these ν_μ have a higher energy than the ones produced from pion decay:

$$\begin{aligned} K^+ &\rightarrow \mu^+ + \nu_\mu & K^+ &\rightarrow \pi^0 + \mu^+ + \nu_\mu & (FHC) \\ K^- &\rightarrow \mu^- + \bar{\nu}_\mu & K^- &\rightarrow \pi^0 + \mu^- + \bar{\nu}_\mu & (RHC) \end{aligned}$$

The resulting beam is dominated by muon neutrinos and antineutrinos but there is a small ν_e contamination produced via the K_{e3} decay which has a branching ratio of 5%

$$K^- \rightarrow \pi^0 + e^+ + \nu_e.$$

Some fraction of ν_e contamination also occurs in the decay tunnel from muon decay

$$\mu^+ \rightarrow e^+ + \nu_e + \bar{\nu}_\mu.$$

At the end of the decay volume is the beam dump; this consists of a core made of 75 tons of graphite, 3.174 m long, 1.94 m wide and 4.69 m high, contained within a helium vessel. Muons below $\sim$ 5 GeV/C and all hadrons are stopped by the beam dump whereas the neutrinos pass through the beam dump to be used for physics experiments. The muons above $\sim$ 5 GeV/C are monitored to characterise the neutrino beam. The neutrino beam intensity and direction is monitored by the muon monitor, which is located just behind the beam dump. The neutrino beam direction can be measured with a precision better than 0.25 mrad, which corresponds to a 3cm precision of the muon profile centre.

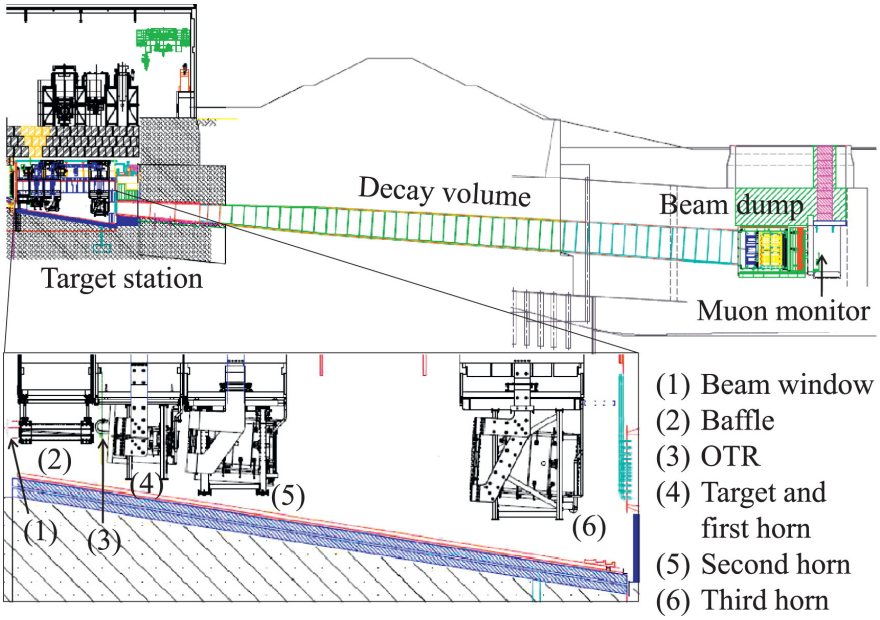

Figure 4.4: Side view of the secondary beamline, showing the target station, decay volume and beam dump [42].

4.3 Off-Axis Neutrino Beam

The T2K experiment uses an off-axis beam with an angle 2.5° away from the beam centre. This method allows a narrow-band neutrino beam to be selected so that the neutrinos observed have a narrow spread of energy. The peak energy of the neutrino beam can be varied by changing the off-axis angle. As the peak energy of the neutrino beam at the first oscillation maximum at SK is $\sim$ 0.6 GeV, the off-axis angle has been

set to 2.5°. This maximises the effect of the neutrino oscillations at 295 km and reduces background events, Figure 4.5 shows the neutrino flux predicitions for different off-axis angles.

The outgoing neutrino energy (E_ν) can be written as:

$$E_\nu = \frac{m_\pi^2 - m_\mu^2}{2(E_\pi - p_\pi.cos\theta)} \tag{4.4}$$

where m_π, E_π and p_π are the mass, energy and 3-momentum of the pion respectively, m_μ is the mass of the muon and θ is the angle between the neutrino and pion directions.

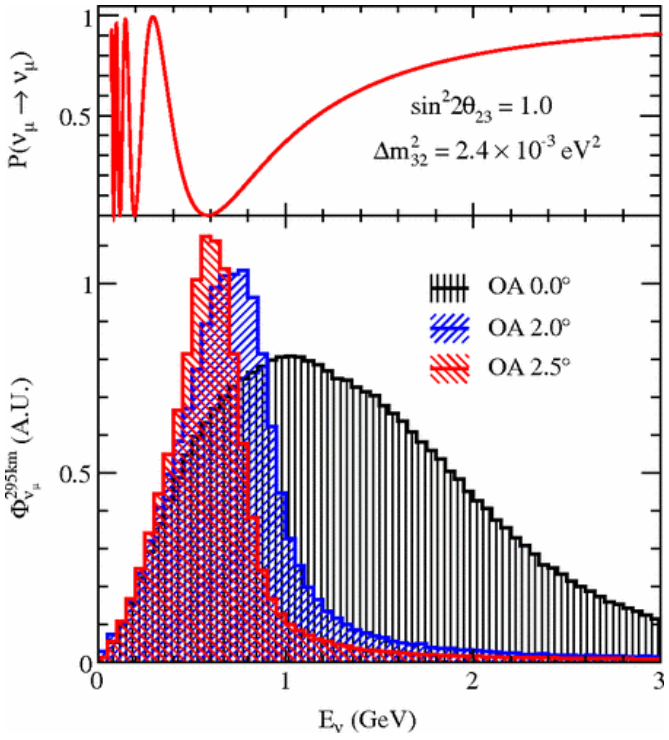

Figure 4.5: T2K neutrino flux predictions for different off-axis angles and muon neutrino survival probability at 295 km as a function of neutrino energy [84].

4.4 Neutrino Flux

The neutrino flux is modelled by a Monte Carlo (MC) simulation driven by experimental data from the experiment NA61/SHINE [85], as it covers the full kinematic region of interest for T2K. FLUKA [86] is used to simulate the hadronic interactions inside the graphite target and passes kinematic information to JNUBEAM, a MC simulation package based on GEANT3 [87] developed to cover the entire secondary beamline,

and interactions outside the target use GEANT3/GCALOR [88]. Neutrino interactions are simulated with a neutrino event generator, either NEUT [55] or GENIE [56].

The runs 1-8 prediction of the T2K flux for the near and far detector in both ν and $\bar{\nu}$ mode is shown by Figure 4.6.

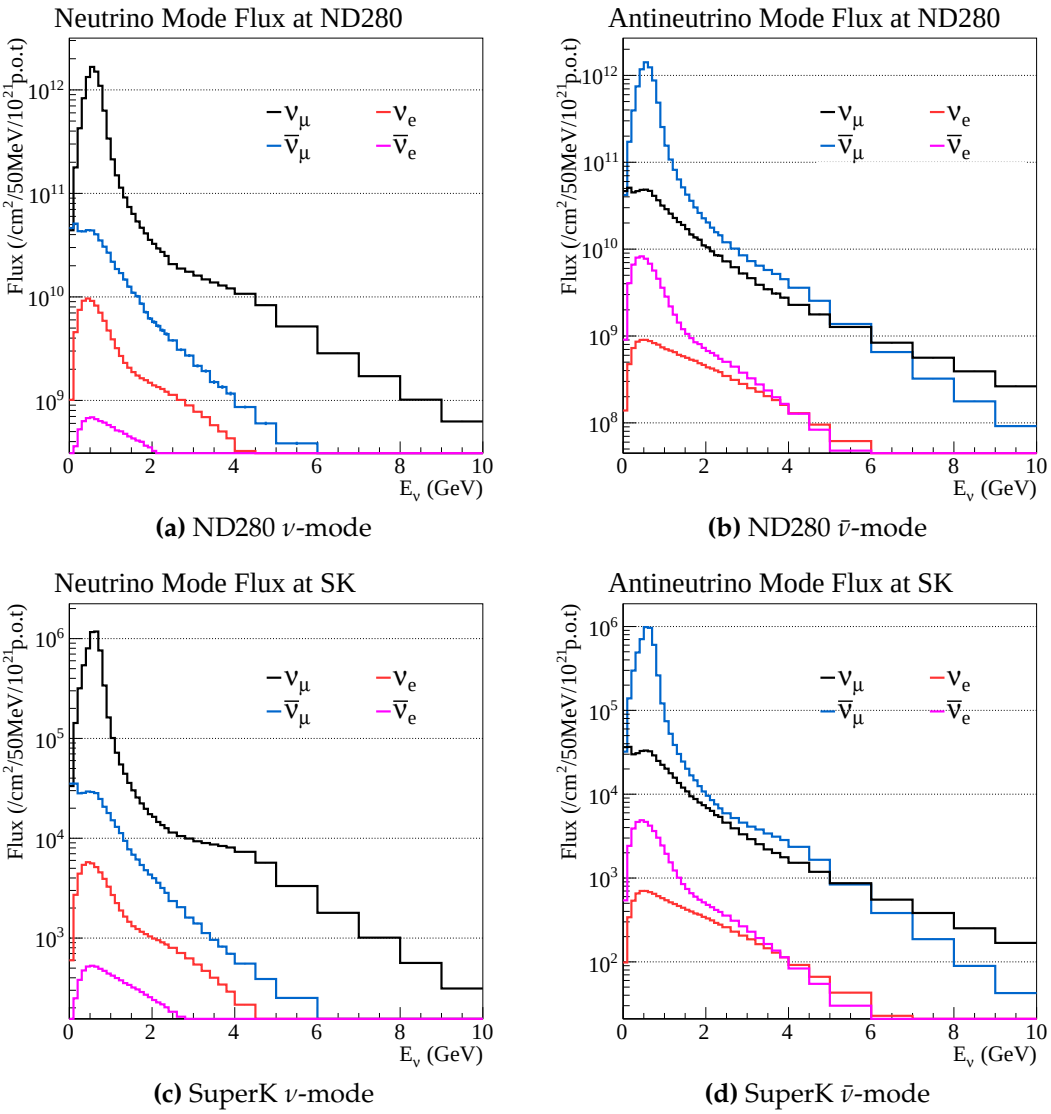

(a) ND280 ν-mode **(b)** ND280 $\bar{\nu}$-mode

(c) SuperK ν-mode **(d)** SuperK $\bar{\nu}$-mode

Figure 4.6: Flux Predictions for ND280 (left) and SuperK (right) for runs 1-8 with horns operating in 250 kA mode, normalised to 10^{21} POT [82].

4.5 T2K Data

T2K began data collection in January 2010 in neutrino mode and since 2014 the beam has been running mainly in antineutrino mode. The data collected so far has been divided into nine runs and is summarised in Table 4.1, and the number of protons on target (POT) accumulated along with beam power is shown in Figure 4.7. The analysis presented in this thesis in Chapters 6-8 uses the data from runs 2-4 which were collected between November 2010 and April 2013 and correspond to 5.736 x 10^{20} POT in neutrino mode.

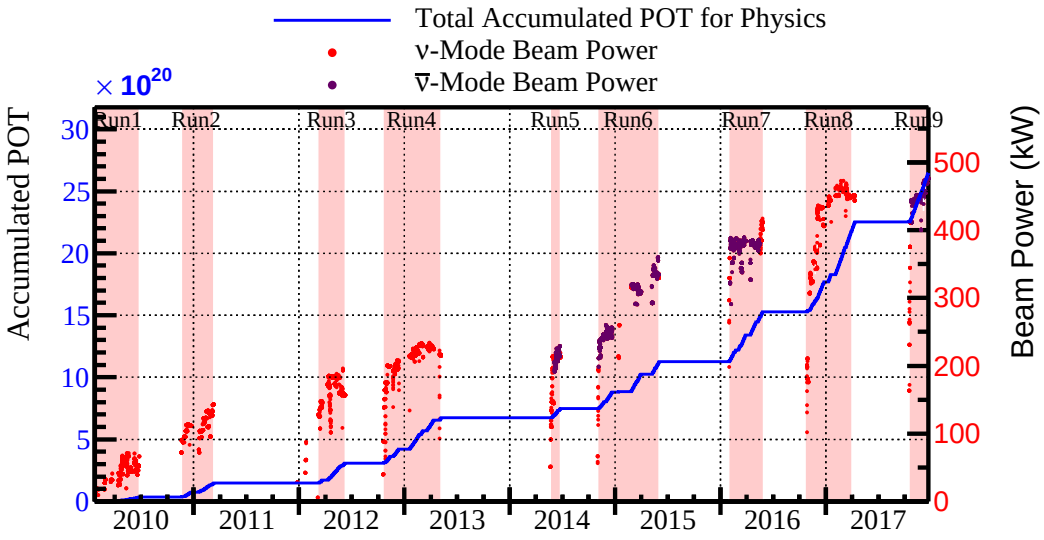

Figure 4.7: Number of accumulated protons on target (POT) for each T2K run, as well as the J-PARC proton beam power [82].

Run Period	Dates	ν POT (x 10^{20})	$\bar{\nu}$ POT (x 10^{20})
Run 1	Jan. 2010 - Jun. 2010	0.323	-
Run 2	Nov. 2010 - Mar. 2011	1.108	-
Run 3	Mar. 2012 - Jun. 2012	1.579	-
Run 4	Oct. 2012 - May 2013	3.560	-
Run 5	May 2014 - Jun. 2014	0.242	0.506
Run 6	Nov. 2014 - Jun. 2015	0.190	3.505
Run 7	Feb. 2016 - May 2016	0.480	3.520
Run 8	Oct. 2016 - Apr. 2017	7.252	-
Run 9	Oct. 2017 - May 2018	0.205	8.887
Total	Jan. 2010 - May 2018	15.131	16.505

Table 4.1: A table outlining the details of the T2K runs, including the number of POT for neutrino and antineutrino mode.

4.6 Super-Kamiokande

Super-Kamiokande (SK) [89] is a 50 kiloton (22.5 kiloton fiducial) water Cherenkov detector located in Kamioka Township, Gifu Prefecture, Japan. SK is used as the far detector for the T2K experiment, as well as having other scientific goals including proton decay searches and studies of neutrinos from sources such as the sun, atmosphere, supernovae and gamma rays among many others. SK published the first unambiguous evidence of neutrino oscillation in atmospheric neutrinos [90] and confirmation of the solar neutrino flux deficit. SK is located in the Mozumi mine and the detector cavity lies under Mt. Ikenoyama, as shown by Figure 4.8.

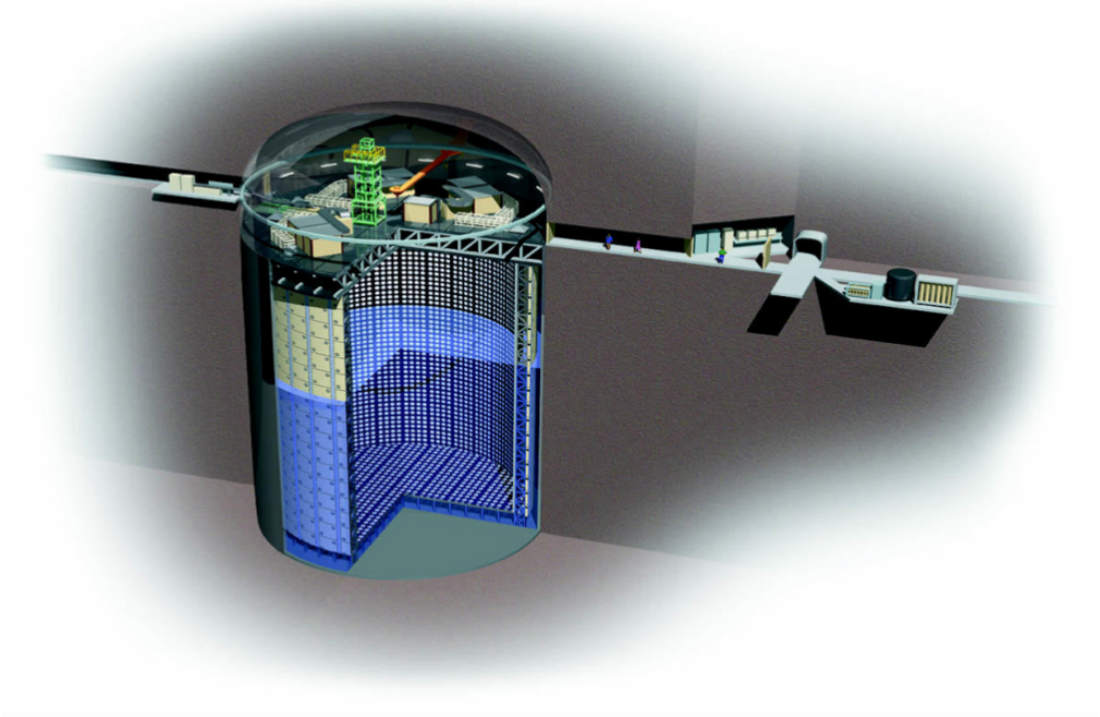

Figure 4.8: A diagram of the Super-Kamiokande detector [82].

The SK detector consists of a 39 m diameter and 42 m tall welded stainless-steel tank. Inside the tank there is a stainless-steel framework of thickness 55 cm, spaced approximately 2-2.5 m inside the tank walls, which supports two separate arrays of PMTs. There are 11,146 inward-facing PMTs located about 2.5 m inside the wall and, along with the the volume of water they view, are referred to as the Inner Detector (ID). The outward-facing PMTs, of which there are 1885, are located 2 m inside the wall. These PMTs, and the water volume they view, are known as the Outer Detector (OD). Events over a wide range of energy (4.5 MeV to over 1 TeV) can be detected; for low energy events (solar neutrino studies) the energy is calculated from the number of PMT hits, while for high energy events (atmospheric neutrino and muon studies) the energy is

measured in terms of net charge detected by PMTs. The Cherenkov light emitted by the charged particles produced is used to detect neutrino interactions. The size, shape and orientation of the Cherenkov light pattern produced on the ID walls can be used to identify events as being electron-like if they are fuzzy, as electrons undergo multiple Coulomb scattering resulting in a blurred ring, or muon-like if they are not, as muons are highly penetrating so will pass through the detector with minimal scattering producing a sharper and better defined ring; this is shown by Figure 4.9.

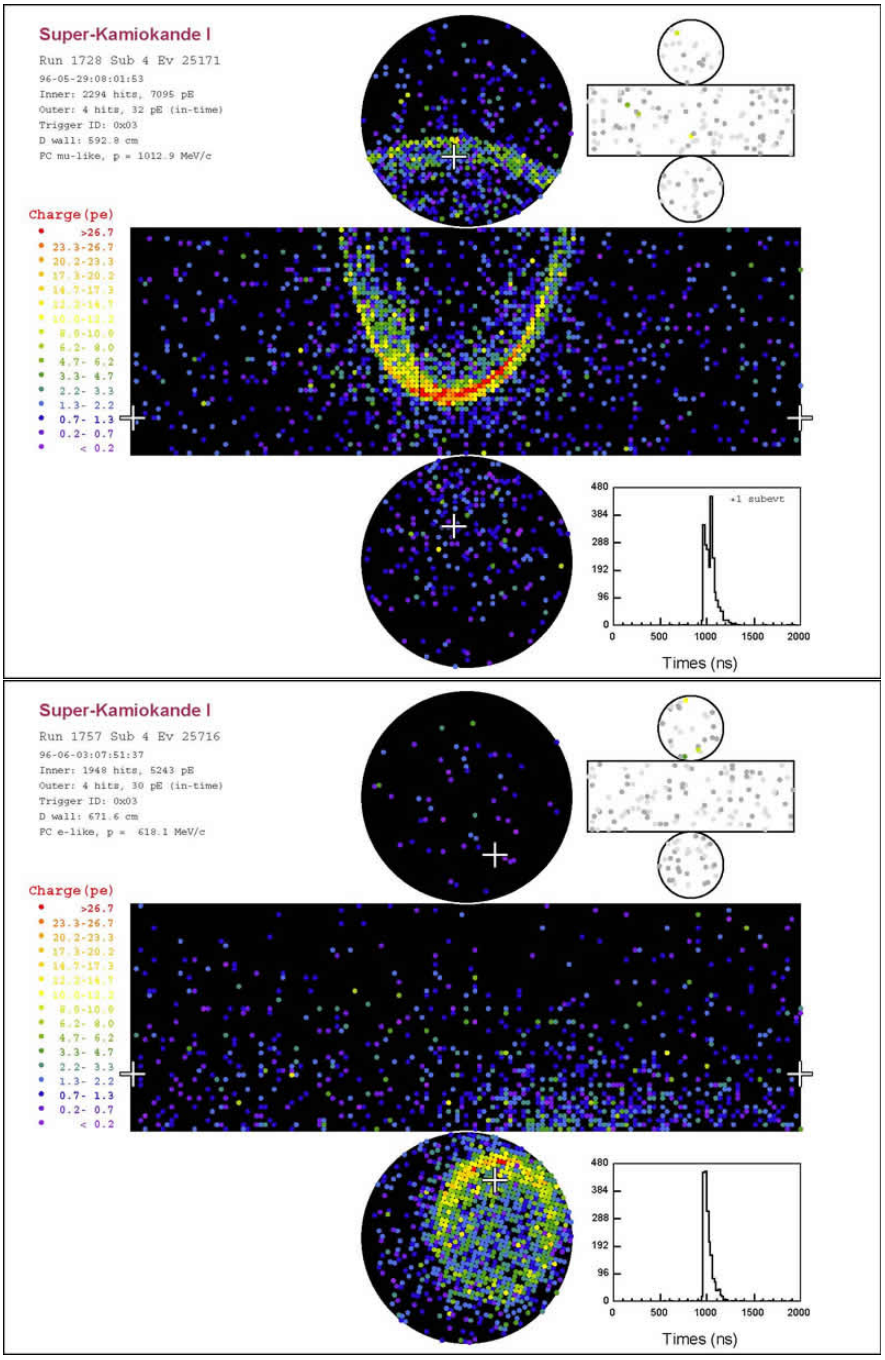

Figure 4.9: SuperK Event Display. The top image is a muon-like event and the bottom image is an electron-like event [91].

4.7 T2K Near Detectors

The near detector complex at J-PARC is located 280 m downstream from the production target and is used to monitor the neutrino beam, measure neutrino event rates and help minimise uncertainties in measurements of neutrino oscillation parameters. The T2K near detectors consist of an on-axis detector, Interactive Neutrino Grid (INGRID), and an off-axis detector, Near Detector at 280m (ND280), described in more detail in Sections 4.7.1 and 4.7.2 respectively.

4.7.1 INGRID

The on-axis detector located at J-PARC is known as INGRID. It contains a set of modules with sufficient target mass to continuously monitor the neutrino beam rate, profile and centre. In order to achieve this, INGRID is designed to sample the beam in a transverse section of 10 m x 10 m, with 14 identical modules arranged in two groups along the horizontal and vertical axes, as shown by Figure 4.10. The point at which the two modules cross in the centre is the neutrino beam centre and is 0° with respect to the direction of the primary proton beamline. The purpose of the two off-axis modules is to verify the axial symmetry of the neutrino beam.

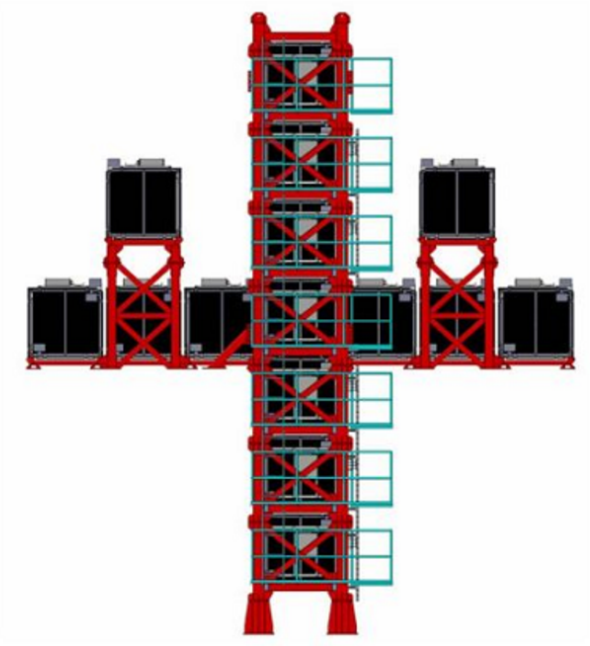

Figure 4.10: Overview of INGRID viewed from beam upstream [42].

The INGRID modules are arranged in a sandwich structure of nine iron target plates and eleven tracking scintillator planes as shown by Figure 4.11. Charged particles coming from the outside of the modules are rejected by veto scintillator planes that

surround the tracking scintillator planes. A more detailed description of the INGRID module can be found at [42].

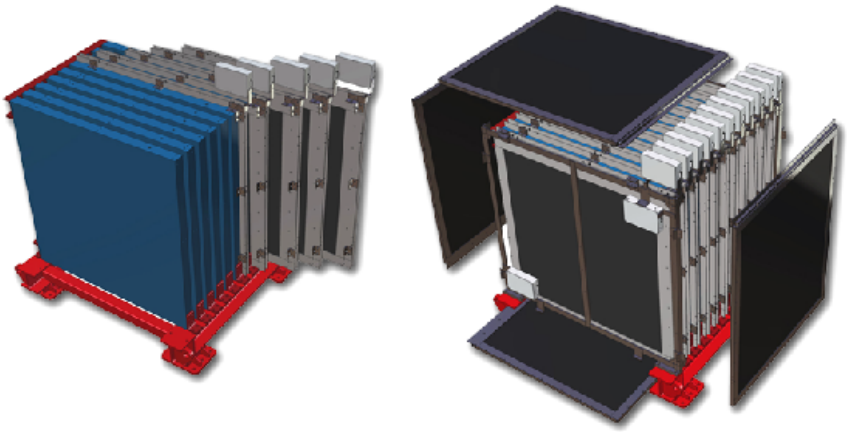

Figure 4.11: A single INGRID module, which consists of a sandwich structure of nine iron plates and 11 tracking scintillator planes surrounded by a veto scintillator plane [42].

Proton Module

A module separate from the 16 INGRID modules, known as the Proton Module, was installed in 2010, and is shown by Figure 4.12. The purpose of the Proton Module is to measure the neutrino cross section precisely with the T2K on-axis neutrino beam. The measurement of CCQE cross sections on carbon at mean neutrino energies of 1.94 GeV and 0.93 GeV was achieved with a total uncertainty of around 20%, dominated by neutrino flux errors.

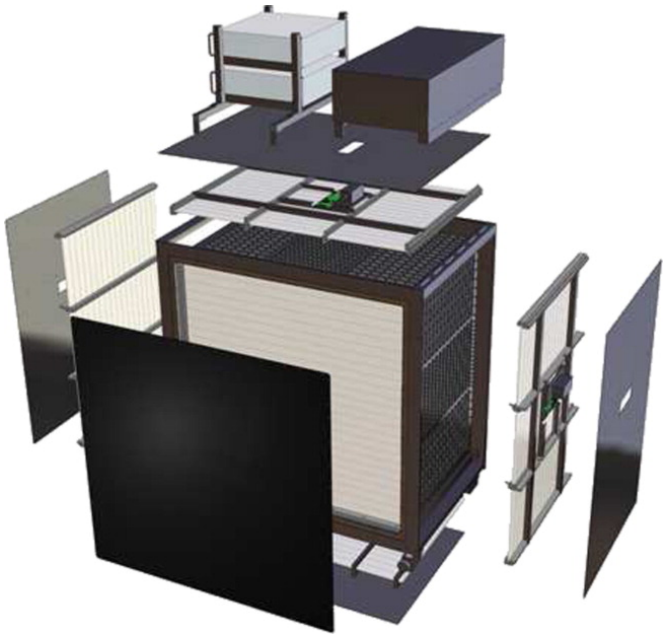

Figure 4.12: Schematic view of the proton module [42].

The Proton Module consists of 34 tracking planes, made up of 32 scintillator bars which are finer grained than the INGRID module planes, surrounded by 6 veto planes; there are no iron plates present. The module is 1.42 m high x 1.43 m wide x 0.96 m deep, has a total target mass of 556 kg and contains 1204 channels.

The Proton Module is currently located upstream of INGRID. The Proton Module is a fully-active detector therefore track reconstruction from the interaction point is possible. An example of an Ingrid and Proton Module Event Display is shown by Fig 4.13.

4.7.2 ND280

A large, fine grained, magnetised off-axis near detector, ND280 is located at J-PARC 280 m downstream from the start of the neutrino beam. It is designed to measure the flavour content, energy spectrum and NC and CC interaction rates of the unoscillated neutrino beam to predict the neutrino event rate and energy spectrum at the SK detector.

The goals of ND280 are to:

- measure the ν_μ energy spectrum
- determine the rate of ν_μ induced CC interactions
- measure the inclusive and exclusive cross section rates
- measure the NC π_0 production rates.

ND280 is located inside the UA1 magnet at a magnetic field of 0.2 T and contains several subdetectors designed to measure neutrino interactions in the 100 MeV to few GeV range. The tracker section of ND280 (used in most analyses) consists of 2 Fine Grained Detectors (FGDs) used as a target for neutrino interactions sandwiched between 3 gaseous Time Projection Chambers (TPCs), that have excellent particle identification capabilities. A π^0 detector, (PØD), is located upstream of the tracker to form what is known as the basket region and is optimised for π^0 detection. Surrounding this basket region are the Electromagnetic Calorimeters (ECALs) and a magnet which houses a Side Muon Range Detector (SMRD) that measures muon momenta. This section will describe, in further detail, the subdetectors that make up ND280, as shown by Figure 4.14.

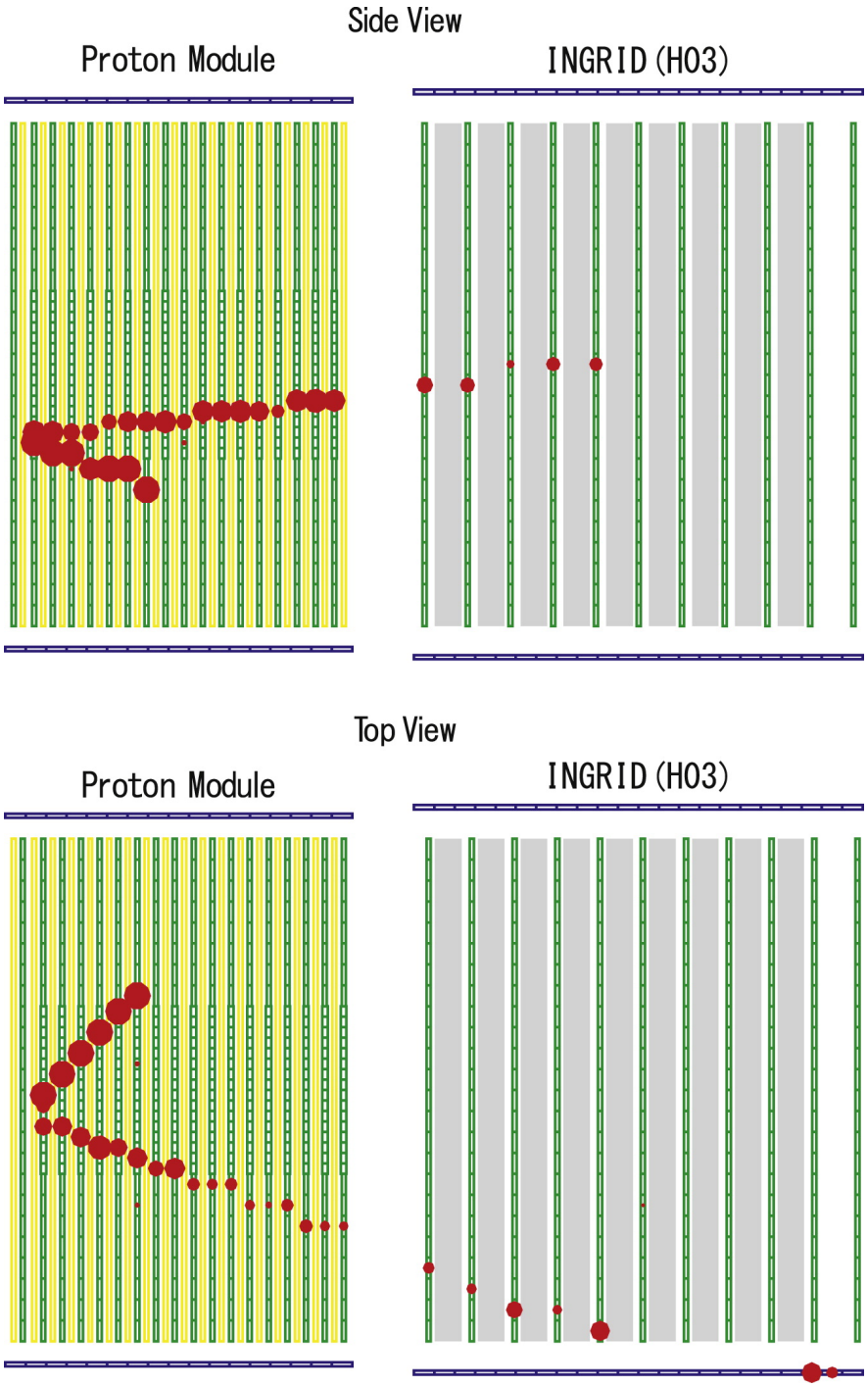

Figure 4.13: An event display showing a typical proton module event (left) and INGRID event (right) [42].

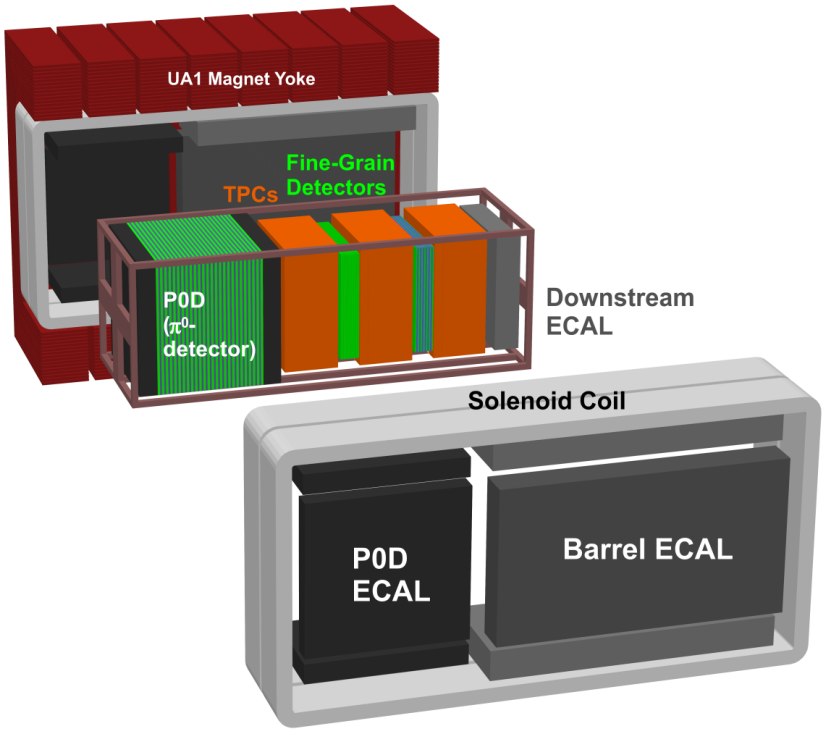

Figure 4.14: A diagram of the ND280 off axis detector [42].

4.7.3 ND280 Magnet

The magnet that houses the ND280 detector was previously used for the UA1 detector [92] and NOMAD experiment [93], both based at CERN. The magnet provides a dipole magnetic field of 0.2 T and is comprised of water-cooled aluminium coils that produce the horizontally oriented dipole field, and a 850 ton flux return yoke. The magnet has an inner volume of 7.0 m x 3.5 m x 3.6 m and an outer volume of 7.6m x 5.6 m x 6.1 m. The aluminium coils are shaped like bars with a 5.45 cm x 5.45 cm square cross section and a central 23 mm diameter bore for water to flow.

4.7.4 Side Muon Range Detector

The Side Muon Range Detector (SMRD) is incorporated into the magnetic yoke that surrounds ND280 and consists of layers of plastic scintillator placed in the air gaps found in the yokes of the UA1 magnet [94].

The main purpose of the SMRD is to measure the momentum of muons produced in neutrino interactions and muons that escape the inner detectors at a large angle with respect to the neutrino beam. The SMRD also acts as a cosmic ray trigger and helps identify beam-related event interactions that occur in the cavity walls and iron of the magnet. The SMRD consists of a total of 440 scintillator modules (192 horizontally

oriented and 248 vertically oriented) which are located in the 1.7 cm air gaps between 4.8 cm thick steel plates that make up the UA1 magnet flux return yokes; Figure 4.15 shows a single yoke structure. The SMRD consists of three scintillator module layers on the top and bottom of all yokes, all of which are located in the innermost gaps of the UA1 magnet in order to detect particles escaping the inner detectors.

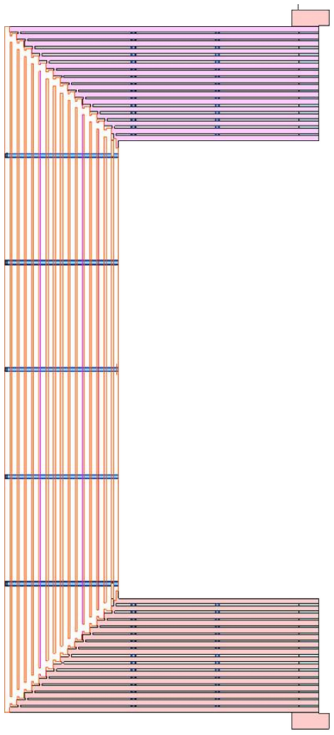

Figure 4.15: A drawing of the single yoke structure showing bolts holding the iron plates together to form horizontal, vertical and corner subsections [94].

4.7.5 Fine Grained Detectors

The Fine Grained Detectors (FGDs) provide the target mass for neutrino interactions and tracking of charged particles originating from the interaction vertex [95].

There are 2 types of FGDS in ND280: FGD1 which contains scintillator bars only (shown by Figure 4.16) and FGD2 which contains additional water layers. The scintillator bars are 1 cm long and have a square cross section of 9.6 mm on a side, which provides the fine granularity of the FGD. Each scintillator bar contains a reflective coating which includes $Ti0_2$ and a wavelength shifting fibre that connects to an MPPC. The scintillator bars are arranged in XY modules with each module containing a layer of 192 scintillator bars in the horizontal direction glued to 192 bars in the vertical direction. The dimensions of the scintillator modules are 186.4 cm x 186.4 cm x 2.02 cm, not including electronics.

FGD1 has 15 of these modules whereas FGD2 has 7 scintillator modules, as well as 6 water target modules, composed of thin-walled hollow corrugated polycarbonate, 2.5 cm thick. The interaction rates in both the FGDs can be compared in order to measure separate cross sections on carbon and water. Each FGD has external dimensions of 230 cm x 240 cm x 36.5 cm (depth in beam direction), and contains 1.1 tonnes of target material, a cross section image of the FGD is given by Figure 4.17.

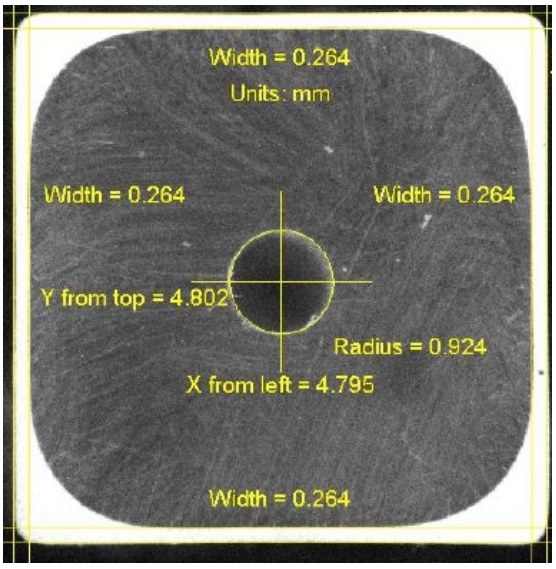

Figure 4.16: A CCD camera image of a FGD scintillator bar. The scintillator bar has a hole in the middle where the wavelength shifting fibre is coupled to a multi-pixel photon counter [95].

The FGD is capable of particle ID, by distinguishing protons, from muons and pions, using the dE/dx information, and Figure 4.18 shows a scatterplot of deposited energy vs track range for particles produced in neutrino interactions that stop in FGD1. Slower moving particles will deposit more energy per path length, therefore the energy loss in a particular region can be used to determine the particle that produced a track in the FGD.

The FGD is capable of measuring short-range particles such as low momentum recoil protons, using a measure of energy deposit in a particular vertex region known as the Vertex Activity (VA), which will be discussed further in the analysis Chapters, 6-8. The FGD requires a track to have at least 3 hits for reconstruction, and is able to reconstruct short tracks that begin and end in the FGD, not matched to TPC tracks using a pattern recognition algorithm. There is also a FGD-TPC matching process where TPC tracks are matched to the FGD hits using a Kalman filter [96].

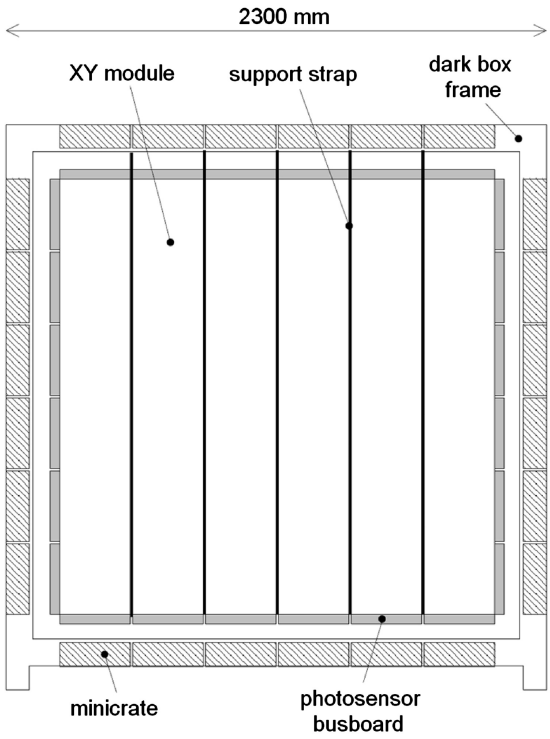

Figure 4.17: Cross sectional view of the FGD, as viewed by the beam. The location of the XY modules, photosensors, support straps, electronic minicrates and dark box are shown [95].

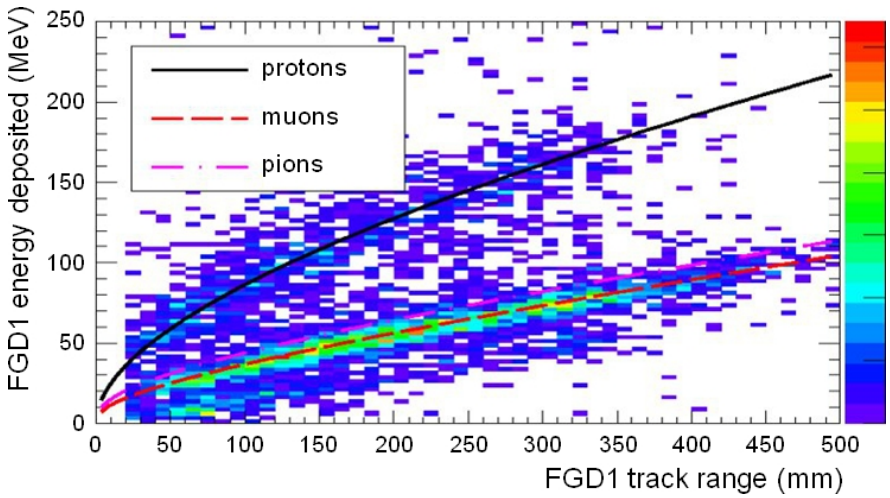

Figure 4.18: Distribution of FGD1 energy deposited (MeV) versus FGD1 track range (mm). The scatterplot represents stopping particles in neutrino beam data, and the curves show MC expectations for charged particles [95].

4.7.6 Time Projection Chamber

The ND280 tracker contains 3 Time Projection Chambers (TPCs) that separate the 2 FGDs that were described in the previous section. The main purposes of the tracker are to:

- provide three-dimensional imaging capabilities to determine the number and orientation of charged particles in the detector
- measure the momenta of charged particles produced by neutrino interactions outside of the TPC
- identify different types of charged particles and determine the relative abundance of electron neutrinos in the beam.

Data from the tracker allows studies of CC neutrino interaction rates and kinematics before oscillation in order to reduce uncertainties in the far detector oscillation measurements [97]. The TPC is capable of differentiating between different charged particles using the energy loss per distance, dE/dx, as shown by Figure 4.19. The dE/dx resolution for MIPs is 7.8 $\pm$ 2 %, which allows muons to be accurately distinguished from electrons.

Each TPC module is rectangular in design (to fit the geometry of the UA1 magnet) and consists of a double box design operated in a magnetic field of 0.2 T. The top, bottom, front and back walls of the inner box are made from 13.2 mm thick copper-clad-G10 laminated panels. The inner box is split into two parts separated by a cathode at its midpoint. The outer box is surrounded by 14.3 mm thick aluminium-rohacell laminated panels. The inner box walls serve as a field cage whereas the walls of the outer box are at ground potential, and CO_2 acts as an insulator between the two boxes; this is shown by Figure 4.20. The inner volume contains a gas mixture of Ar:CF_4:iC_4H_{10} (95:3:2) which allows drift space for the primary electrons. A readout plane is located on either end of the inner box volume (6 overall) and contain 12 micromegas modules tiled in two offset columns so that there is no alignment in the small inactive region of the module. When charged particles pass through the TPCs, ionisation electrons produced in the gas drift from the central cathode and towards one of the readout planes where they multiply and are detected by the bulk micromegas detectors.

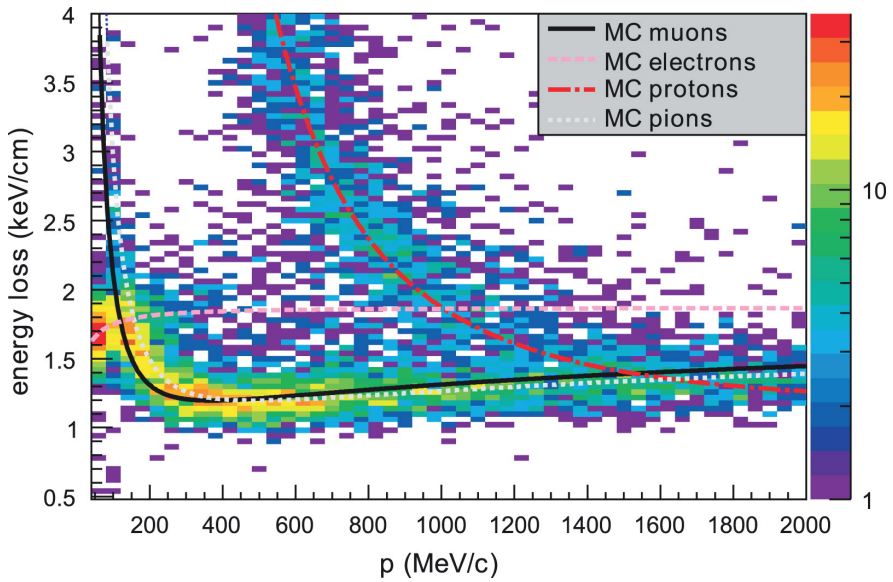

Figure 4.19: The dE/dx distribution in a TPC as a function of momentum for charged particles [97].

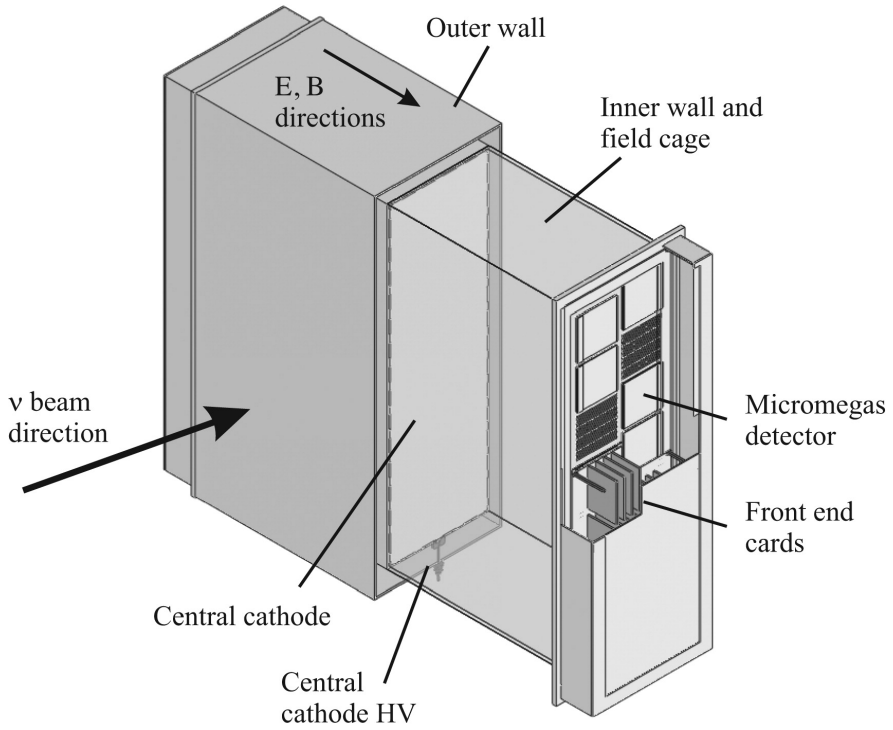

Figure 4.20: Cut-away drawing of the TPC, with the key features labelled [97].

4.7.7 Electromagnetic Calorimeters

The ECal is a lead-scintillator sampling electromagnetic calorimeter formed of three detectors: the barrel ECal and the Ds-ECal that surround the tracker region of ND280 (known as the tracker-ECal) and the PØD ECal [98] that surrounds the PØD, shown by Figure 4.14. The tracker-ECal consists of 6 barrel-ECal modules (2 top, 2 bottom, 2 side) parallel to the z (beam) axis and 1 Ds-ECal module; there are 6 PØD-ECal modules (2 top, 2 bottom, 2 side) parallel to the z axis. Each ECal module consists of layers of scintillating polystyrene bar with a thickness of 10 mm, bonded to lead sheets that act as a neutrino-interaction target, and Figure 4.21 shows an external view of a single ECal module.

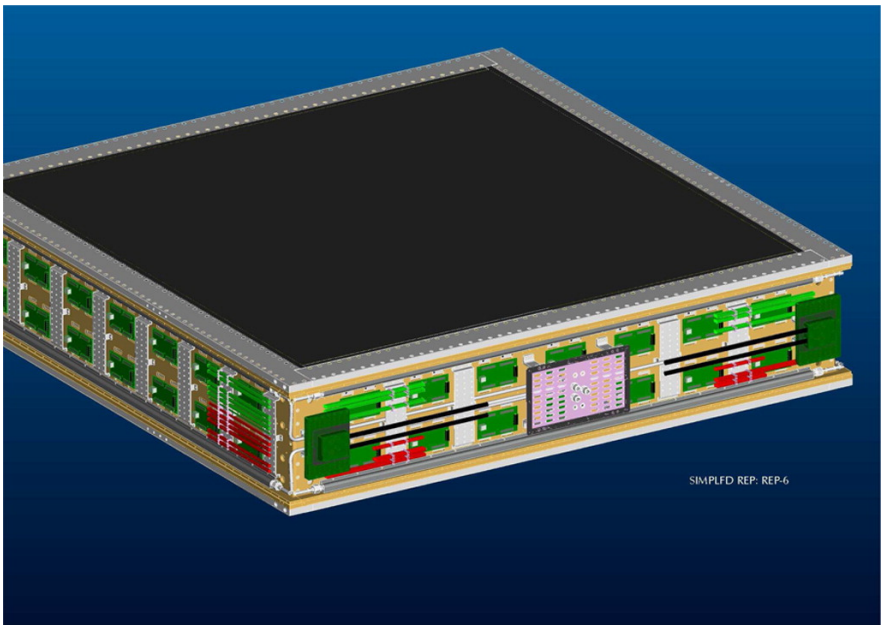

Figure 4.21: A close up external view of one ECal module, showing the scintillator bars running horizontally inside the module [42].

The ECal assists the rest of the ND280 detectors in full event reconstruction by detecting the energy and direction of charged particles, as well as photon detection. The physics aims of the tracker-ECal are to complement the TPC's charged-particle tracking and particle identification capabilities by detailed reconstruction of electromagnetic showers. The tracker-ECal is designed as a tracking calorimeter with 31 scintillator-lead layers in the barrel-ECal and 34 layers in the DS-ECal. The tracker-ECal is essential in ND280 calibration studies, and further details of this and of the tracker-ECal will be discussed in Section 5.5.

The purpose of the PØD-ECal differs from the tracker-ECal somewhat and this is reflected in the differences in design of the two types of ECal. The PØD-ECal is designed to tag escaping energy and distinguish between photons and muons. The PØD-ECal has only 6 scintillator-lead layers all running parallel to the beam direction, as its main

purpose is energy containment therefore it has coarser sampling than the tracker ECal which provides particle tracking. The lead sheets found in the PØD-ECal are thicker (4.00 mm compared to 1.75 mm in the tracker-ECal) to ensure that showers are well contained and photons are detected with a high efficiency. Table 4.2 lists the properties of the PØD ECal in more detail.

	PØD ECal (side)	PØD ECal (top/bottom)
Dimensions (m)	2.45 x 2.90 x 1.55	2.45 x 1.58 x 1.55
Weight (kg)	3000	1500
No. of layers	6	6
Bar Orientation	Longitudinal	Longitudinal
No. of Bars	828	912
Bars/layer	69	38
Bar length (m)	2.34	2.34

Table 4.2: Properties of the PØD ECal including dimensions, bar and layer details.

4.7.8 Pi-Zero detector

The Pi-Zero detector (PØD), located upstream of the ND280 tracker, is a plastic-scintillator based detector optimised for π^0 detection [99]. The dominant background to the ν_e appearance signal at SK occurs from events containing π^0s.

The PØD has been designed with a primary aim of measuring the neutral current π^0 rate

$$\nu_\mu + N \rightarrow \nu_\mu + N + \pi^0 + X \tag{4.5}$$

on a water target, in order to understand one of the largest backgrounds that occurs at SK.

The electronic supports and detector mounting system surround the active regions of the detector; a 3D drawing showing the main features of the PØD is shown by Figure 4.22. The PØD contains 40 scintillator modules known as PØDules, each comprised of two perpendicular arrays of triangular scintillator bars: 134 horizontal bars (2133 mm long) and 126 vertical bars (2272 mm long). The x and y planes of scintillator bars are read out by a single WLS fibre and are interleaved with fillable water target bags and lead and brass sheets. The PØD acts as a neutrino target and the water target cross sections are calculated by statistical subtraction of data, when the water target bags are full and, when they are empty. The PØDules are formed into four ”super-groups”

known as super-PØDules, as shown by a schematic in Figure 4.23.

There are two ECal super-PØDules, located at the front and rear sections, made from a sandwich of seven PØDules alternating with seven lead sheets. The water target is made from the remaining two super-PØDules located in the central region and is made from 13 PØDules alternating with water bag layers and brass sheets. The entire PØD active target region is 2103 mm wide x 2239 mm high x 2400 mm long, and the mass of the detector is 15800 kg with water and 12900 kg without water.

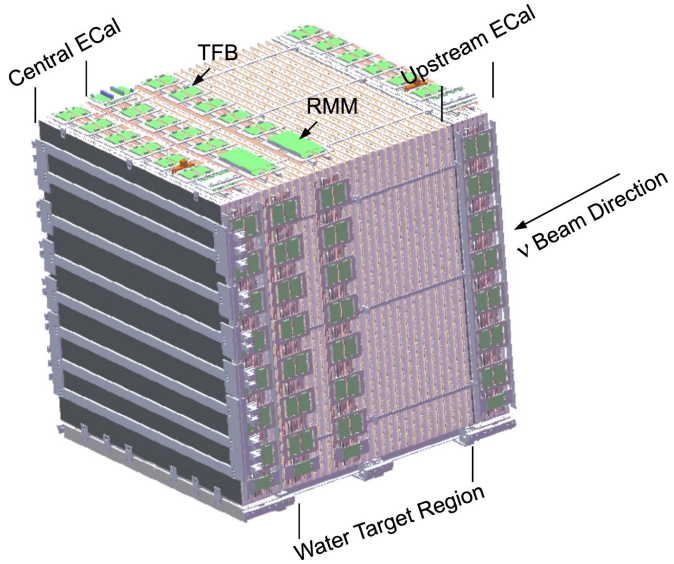

Figure 4.22: A three-dimensional view of the PØD [99].

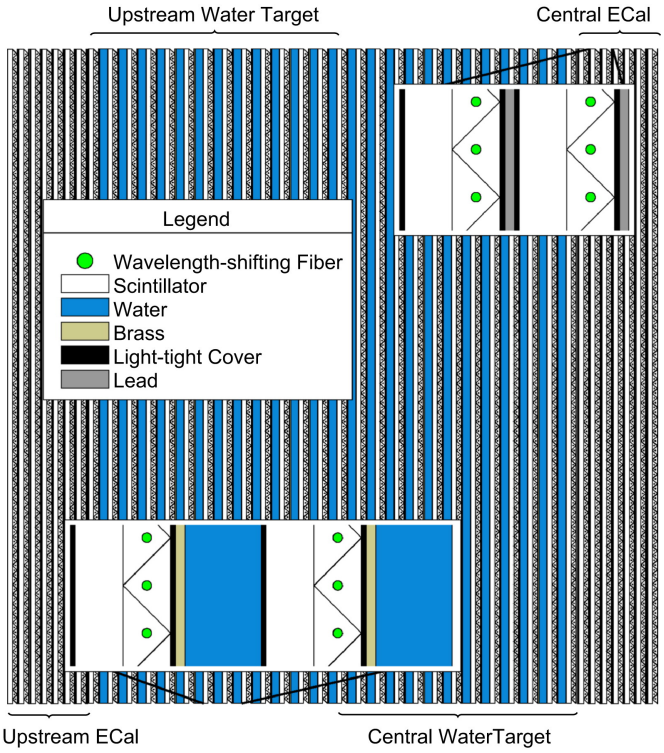

Figure 4.23: A schematic view of the PØD detector, showing the scintillator bars and water bags. The beam arrives from the left [99].

4.8 ND280 Software and Data Processing

The ND280 offline software suite comprises of a variety of packages, as shown by the flow chart in Figure 4.24. ROOT [100] and GEANT4 [101], written predominantly in C++, are used as the basic framework for data and simulations.

Maximum Integrated Data Acquisition System (MIDAS) [102] data files are converted for offline use by the *oaEvent* library before the data processing stages occur. There are three main stages to processing the data prior to analysis: calibration, reconstruction and reduction. The *oaEvent* data files enter the calibration stage controlled by the *oaCalib* package, which produces calibration constants for detectors stored in a mySQL database [103]. The reconstruction stage is handled by *oaRecon* and is a two-stage process: firstly, with individual subdetectors reconstructing tracks and showers for each event, then this information is combined for event reconstruction on a global level across muiltiple subdetectors. The final stage in data processing uses the *oaAnalysis* package to reduce the large reconstruction files into *oaAnalysis* files that are composed of ROOT objects.

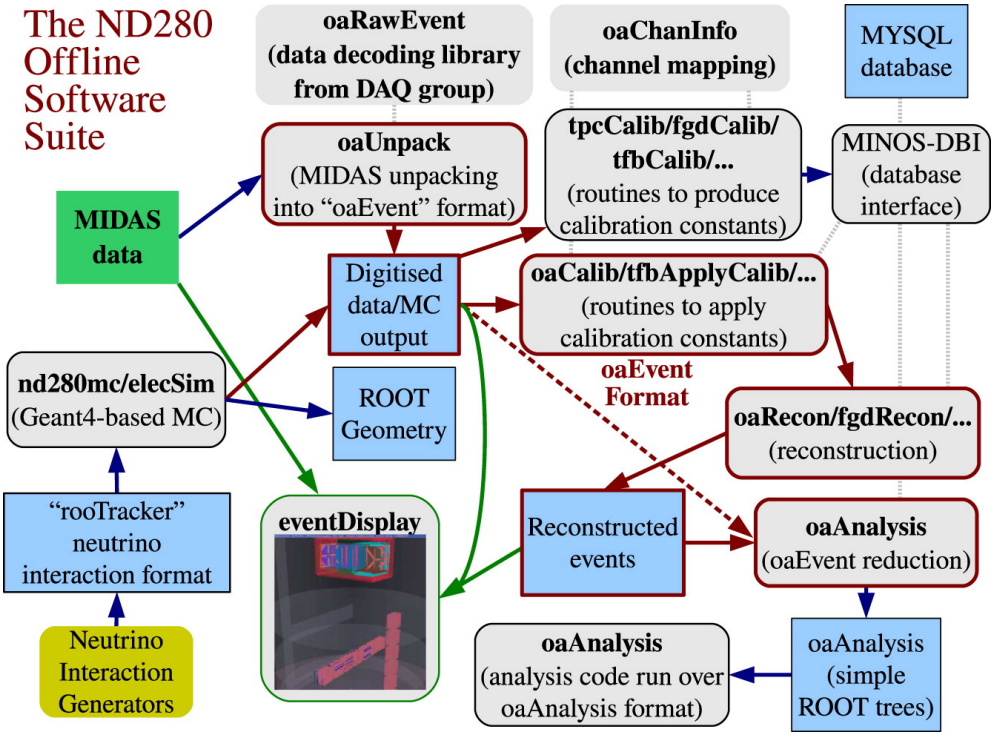

Figure 4.24: A flow chart of the ND280 Software Suite [42].

The MC data production requires firstly simulation of neutrino interactions which are handled by NEUT [55] or GENIE [56],[57]. At T2K, NEUT v5.3.2 is used as the default MC generator for Production 6 [1] and GENIE is used as a crosscheck; in this thesis GENIE v2.8.0 was used for the Vertex Activity (VA) analysis in Chapters 6 - 8. Geant4 is then used to simulate final state particle information which is propagated through *nd280mc* and stored as hits which contains a particle's position, time and energy deposited information. Finally the output is passed through *elecSim* in order to simulate the response of the detector. The generated MC files can then be processed in the same way as outlined previously for real data.

[1] For Production 7, NEUT v5.4.0 will be used.

Chapter 5

Electromagnetic Calorimeter and Calibration

This chapter will discuss ECal calibration including the ECal channel swap analysis and ECal bar-to-bar equalisation, as well as a more detailed description of the ND280 ECal itself. The ND280 ECal consists of a barrel ECal and a Downstream ECal (DsECal), which together are known as the tracker-ECal (which will be the main focus of this chapter), and a PØD ECal that has been described in more detail in Section 4.7.7. The barrel ECal is attached to the magnet and surrounds the inner tracking detectors whereas the DsECal is located further downstream in the basket region. Figure 5.1 shows the ND280 detector in the pit at J-PARC with the barrel ECal shown, for a reminder of the layout of ND280, the reader is referred to Figure 4.14.

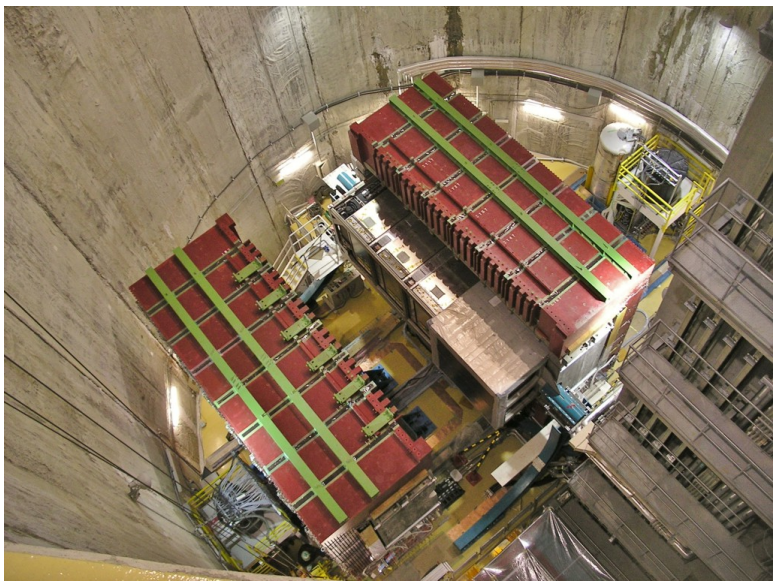

Figure 5.1: The ND280 detector located in the pit. The barrel ECal is shown in the centre of the image.

5.1 Barrel ECal

The barrel ECal consists of 6 modules: 2 top, 2 bottom and 2 side. Table 5.1 summarises the properties of the barrel ECal. Layers of scintillating polystyrene bars make up the modules, and each bar has a cross section of 40 mm x 10 mm. The purpose of the barrel ECal is to provide a neutrino-interaction target and this is achieved by the lead sheets attached to the modules which act as a radiator to produce electromagnetic showers.

	Barrel ECal (side)	Barrel ECal (top/bottom)
Dimensions (m)	4.14 x 2.50 x 4.62	4.14 x 1.67 x 4.62
Weight (kg)	8000	10000
No. of layers	31	31
No. of Bars (longitudinal)	1710	2280
No. of Bars (perpendicular)	3072	6144
Bars/layer (long.)	57	38
Bars/layer (perp.)	96	96
Bar length (m) (long.)	3.8	3.8
Bar length (m) (perp.)	2.28	1.52

Table 5.1: Properties of the Barrel ECal including dimensions, bar and layer details.

The four ECal top and bottom modules are 4140 mm long x 1676 mm wide x 462 mm high with 31 lead-scintillator layers: 16 with 1520 mm-long scintillator bars running perpendicular to the beam direction and 15 with 3840 mm-long bars parallel to the beam direction. Similarly, the two side barrel ECal modules are 4140 mm long x 2500 mm wide x 462 mm deep, with 31 lead-scintillator layers: 16 with 2280 mm long scintillator bars running perpendicular to the beam direction and 15 with 3840 mm long bars running parallel to the beam direction. In all cases, the perpendicular bars have a single-ended readout whereas the longitudinal bars all have double-ended readout. The ECal scintillator bars were made at the Fermi National Accelerator Laboratory (FNAL) from extruded polystyrene doped with organic fluors at concentrations of 1% PPO (Polyphenylene Oxide) and 0.03% POPOP. Polystyrene co-extruded with $Ti0_2$ coats the scintillator bars providing light reflection and isolation.

5.2 DsEcal

The DsECal was the first detector to be constructed in 2008 and commissioned at CERN in 2009 for cosmic ray and test beam data taking. It is 2300 mm high x 2300 mm wide x 500 mm long and comprises of 34 layers, each containing 50 scintillator bars of length 2000 mm; Table 5.2 lists the properties of the DsEcal. The most-upstream layer contains bars running in the x-direction, and the layers are surrounded by 25 mm thick aluminium bulkheads which contain holes for the WLS fibres to exit and connect to the MPPC.

	Downstream ECal
Dimensions (m)	2.3 x 2.3 x 0.5
Weight (kg)	6500
No. of layers	34
No. of Bars	1700
Bars/layer	50
Bar length (m)	2.0

Table 5.2: Properties of the Downstream ECal including dimensions, bar and layer details.

5.3 Electronics

The scintillator bars are read out by the MPPCs, which are a pixellated array of Avalanche Photo-Diodes (APDs). The readout system uses Trip-T front-end electronic boards (TFBs) which are mounted on cooling panels that contain slots to allow the TFBs to be connected to the MPPCs. There are 64 MPPCs which are connected to 48 TFBs. MPPCs are used rather than PMTs as they have a higher photon detection efficiency (PDE) than PMTs for the wavelength distribution produced by the WLS fibres. The TFBs are connected to the Readout Merger Modules (RMMS) which provide control and readout; the Barrel ECal has 8 RMMs and the DsECal has 2. The RMMs provide the communication interface with the off-detector data acquisition system (DAQ).

5.4 ECal Channel Swap

5.4.1 Introduction

A detailed study of the mapping of electronic channels to a specific scintillator bar location within the ND280 ECal was performed [104] which found 65 mis-mapped channels, that occur when an electronic channel is connected to an incorrect MPPC, to exist in the ECal. Mis-mapping of channels can lead to issues such as inaccuracies in particle reconstruction and measured energy deposition. ND280 relies heavily on event detection of the ECal as well as accurate software reconstruction, therefore it is important for these mis-mappings to be resolved for ND280 analyses. This section discusses the problem of mis-mapped channels in the ECal during detector construction, as well as implementation and validation of the ECal channel swaps.

5.4.2 Particle Detection

When a particle enters the ECal it will deposit its energy in a scintillator bar causing light to be produced. The scintillation light is directed to a WLS coupled to the MPPCs and pixels, which read out the light. The analogue sum of all the fired pixels is the output, known as a Pixel Energy Unit or PEU. The incoming MPPC signal is capacitively split, by a ratio of 1:10, into high and low gain channels. 1 PEU signal corresponds to roughly 10 ADC counts in the high gain channel whereas the low gain channel corresponds to around 500 PEU. The MPPCs correspond each to a channel and there are 22,336 channels in the T2K event reconstruction software. A detailed account of the electronics involved in the ECal was given in Section 5.3, but as a recap, there are up to 64 MPPC channels on each TFB. Each TFB has 4 Trip-T chips, numbered from 0-3 or A-D, which read in data for up to 16 channels. During the 2011 earthquake RMM9 lost two TFBs, TFB13 and TFB25, both containing 64 channels each. The Barrel ECal TFB mapping is shown in Figure 5.2. The Barrel ECal has single and double-ended bars whereas the DsEcal only has double-ended bars.

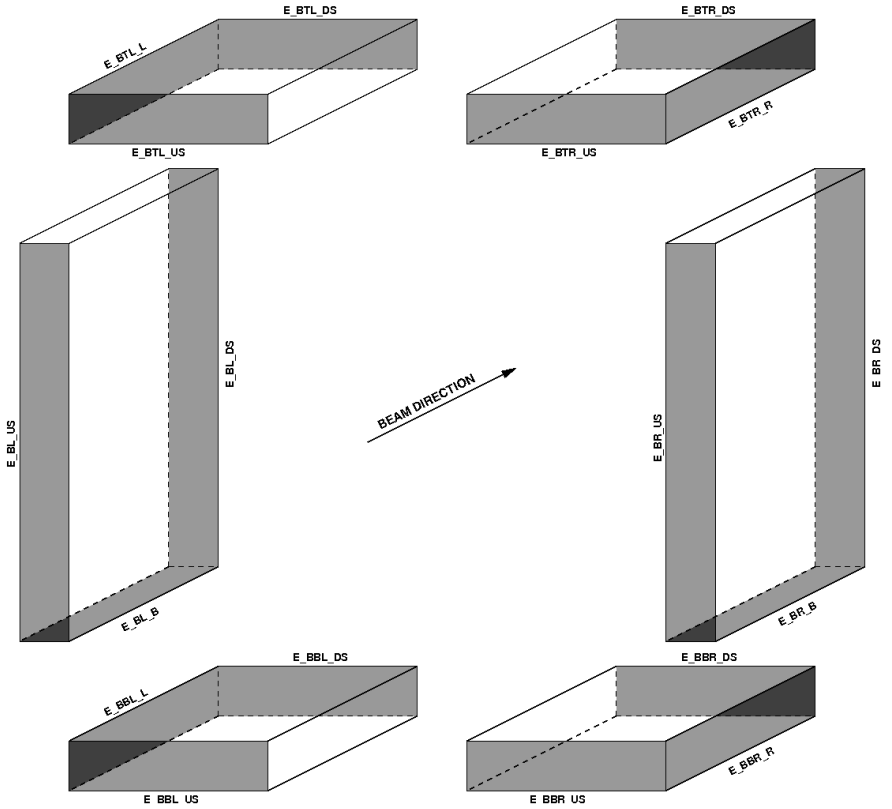

Figure 5.2: The TFB mapping of the Barrel ECal.

5.4.3 Identifying mis-mapped channels

The method for identifying the mis-mapped channels in the ECal was described in thorough detail in [104], and is beyond the scope of this thesis, but a brief overview of the procedure will be provided in this section to avoid ambiguity.

The analysis began with fitting a sample of production 6B cosmic ray data files from run 4 with Simple Track Fitter (STF), a simple and robust tool that quickly reconstructs data to produce 2D clusters which are connected by straight lines to form well understood tracks. STF can differentiate between hits forming a track and outlying hits, the latter of which were stored in a list and compared to tracks containing missing or anomalous hits to find mis-mapped channel candidates.

Plots were produced to show the number of hits for a given channel on each TFB in the ECal, excluding RMM2 and RMM7 as they belong to the PØDECal, and were analysed to see if there were any mis-mapped channels present which would be observed as a deficit of hits in two channels on the same TFB[1] as when a channel is hit in physical space, the potentially mis-mapped channel would be activated in the software.

[1]It is highly unlikely that a channel on one TFB would be swapped with a channel on a separate TFB as the readout cables used for the electronics in the ECal are not long enough for this to occur. For the instances where cross-TFB swaps did occur, they were rectified prior to the channel swap analysis.

STF proceeded to ignore these channels and this was noticeable in the plot as a vast decrease in the total number of hits for both the channels. Hits were then viewed in Bar/Layer space for RMMs rather than TFBs in order to reduce the number of plots produced. Some module types have two sets of RMM numbers that represent them (e.g. DsECal has RMM numbers 0 and 1 and barrel side left has RMM numbers 5 and 6), and Table 5.3 lists the RMM and TFBs numbers for all the ECal modules. In order to distinguish between single ended and double ended views, the hitEnd function is used where a value of -1, 0 and 1 corresponds to downstream, single and upstream respectively. As was mentioned before, the DsECal has only double ended bars therefore there is no single ended view plot for this module.

Module Name	RMM Number	Number of TFBs
Downstream ECal	0	28
Downstream ECal	1	28
P0D ECal Left (South)	2	15
Barrel Top Left (South)	3	44
Barrel Bottom Left (South)	4	44
Barrel Side Left (South)	5	26
Barrel Side Left (South)	6	26
P0D ECal Right (North)	7	15
Barrel Side Right (North)	8	26
Barrel Side Right (North)	9	24
Barrel Bottom Right (North)	10	44
Barrel Top Right (North)	11	44

Table 5.3: List of ECal Modules, RMM numbers and TFB numbers.

The variables that are stored in the anomalous channels list are RMM, Bar, Layer, Stream Direction, TripT and Channel and this is shown for a small sample by Table 5.4. The next stage was to search through each element in the array that corresponds to a hit bar and layer on each RMM and store the number of hits in a variable, a cut was used to ensure that the values were not from a dead channel. The mean of each value was taken as an ideal value for the channel in question and the square root of the mean was used similarly to the standard deviation. The hit value of the channel was compared to the mean of channels surrounding it and if the value differed greatly from the mean then it was regarded as an anomalous channel. This process was repeated with the known anomalous channels removed so that they did not affect the means and a list of anomalous channels was outputted. Further cuts including a more stringent timing cut were performed and finally the post-simple track fitted events were subtracted from the pre-simple track fitted event so that the residual hits that remained were likely to be mismapped channels.

5.4.4 Validation

As a first step in the validation the same cosmic data files used in the original analysis [104] were used in order to reproduce the Bar/Layer space plots. Figure 5.3 shows an example of one of the Bar/Layer space plots of the cosmic hits for RMM4 in the single ended view before the channel swap was applied. The pre-swapped Bar/Layer space plots were compared to the ones in the original analysis and as they were similar the validation process continued.

The 66 mis-mapped channels that were identified [104] were stored in data files in the ND280 software, and Table 5.4 shows examples of some of the channels for each ECal module type, the full list is provided in Appendix 9.1. The first step in implementing the channel swaps was to manually adjust the channels in the data files.

Once the channel swaps were implemented new reconstruction files that contained updated channel swap information were produced from raw MIDAS files. The processing takes raw MIDAS files and oaCalib is applied in order to produce a calibration ROOT file. Next, the calibration file is processed using oaRecon in order to produce the new reconstruction ROOT files which contain hit information with the channel swaps applied.

Once it was established that the processing stage worked, production 6B raw MIDAS files were run through the ND280 processing chain in order to produce reconstruction files and post-swap Bar/Layer space plots. Pre and Post channel swap Bar/Layer plots were produced for every ECal module type and included as examples are: Figure 5.4 which shows the post swap plot for the Barrel Bottom Left, i.e. RMM4 for the single ended view and Figures 5.5 and 5.6 which show the pre and post swap view for the DsECal. As it is difficult to identify where the channels of interest are in Figures 5.3- 5.6, the post-swap Bar/Layer space plots were subtracted from the pre-swap Bar/Layer space plots in order to produce subtracted plots. The subtraction was performed so that the resulting plots would include a deficit of hits corresponding to the swapped channels, when compared to the Bar/Layer locations of the mis-mapped channels. The z axis in the subtracted plots is the difference in channel hits, and each subtracted plot is provided in the Channel swap results in Section 5.4.5.

Table 5.4: List of ECal Modules, RMM, TFB TripChip, Channel ID, Geometry ID numbers and chan-64 numbers pre and post channel swap.

Module	RMM	TFB	TripChip	ChanID	GeomID	Bar no.	Layer no.	Chan64-pre swap	Chan64-post swap
Bot. Left	4	4	1	2283818026	170213453	77	20	26	27
Bot. Left	4	4	1	2283818027	170221645	77	22	27	26
Side Left	5	0	3	2284325996	170655767	23	0	60	61
Side Left	5	0	3	2284325997	170663959	23	2	61	60
Top Left	3	6	1	2283301920	171278336	0	24	16	24
Top Left	3	6	1	2283301928	171278338	2	24	24	16
Bot. Right	10	24	1	2287045667	169926688	32	14	19	21
Bot. Right	10	24	1	2287045669	169910305	33	10	21	19
Side Right	8	4	0	2285915137	170405936	48	3	1	4
Side Right	8	4	0	2285915140	170397745	49	1	4	1

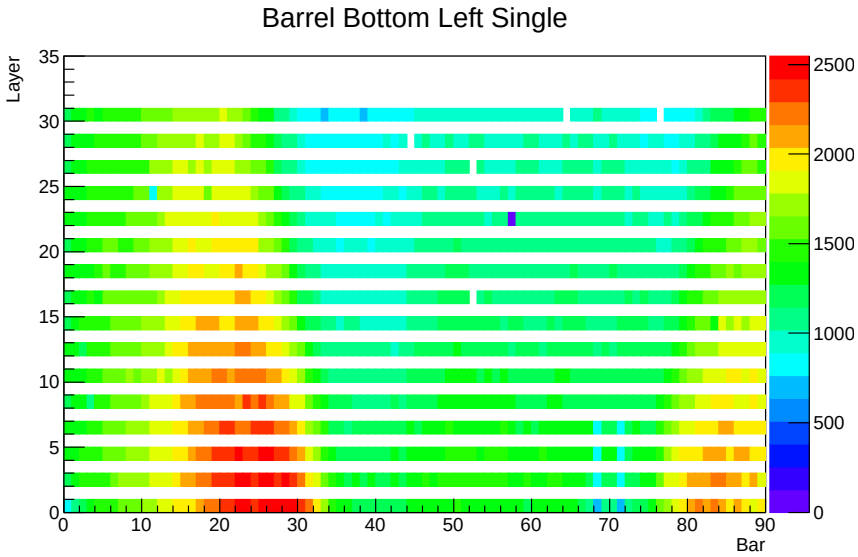

Figure 5.3: Plot showing the cosmic hits for the barrel bottom left ECal Module pre-channel swap. White hits indicate dead channels (as the channels are inactive there is no response hence observed by a ”blank” white hit) and the purple hits occur when the output is a bad channel response.

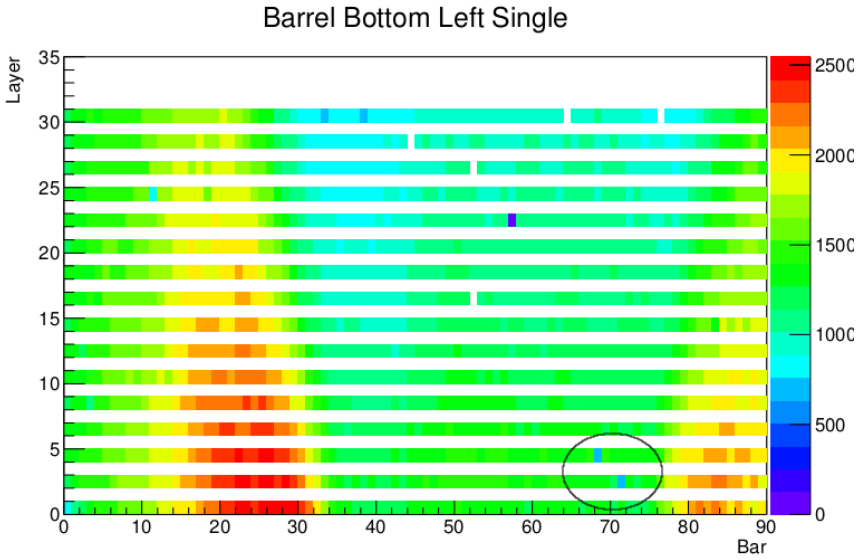

Figure 5.4: Plot showing the cosmic hits for the barrel bottom left once the mis-mapped channels were corrected, as shown by the absence of blue channels around bar number 70 and layer 5, indicated within the circled region.

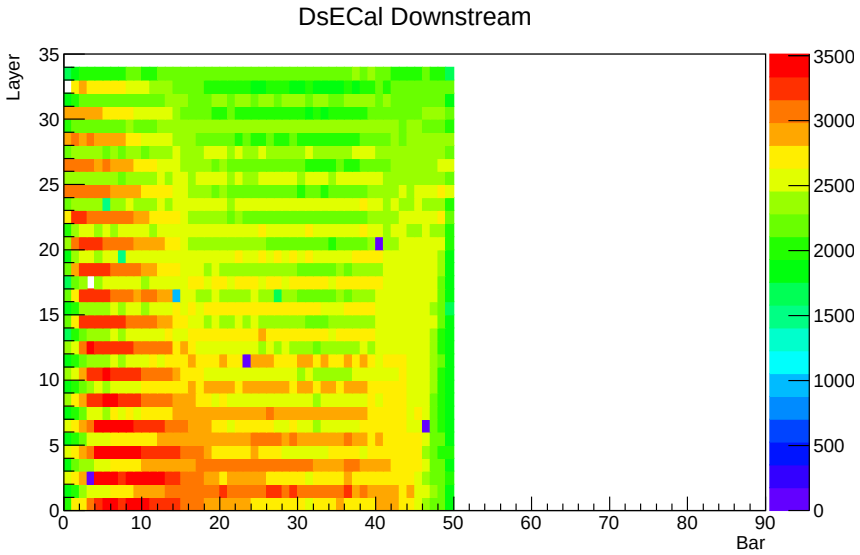

Figure 5.5: Cosmic hits for the DsECal downstream before the channel swap was applied.

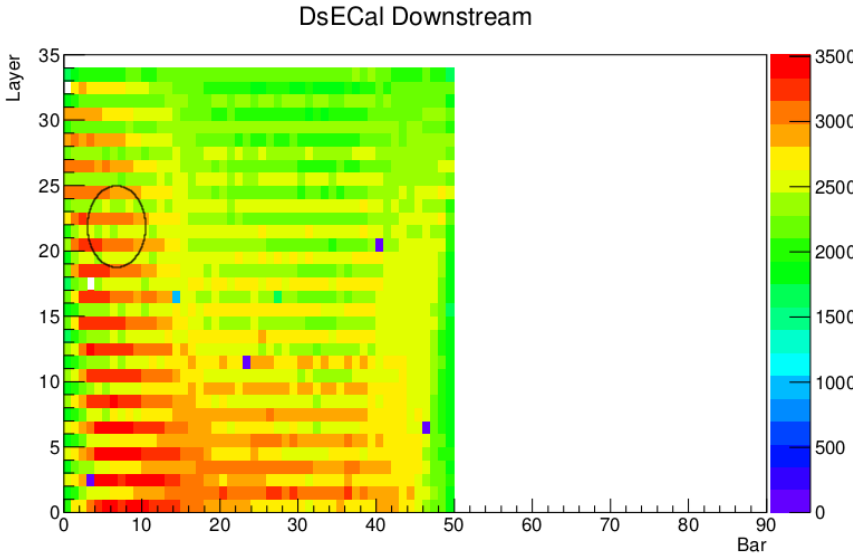

Figure 5.6: Cosmic hits for the DsECal downstream after the channel swap was applied, around layer 18 to 25 and bar number 6 to 8, as indicated by the highlighted region.

5.4.5 Results

The following section will discuss the results for each of the different modules for the Barrel ECal and DsECal module. A Bar/Layer space plot showing the cosmic hits after the post-channel swap plots were subtracted from the pre-channel swap is provided for each ECal module type, as well as a table listing the swaps that were determined.

It should be noted that, as most of the subtracted plots are presented in the single view only [2], some of the swaps listed in the tables will not correspond to the channels observed in the plots. During the analysis, a complete set of single/downstream/upstream view plots were produced and analysed, but only the single sided views are presented in this section to avoid an oversaturation of plots, and also as the single sided plots contain most of the key information.

[2] The side right module and DsECal modules are presented in the downstream view.

Barrel Bottom Left

Pre Swap		Post Swap	
Bar Number	Layer Number	Bar Number	Layer Number
77	20	77	22
71	0	68	6
71	2	68	4
71	4	68	2
71	6	68	0
70	0	69	6
70	2	69	2
70	4	69	4
70	6	69	0

Table 5.5: Bar and layer numbers for Barrel Bottom Left ECal.

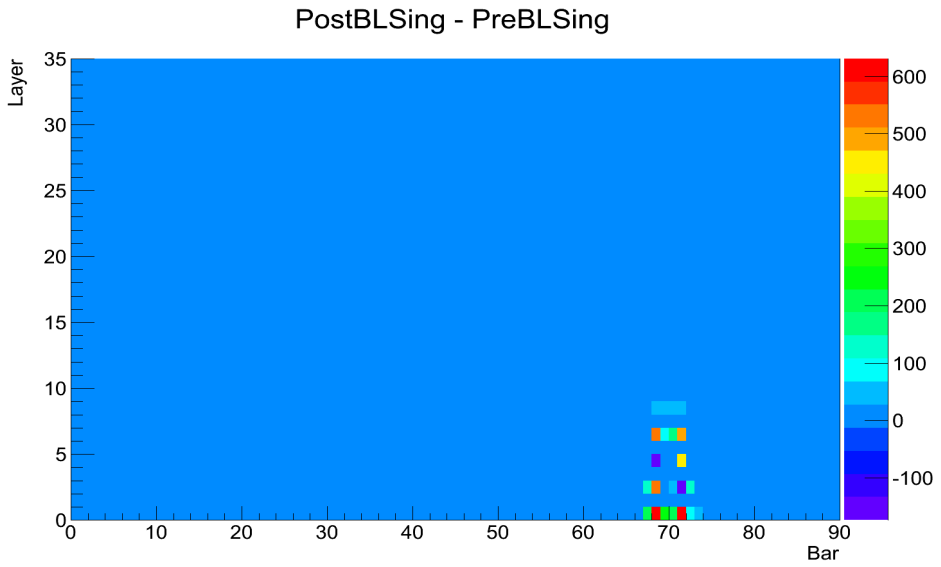

Figure 5.7: Bar/Layer subtracted plot for RMM4 which corresponds to the barrel bottom left ECal module. The plot is a single-ended view where the z-axis is the difference in channel hits.

All the swaps have been observed except for Bar# 77 Layer# 20 and Bar# 77 Layer# 22.

Side Left

Pre Swap		Post Swap	
Bar Number	Layer Number	Bar Number	Layer Number
23	0	23	2
82	30	83	24
83	16	83	18
19	5	19	7
29	19	29	23

Table 5.6: Bar and layer numbers for Barrel Side Left ECal.

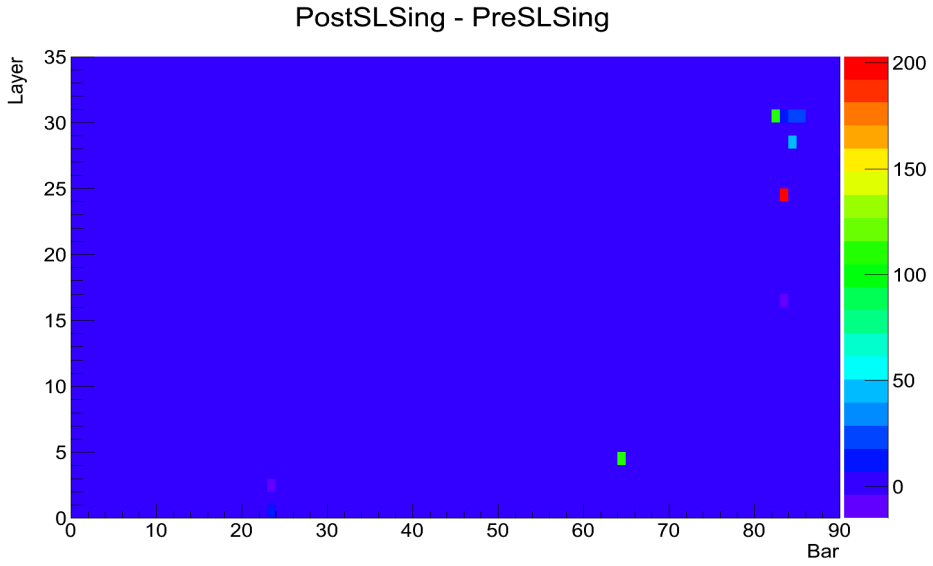

Figure 5.8: Bar/Layer subtracted plot for RMM5 and RMM6 which corresponds to the barrel side left ECal module. The plot is a single-ended view where the z-axis is the difference in channel hits.

For the barrel side left ECal module all the swaps were seen except for a single channel, bar# 83 and layer# 18, a few anomalous channels were also observed.

Top Left

Pre Swap		Post Swap	
Bar Number	Layer Number	Bar Number	Layer Number
0	24	2	24
0	16	2	18
4	16	5	18
1	18	3	18
4	18	5	22

Table 5.7: Bar and layer numbers for Barrel Top Left ECal.

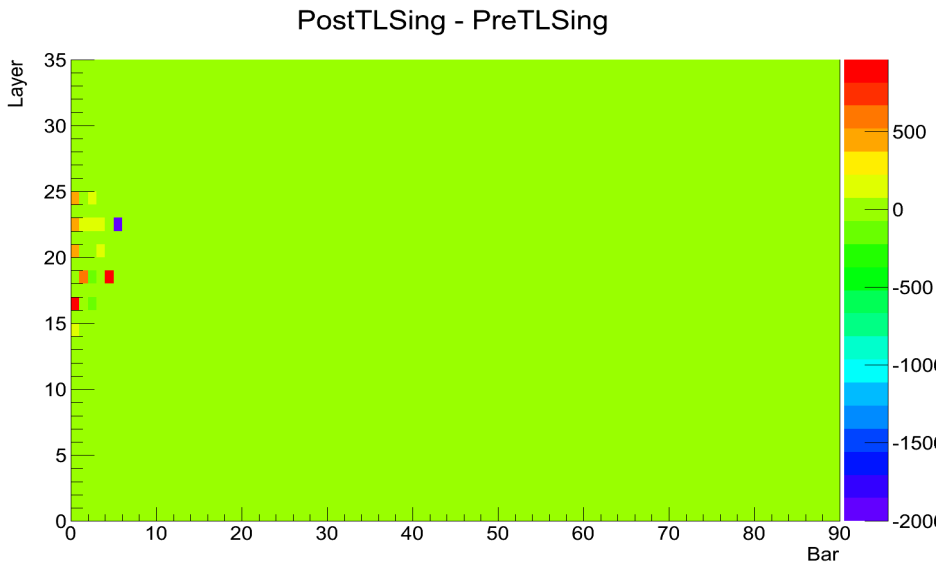

Figure 5.9: Bar/Layer subtracted plot for RMM3 which corresponds to the barrel top left ECal module. The plot is a single-ended view where the z-axis is the difference in channel hits.

For RMM3, the barrel top left ECal module, all swaps were observed in the Bar/Layer space subtracted plot except for a single swap corresponding to a bar value of 0 and a layer number of 24 being swapped with bar number 2 and layer number 24. There was also a single anomalous channel seen in blue.

Bottom Right

Pre Swap		Post Swap	
Bar Number	Layer Number	Bar Number	Layer Number
32	14	33	10
10	18	10	20

Table 5.8: Bar and layer numbers for Barrel Bottom Right ECal.

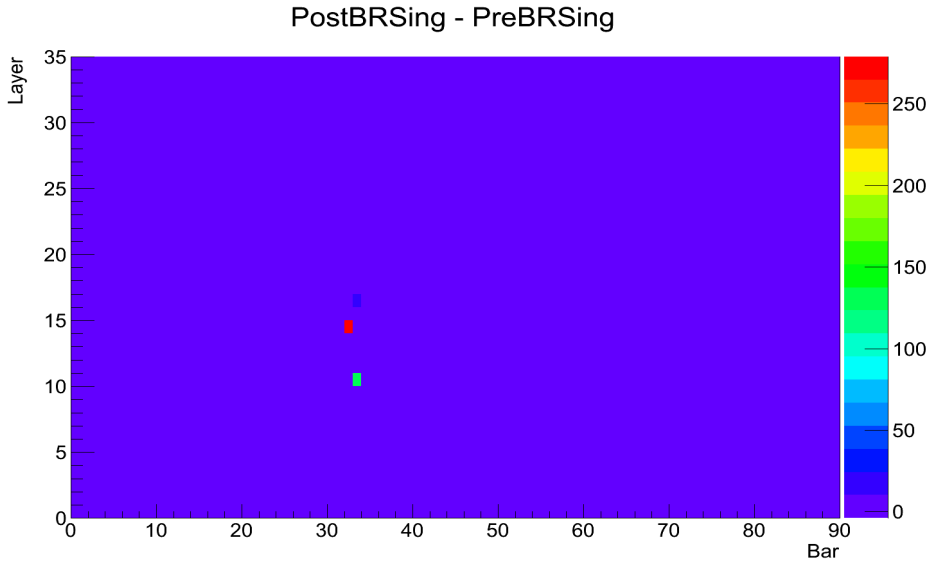

Figure 5.10: Bar/Layer subtracted plot for RMM10 and RMM11 which corresponds to the barrel bottom right ECal module. The plot is a single-ended view where the z-axis is the difference in channel hits.

Only one swap was not observed for the barrel bottom right ECal module: bar# 10 and layer# 18 being swapped with bar# 10 and layer# 20.

Side Right

Pre Swap		Post Swap	
Bar Number	Layer Number	Bar Number	Layer Number
48	3	49	1
42	29	43	27
30	15	31	11
87	8	87	10
86	16	86	18
7	11	7	13

Table 5.9: Bar and layer numbers for Barrel Side Right ECal.

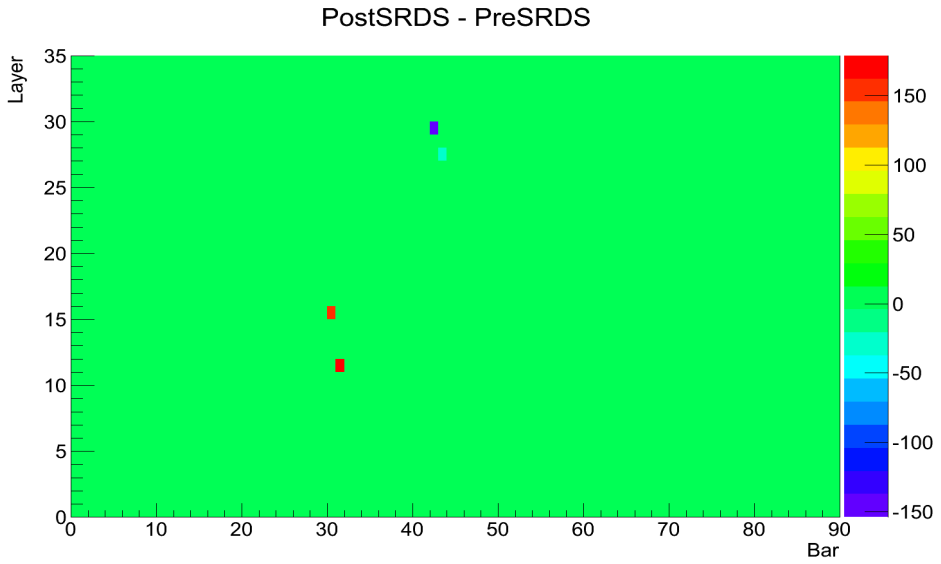

Figure 5.11: Bar/Layer subtracted plot for RMM9 which corresponds to the barrel side right ECal module. The plot is a single-ended view where the z-axis is the difference in channel hits.

All of the swaps were observed in the Bar/Layer subtracted plot for the barrel side right ECal module.

DsECal

Pre Swap		Post Swap	
Bar Number	Layer Number	Bar Number	Layer Number
27	8	29	8
7	19	5	23
21	19	26	21

Table 5.10: Bar and layer numbers for Downstream ECal.

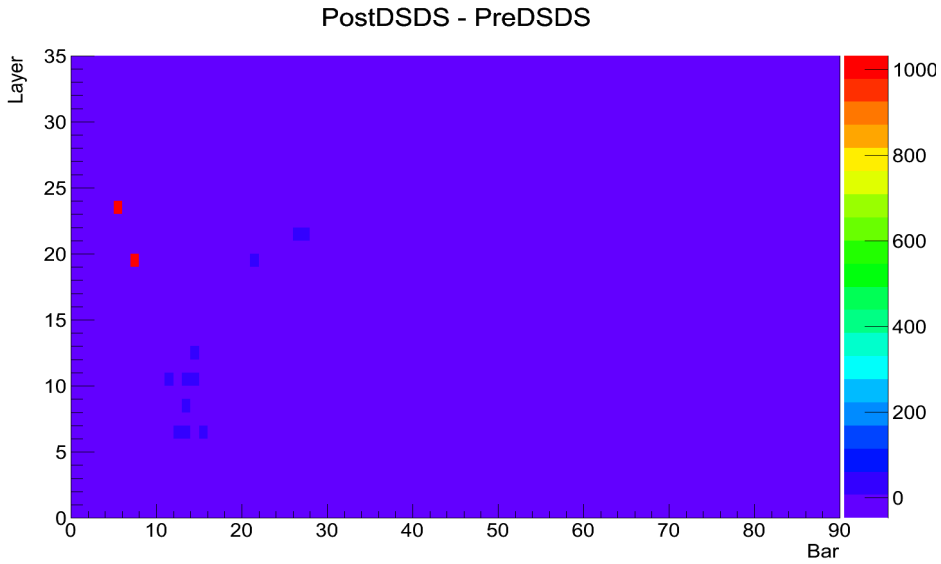

Figure 5.12: Bar/Layer subtracted plot for RMM0 which corresponds to the DsECal module.

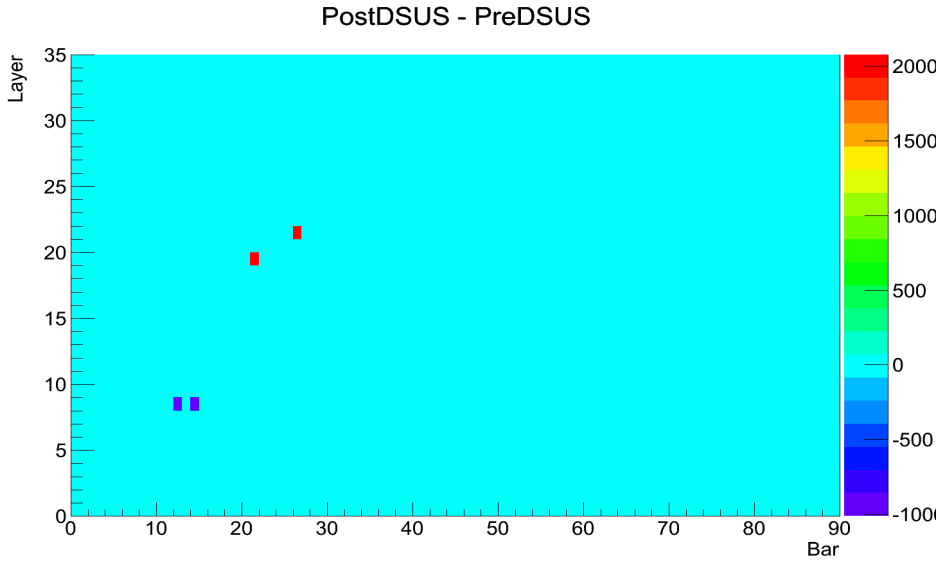

Figure 5.13: Bar/Layer subtracted plot for RMM0 and RMM1 which correspond to the DsECal module.

5.4.6 Conclusions

The subtracted Bar/Layer space plots, along with the pre/post swap hit maps, show that the swaps make a clear improvement, this was further shown by the Bar-to-Bar calbration plots that are included in Section 5.5.

There are some channels that were absent in the subtracted plots and the reason for this could be lack of statistics. The ND280 reconstruction package *ecalRecon* requires at least 3 hits for a hit cluster, therefore a track might not be reconstructed if there are not enough hits. In addition, noise could be another reason why we do not see certain channels. As well as this, there were a few examples of new anomalous channels, as listed in Table 5.11. The original analysis by no means computed an exhaustive list of mismapped channels, so a future analysis to explore the channels further would be beneficial.

Module	Bar	Layer
Top Left	6	23
Side Left	65	5
Side Left	85	28
Side Left	85	30
Side Right	27	3
DsECal	34	17
DsECal	13	8

Table 5.11: Details of the new anomalous channels that were observed. The list is not exhaustive and a future analyser may discover further channel discrepancies.

For the mismapped channel analysis presented in this thesis, the validation was reasonable and so to finalise the investigation, the swapped channel tables were committed to the software ready for Production 8.

5.5 Bar-to-Bar Calibration

5.5.1 Overview

The ECal (see Section 4.7.7 for a more detailed description of the detector) needs to be properly calibrated in order to perform at a high-quality and consistent level. It is essential that all bars in the ECal have a uniform response to equal amounts of energy deposited as a variation in the amount of energy recorded by the scintillator bars can cause an effect on certain outputs such as energy reconstruction and clustering.

5.5.2 Scintillator bars

The scintillator bars [105] used for the Ecal modules were fabricated at FNAL and are mainly composed of doped polystyrene (Poly(1-phenylethane-1,2-diyl), $(C_8H_8)_n$). In addition to the polystyrene, the scintillator bars are doped with two scintillating compounds that actuate a two stage photon emission process: PPO (2,5-Diphenyloxazole, C_15H_11NO), added at a 1% level to the polystyrene and 1,4-bis(5-phenyloxazol-2-yl)benzene, which is commonly known as POPOP ($C_24H_16N_2O_2$), is added to the polystyrene at an 0.03 % level. The first doping compound, PPO, releases photons mainly in the 340 - 400 nm wavelength region; these photons are highly attenuated by the scintillator bars themselves therefore a two-stage doping process is required. POPOP acts as a wavelength shifter, absorbing the photons emitted and re-emitting them with an energy distribution that peaks at 410 nm, a photon wavelength that is not so readily attenuated by the bars.

5.5.3 Data sample

A sample of through-going cosmic muons is used to investigate the amount of energy recorded by the scintillator bars. Cosmic muons are ideal for calibration purposes as they are a well understood control sample, plentiful and behave like Minimum Ionising Particles (MIPs); they deposit approximately the same amount of energy in each bar they pass through. Figure 5.14 shows a charged particle travelling through several bars in an ECal.

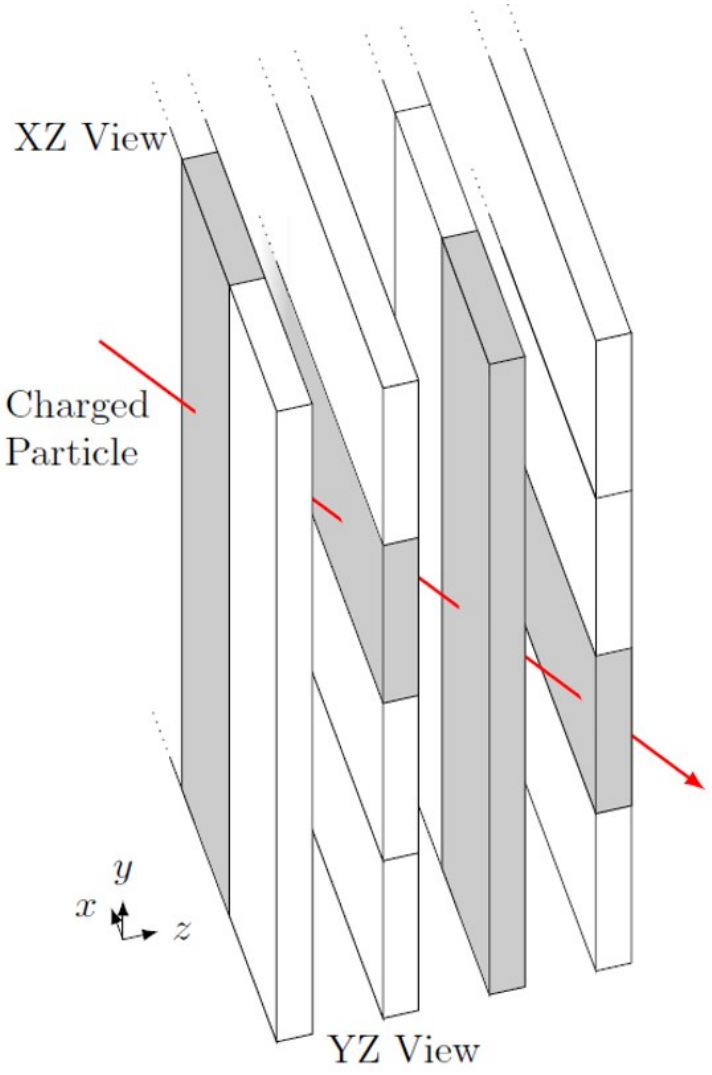

Figure 5.14: A schematic showing a charged particle traversing multiple bars in the ECal [106].

The mean rate of energy loss of heavy charged particles, including muons, is given by the Bethe-Bloch formula [2]:

$$-\frac{dE}{dx} = Kz^2\frac{Z}{A}\frac{1}{\beta^2}\left[\frac{1}{2}ln\frac{2m_ec^2\beta^2\gamma^2T_{max}}{I^2} - \beta^2 - \frac{\delta(\beta_\gamma)}{2}\right] \tag{5.1}$$

where

- $T_{max} \simeq 2m_ec^2\ \beta^2\ \gamma^2$
- $K = 4\pi N_A r_e^2 m_e c^2$
- N_A is Avogadro's number
- r_e is the classical electron radius
- I is the mean excitation energy
- $\delta(\beta_\gamma)$ is the density effect correction to the ionisation energy loss

When a particle hits a scintillator bar, scintillation light is produced and collected by the WLS fibres and transported to the MPPCs. The light yield that is recorded requires two corrections to be applied: a path length difference in a scintillator layer, as particles with longer path lengths will deposit more energy in the same length, and secondly a correction for the angle travelled by the charged particle track through the bar.

5.5.4 Calculating bar-to-bar constants

The first step in the calibration is to calculate the average response for each bar. An example of the hit charge fitted with a Landau-Gaussian for a bar in the DsECal is shown by Figure 5.15. A histogram for each bar is filled with the charge of all the hits in that bar, where each hit is corrected for how far it was from the sensor at the end of the bar and the path the track took through the bar. This gives a charge spectrum for each bar that is then fitted with a Landau Gaussian function. The energy loss of particles passing through a scintillator layer varies from particle to particle, so the distribution of energy deposits forms a Gaussian-like distribution but one that is more skewed (Landau-like) for thin scintillator layers,such as that for the DsECal and Barrel ECal scintillator planes. The measured energy is plotted in MEU (MIP Equivalent Units) for each channel and fitted with a Landau Gaussian to produce a most probable value (MPV) for each channel. Each bar is corrected so that the average energy recorded

by a bar is divided by the average energy recorded for all the bars of the same type (orientation and module). The uncertainty on the MPV, σ is given as:

$$\sigma = \frac{MPV}{\sqrt{N}} \tag{5.2}$$

where N is the total number of hits.

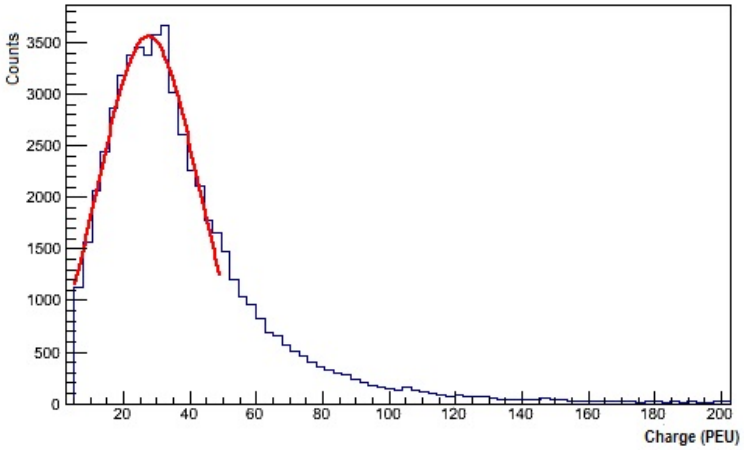

Figure 5.15: Energy spectrum for cosmic muons.

The calibration is performed on both the Barrel ECal and DsECal on a hit-by-hit basis, the results for run 7 and run 8 are shown in Figure 5.16. Each green block is composed of points before the bar equalisation calibration is applied. The first 2 green blocks correspond to double-ended bars only while the rest correspond to a mixture of single-ended and double-ended bars. The blue points are produced after the calibration is applied and each horizontal band corresponds to a different RMM. The P0D ECal RMMs are calibrated by a different method, therefore they are not included in the results. It should be noted that with the implementation of the swapped channels as explained in Section 5.4, there are fewer outliers in the bar-to-bar plots as compared to constants from previous runs.

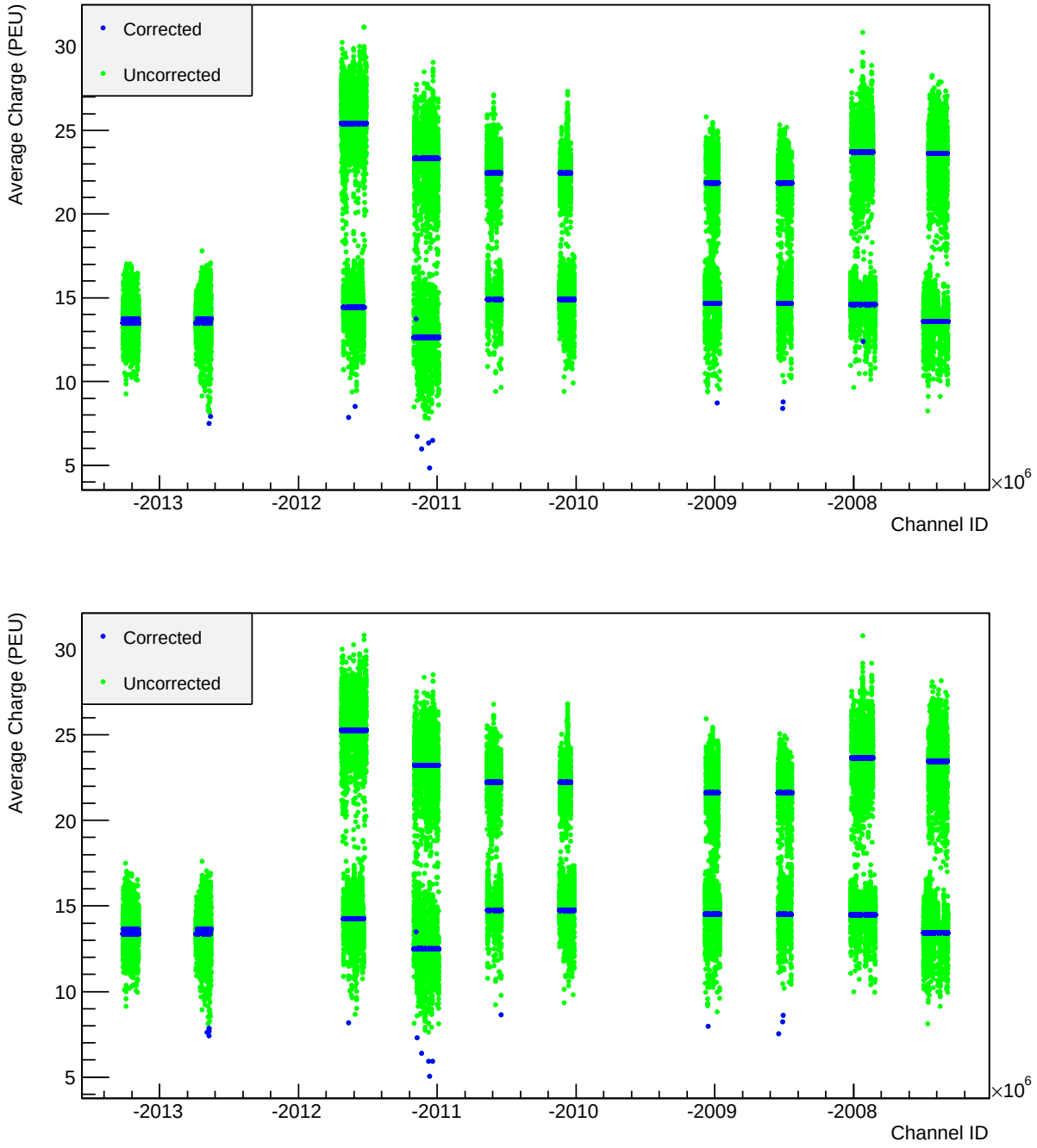

Figure 5.16: The average energy (PEU) for each bar for run 7 (top) and run 8 (bottom) bar-to-bar constants. Each blue band represents a different RMM, and is composed of blue points after the calibration has been applied. The green points show the scatter of average energy recorded. The DsECal (2 blocks at the left) contains only double ended bars, whereas the Barrel ECal contain a mixture of single and double ended bars (as represented by the rest of the blocks).

In order to validate the bar-to-bar results, calibration constants from different runs can be compared. Figure 5.17 shows the run 7 calibration constants in red, the run 8 calibration constants in blue and the difference between the two constants normalised to the run 7 constants in black. The normalised difference in the calibration constants has a narrow peak that centres on 0 which means that the constants are stable across different runs.

Once the constants have been produced and validated they are uploaded to the mySQL database. This is performed once per data run and the latest run 8 constants were uploaded in November 2017.

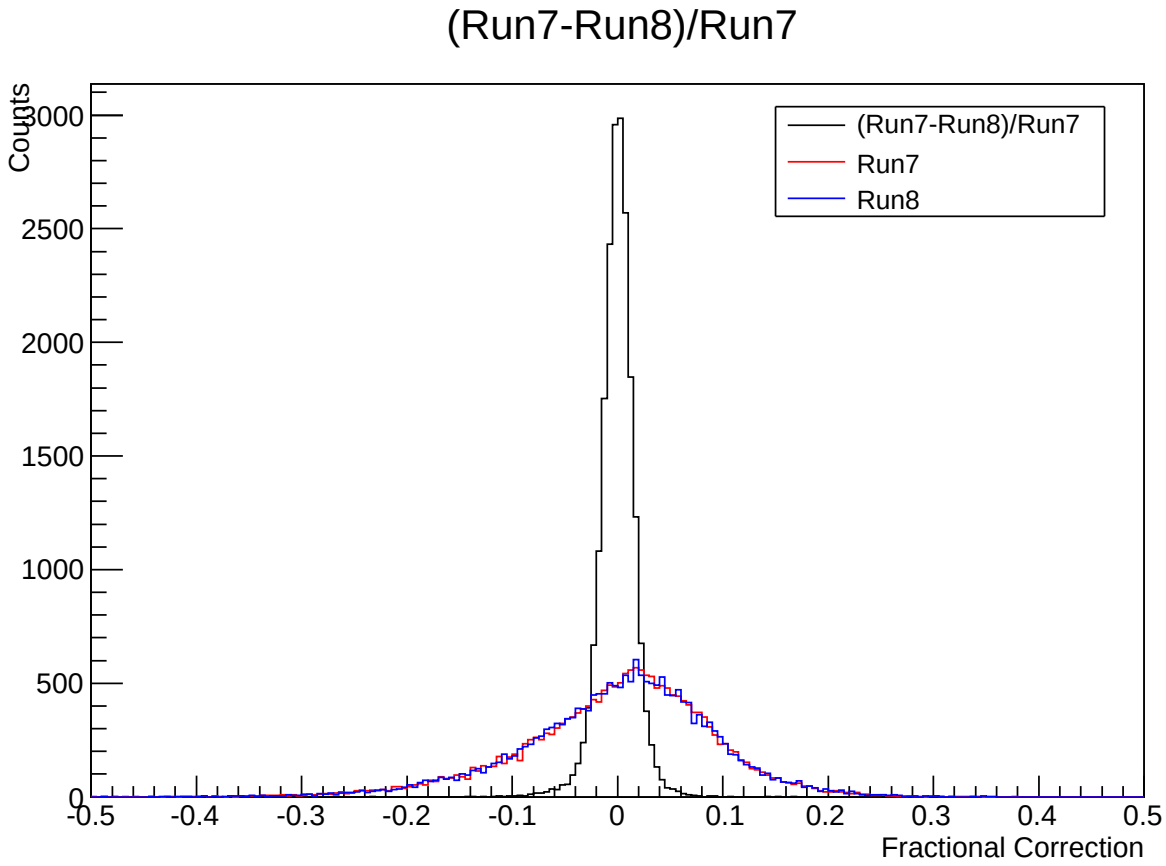

Figure 5.17: Run 7 (red) and run 8 (blue) bar-to-bar constants comparison. The black histogram shows the difference between the run 7 and run 8 constants, normalised to the run 7 constants.

Chapter 6

Vertex Activity in the FGDs

During a neutrino-nucleus interaction (Section 3 discusses these interactions), low energy particles can be produced that are below the reconstruction threshold of the detector[1] and these can impact on the kinematics of the event and lead to misidentification of the event and miscalculation of the neutrino energy during event reconstruction. If the muon kinematics are altered, the momentum of the neutrino may be incorrectly determined leading to inaccurate measurements, therefore it is essential to understand these nuclear effects better. The low energy particles produced are not observable but the detector can measure the energy they deposit around the vertex.

The Vertex Activity (VA) is defined as being the amount of energy deposited in a given region around the vertex point, including contributions from reconstructed tracks as well as short-ranged particles that are difficult to reconstruct. The VA is sensitive to final-state particles that exit the nucleus after a neutrino interaction but are not reconstructed as their energy is below the reconstruction threshold.

The VA calculation begins with a box centered on the vertex, which is the start position of the 3D fitted track, with dimensions given by: layers deep x bars [2] high x bars wide of values: 1x1x1, 3x3x3, 5x5x5 or 7x7x7. All the bars within the specified VA region are selected and the energy deposited by particles within that area is summed up to give a VA value measured in Photon Equivalent Units (PEU), where 1 MeV $\sim$ 21.7 PEU [107].

Figure 6.1 shows the VA calculation for different vertex box regions; it should be noted that, unless specified otherwise, all plots presented in this thesis have a VA region of 5x5x5. This region was identified as being the optimal size as, during reconstruction

[1] The proton momentum analysis threshold at ND280 is around 450 MeV.
[2] Information about FGD1 scintillator bars is provided in Section 4.7.5

events that deposit their energy at the edge of the box may not be detected therefore a compromise needs to be made in which the box is big enough to account for the VA that occurs during an event, but not too large as key information may be lost or the measurement may be too susceptible to noise or other such effects.

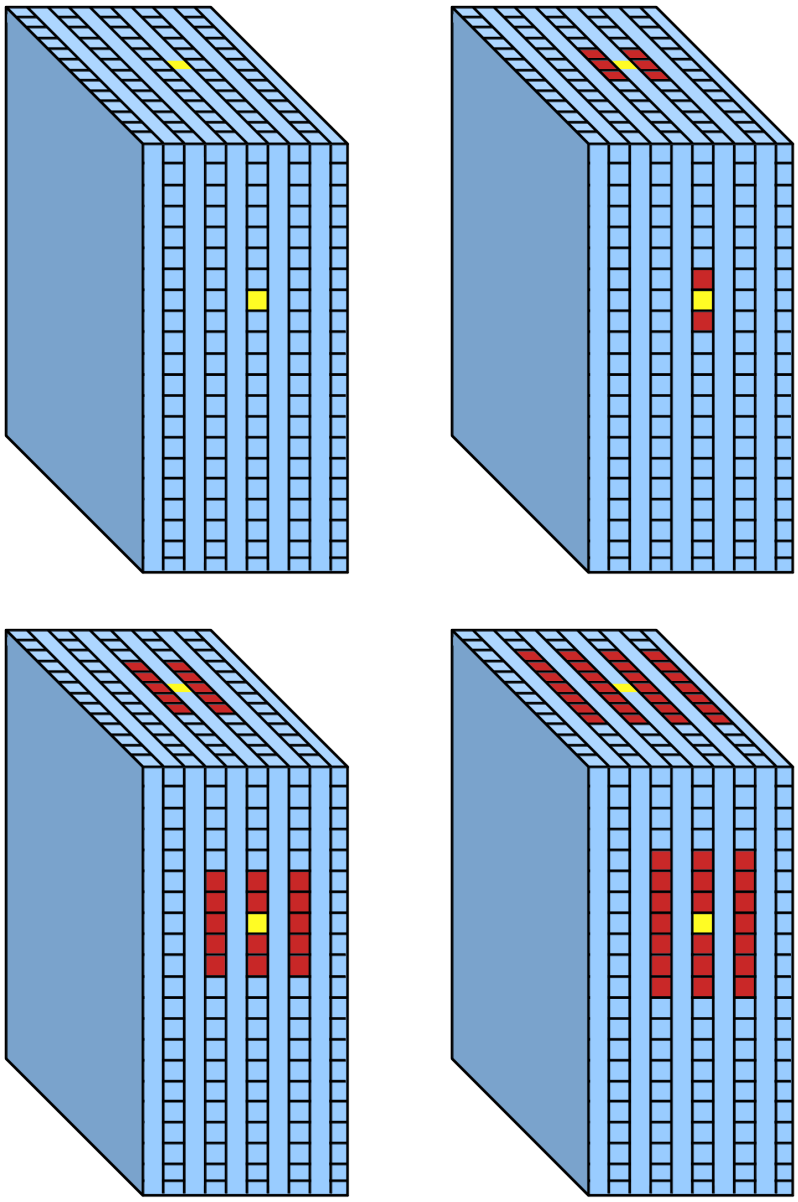

Figure 6.1: Schematics showing the definition of vertex activity, clockwise from first image, 1x1x1, 3x3x3, 5x5x5 and 7x7x7 [108].

6.1 Analysis Motivations

A large number of particles produced in neutrino interactions have a track length too short to be reconstructed (FGD reconstruction requires a track to contain at least 3 hits in order to be reconstructed), or do not enter a TPC for PID. The only way to

study short-range energy deposits is to use the VA as it is sensitive to all charged particles[3] of any track length. The VA variable was implemented into the Production 5 software with the relevant information stored in the FGD component of a Global PID in *oaAnalysis* files (discussed in Section 4.8). The VA can be used to disentangle 2p2h, 1p1h (Section 3.2 discusses these models in further detail) and further models, including ones with multiple protons, as well as being very sensitive to Final State Interactions (FSI), which have been discussed in Section 3.3.

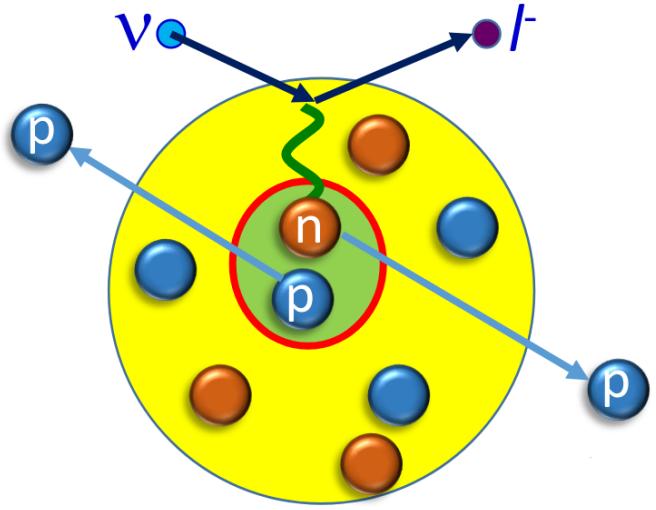

Figure 6.2: Illustration of a neutrino-nucleon interaction showing protons leaving the nucleus [109].

This analysis will look deeper into how the VA can be used to probe low energy protons that are produced in neutrino interactions in FGD1, a schematic of which is shown by Figure 6.2. Protons to first order deposit their energy at the end of the track so when they escape the VA region a smaller amount of energy will be recorded. Sometimes the momenta of protons can be so low that it is not possible to reconstruct the energy deposit as tracks, but the VA variable allows the detection of low momentum particles and is therefore a useful candidate to constrain these low energy particles that are produced in the ND280 detector during neutrino interactions.

Generators model low energies in various ways which do not necessarily agree with data, thus the need for more robust theoretical models in neutrino-nucleus interactions is essential. Uncertainties from neutrino–nucleus interactions will be the major source of systematic uncertainty in the next generation neutrino oscillation experiments, therefore by improving our understanding of nuclear effects, the systematic uncertainties on cross section measurements can be reduced, which will ultimately lead to improved determination of oscillation parameters [110].

[3] Any neutral particle or an NC event (discussed in Section 3.1.3) will not affect the VA and neutrons will have a negligible effect on the VA.

6.2 Muon Neutrino Sample

The inclusive muon neutrino sample begins with a reconstructed forward going muon starting within the FGD1 Fiducial Volume (FV) and with no reconstructed pions, and is then split into the following subsamples: CC0π, CC1π^+ and CCother, depending on the number of pions and charge [111]. All the MC samples are processed with production 6B which corresponds to NEUT version 5.3.2 [55], which uses the Llewellyn-Smith model [61] coupled with the Spectral Function (SF) model and 2p2h contributions from the Nieves model [112], and GENIE version 2.8.0, which does not include any 2p2h contributions and uses the Relativistic Fermi Gas (RFG) model [113].

MC generator	version	Nuclear model	2p2h model	M_A	FSI
NEUT	5.3.2	SF	Yes, Nieves	1.21	Cascade
GENIE	2.8.0	RFG	No	0.99	Empirical (hA)

Table 6.1: A summary of MC generators and the models associated with them.

The data sample used for this analysis includes runs 2-4 which correspond to data collected between November 2010 and April 2013 with run 1 excluded as the BarrelECal had not been fully installed at the time. Table 6.2 shows the data POT used for the runs specified and "water in" and "water out" periods are named as such depending on whether the PØD contained water or not.

T2K Run	Data POT (x 10^{20})
Run 2 (water in)	0.429
Run 2 (water out)	0.355
Run 3b (water out)	0.215
Run 3c (water out)	1.348
Run 4 (water in)	1.627
Run 4 (water out)	1.762
Total POT	5.736

Table 6.2: The statistics in neutrino mode used in this analysis for data.

The MC samples were generated using a flux prediction that takes into account the beam conditions for each run; the total POT for NEUT MC was 5.744 x 10^{21} and for GENIE MC was 6.146 x 10^{21}.

For all the plots in this chapter, the MC is normalised to the data using POT (unless specified otherwise) and a set of corrections were applied to both data and MC in order to reduce any discrepancy observed; these corrections were performed using the highLAND2 framework v2r7 and are listed in Table 6.3.

Correction
de/dx applied to data and MC
Data Quality
Momentum resolution
TPC particle identification (PID)
FGD PID
TPC cluster efficiency
TPC tracking efficiency
TPC charge misassignment
TPC-FGD matching efficiency
TPC-ECal matching efficiency
TPC-PØD matching efficiency
FGD-ECal matching efficiency
FGD-ECal-SMRD matching efficiency
ECal tracking efficiency
ECal PID
FGD tracking efficiency
Michel electron efficiency
Out of FV (OOFV)
Pile-up
Pion secondary interactions
Proton secondary interactions

Table 6.3: A list of the corrections applied to the data and MC samples for the muon neutrino sample.

This thesis does not deal with a muon neutrino selection therefore only a brief description of each cut will be provided, for further details please see [114]. The standard cuts used in the muon neutrino CC inclusive sample for FGD1 were applied to this analysis in order to select ν_μ charged-current events that are well reconstructed:

- **Event quality:** the full spill must contain a good global ND280 data quality flag.
- **Bunching:** a group of tracks belonging to a specific beam packet are known as a bunch, and events must occur within the particular bunch time window of the neutrino beam. Neutrino interactions in two different bunches within a beam spill are considered as two separate events, in order to reduce the risk of pile-up events. The bunch width for data is around 15 ns; tracks are associated within a bunch if they deviate from the centre of the bunch by less than 60 ns (4 x 15 ns = 4 σ).
- **Track multiplicity:** there must be at least one reconstructed track in FGD1.
- **TPC track quality:** good reconstruction quality is required for tracks with a TPC segment. All TPC tracks should have more than 18 hits.
- **Muon candidate search:** the muon is identified as being a negatively charged track with the highest momentum starting in the FGD1 FV. This FV does not ensure that every event has been encompassed in FGD1 so a further cut will be applied which will be discussed in the following subsection.
- **PID:** The PID in the TPC is based on the dE/dx variable which measures energy loss. The muon candidate will have a muon-like PID based on the pull value:

$$Pull_i = \frac{\frac{dE}{dx}_{measured} - \frac{dE}{dx}_{expected}, i}{\sigma_{\frac{dEdx_{measured}}{dEdx_{expected}}}, i} \tag{6.1}$$

where i = e, μ, p or π.

Discrimination functions are used to reject certain particle types:

$$L_i = \frac{e^{-Pull_i^2}}{\sum_{i=e,\mu,p,\pi} e^{-Pull_i^2}} \tag{6.2}$$

Proton and pions are removed by the following condition:

$$\begin{aligned} L_\mu &> 0.05 \\ L_\pi &> 0.3 \end{aligned} \tag{6.3}$$

Electrons with p $<$ 500 MeV/C are rejected by:

$$L_{MIP} = \frac{L_\mu + L_\pi}{1 - L_p} > 0.8 \tag{6.4}$$

- **Entering backgrounds cut:** events with mis-reconstructed tracks are removed.

Figure 6.3 shows the distributions of muon angle for the muon neutrino sample and Figure 6.4 shows the momentum distribution for the muon neutrino CC-inclusive selection using NEUT MC. The MC is separated into different topologies[4]:

- **CC-0π:** Events with a true negative muon and zero pions in the FSI.
- **CC-1π:** Events with a negative muon and 1 neutral or charged pion (also includes events with kaons).
- **CC-Other:** Any other CC event, not included in the previous CC samples, containing a negative muon and $>$ 1 neutral or charged pion.
- **Background:** consisting of CC and NC neutrino interactions.
- **External:** Events where the interaction vertex is outside of the FGD1 FV.

6.2.1 Vertex Activity Analysis Cuts

For the VA analysis, FGD1 is used as a target only and additional tailored cuts were applied as follows:

- **Cut 1:** Single track TPC events only are selected
- **Cut 2:** The FV is modified so that only the last 2 layers of FGD1 are excluded, as shown by Table 6.4.

	x_{min}	x_{max}	y_{min}	y_{max}	z_{min}	z_{max}
FGD1	-874.51	874.51	-819.51	929.51	136.25	426.125

Table 6.4: FV values for FGD1.

The FV was modified to exclude two FGD1 bars in the z direction, the final two downstream layers, as well as five FGD1 bars in the x and y directions, to ensure that the bars present in the VA region do not correspond to any bars close to the edge of the detector.

[4] A topology is classified as a set of particles that leave the nucleus after an interaction.

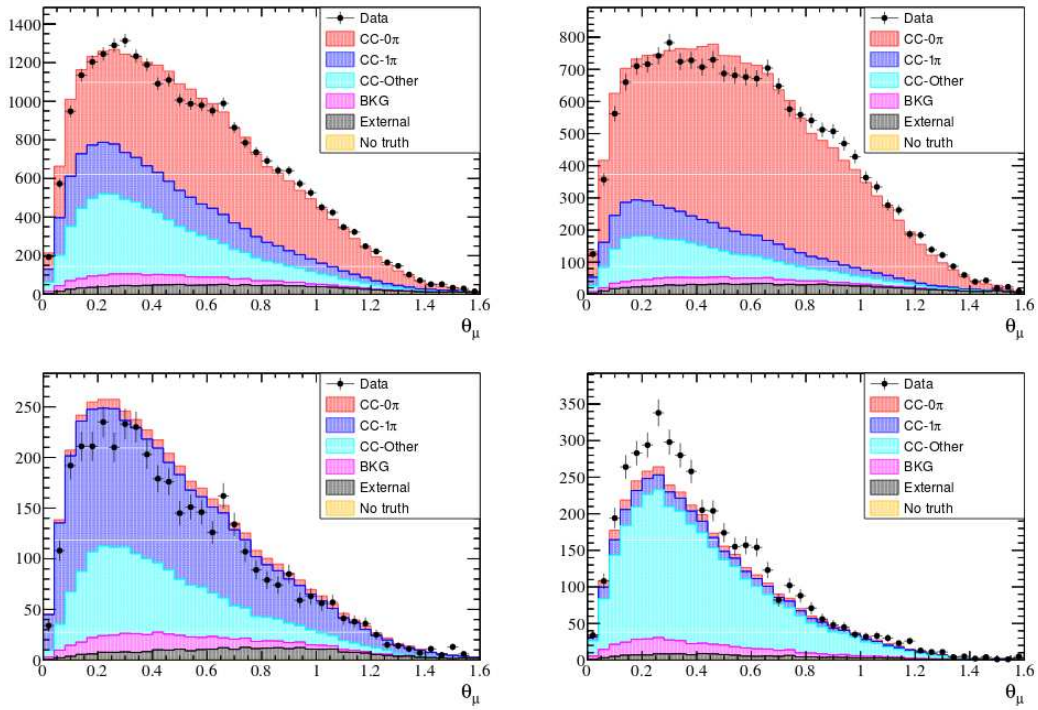

Figure 6.3: The muon angle distribution for different FGD1 samples: CC-inclusive (top left), CC-0π (top right), CC-1π (bottom left) and CC-other (bottom right), separated by topologies [114].

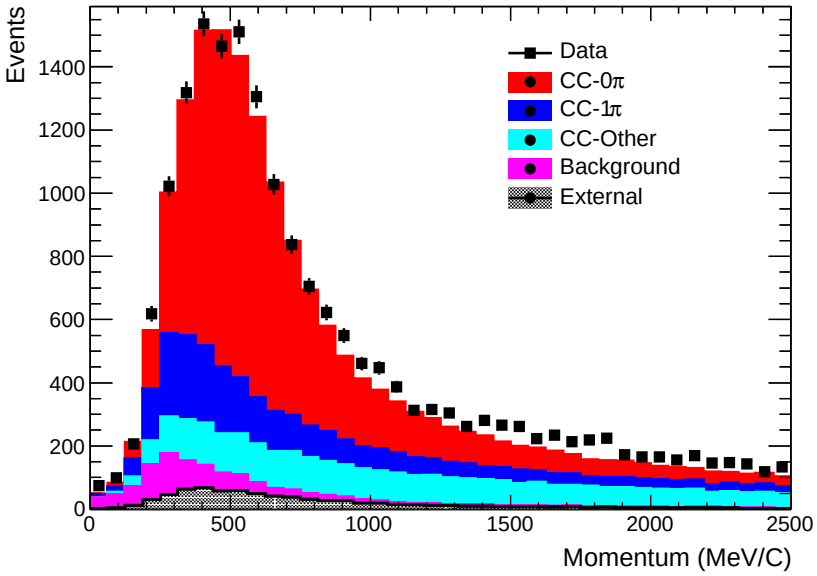

Figure 6.4: The muon neutrino momentum distribution for runs 2-4 where NEUT is used as the MC sample.

Muon Neutrino Sample Discrepancy

The VA for the muon neutrino sample using NEUT MC separated into topologies is given by Figure 6.5 for the different vertex regions. The plots show that there is a discrepancy present in data and MC at low VA for each vertex region whereas for the higher VA region the discrepancy is not seen. The discrepancy appears to be greater at larger box regions, 5x5x5 and 7x7x7, and significantly worse at low VA than seen with 3x3x3.

Figure 6.6 shows the VA for different NEUT interaction modes, and it is clear from these plots and the interaction percentages shown in Table 6.5, that the CCQE-like interaction mode (CCQEL, see Section 3.1 for an explanation of different neutrino interaction modes) is dominant and that the discrepancy likely occurs from events in this mode.

The discrepancy in low VA for the ν_μ sample was an unexpected result. The next stage involved understanding why the discrepancy occurs, by firstly looking at the VA for the $\bar{\nu}_\mu$ sample in the next section, then followed by studies investigating the detector response in Section 6.2.3.

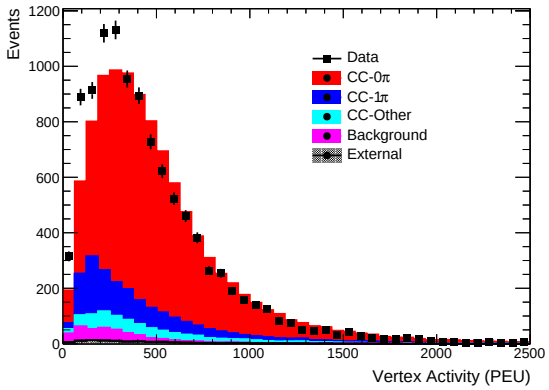

(a)

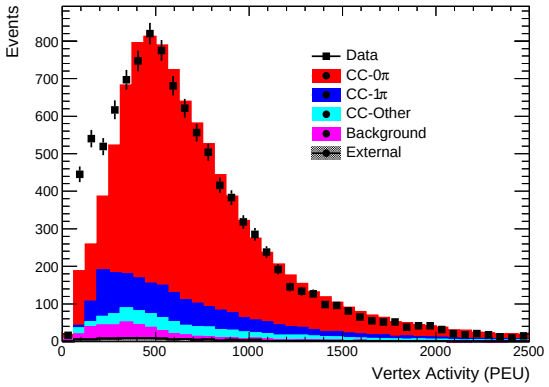

(b)

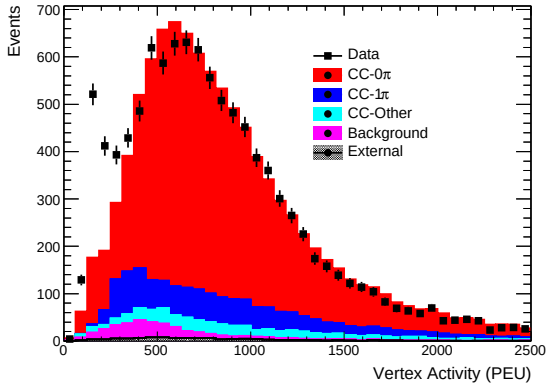

(c)

Figure 6.5: Muon neutrino vertex activity for data and NEUT MC separated into different box sizes: (a) 3x3x3 (b) 5x5x5 (c) 7x7x7.

Interaction mode	NEUT (%)
QEL	63.32
COH	1.82
RES	21.47
DIS	0.42
BG	3.91
2p2h	9.07

Table 6.5: The breakdown in percentage of interaction modes for NEUT MC.

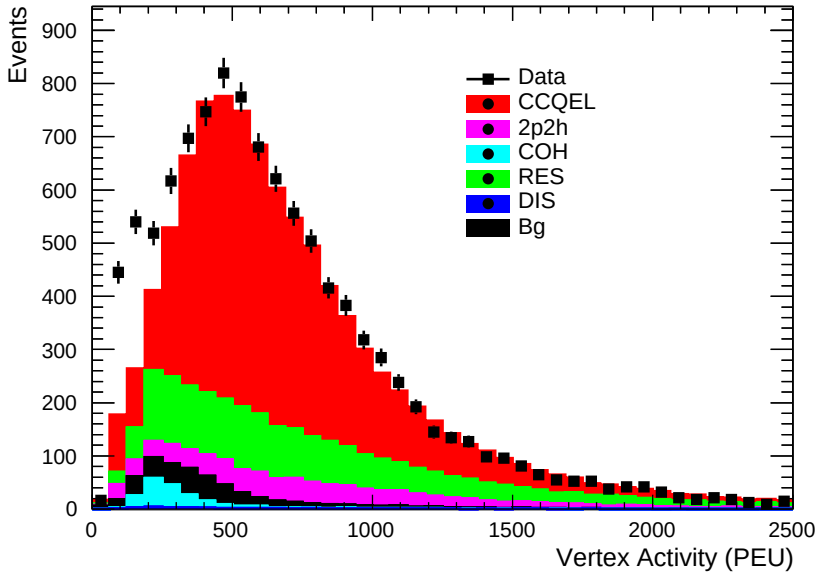

Figure 6.6: Vertex activity of the muon neutrino sample separated by interaction modes using NEUT MC, for the 5x5x5 vertex region.

6.2.2 Muon Antineutrino Sample

The muon antineutrino sample used in this section comprises of data collected from runs 5c (the first RHC mode at T2K) to runs 6e, this corresponds to data collected from June 2014 to June 2015, and is described in Table 6.6. For the MC sample NEUT version 5.3.2 was used with a total POT value of 3.962x10^{20}.

T2K Run	Data POT (x 10^{19})
Run 5c	4.298
Run 6 (b+c+d+e)	34.023
Total POT	38.321

Table 6.6: The table shows data POT values in antineutrino mode used in this analysis.

Events were selected using the standard muon antineutrino sample, where very pure $\bar{\nu}_\mu$'s can be obtained by tagging postive muons, which requires events to be in-time with proton bunches and for the data quality to be from a good global ND280 data quality flag. The following are the selections applied for the muon antineutrino sample, for a more detailed discussion of the cuts, the reader is referred to [115]:

- **Event quality:** the full spill must contain a good global ND280 data quality flag and occur in a defined timing bunch.
- **Total multiplicity:** there must be at least one reconstructed track in TPC2.
- **Positive multiplicity and fiducial:** the positive muon is defined as being the positively charged track with the highest momentum starting in the FGD1 FV. The track must consist of more than 18 TPC nodes.
- **TPC1 veto:** there must be no reconstructed tracks in TPC1. PØD, magnet and FGD1 interactions with backward tracks are vetoed.
- **External FGD1:** muons originating upstream of FGD1, that are misreconstructed into two separate tracks (muon track is split into PØD-TPC1-FGD1 and FGD1-TPC2..) due to muon large-angle scattering, are rejected. If the second highest momentum track begins $<$ 150 mm upstream of the muon candidate, the event is rejected.
- **TPC PID:** using the discriminant variables defined in equation 6.2, the highest momentum positive muon candidate will have: $0.1 < \mathrm{L}_\mu < 0.7$ and $\mathrm{L}_{MIP} > 0.9$, if $\mathrm{p} < 500$ MeV/c.
- **Kinematic selection**: The muon candidate must have a momentum in the range of 0.2 - 5 GeV/c and $\cos\theta_\mu > 0.2$.

The distributions of p_μ and $\cos\theta$ for the muon antineutrino sample is given by Figure 6.7.

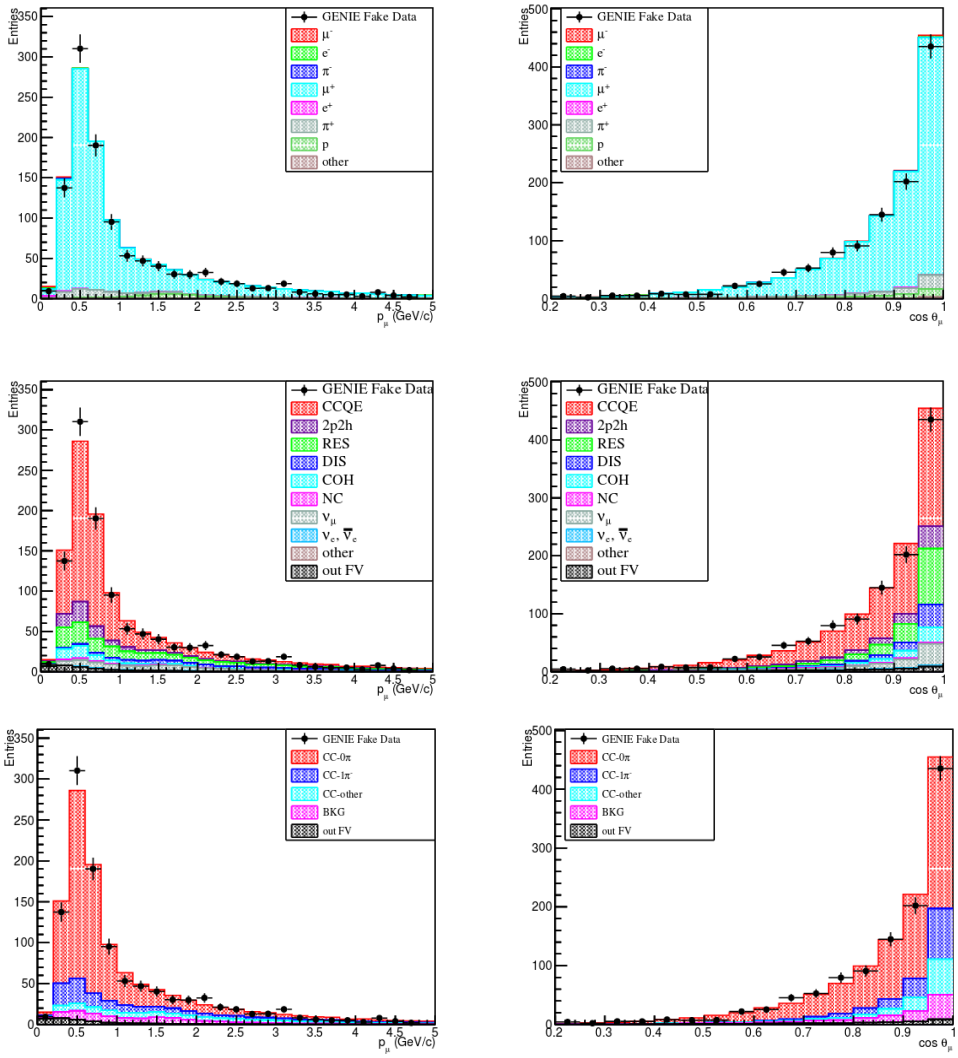

Figure 6.7: POT normalised MC to data distributions of p_μ (left) and $\cos\theta$ (right) for the $\bar{\nu}_\mu$ sample from runs 5c to 6e. The top plots show contributions from different true identities of the μ^+ candidate, middle shows the flavour of the interacting neutrino and the bottom distributions have been separated into different event topologies. Figure and caption from [116].

As with the ν_μ sample, two additional cuts were added in order to tailor the sample for the VA analysis (Section 6.2.1); the VA distribution after these cuts were applied is given by Figure 6.8 for different VA box sizes.

There is no discrepancy observed in the $\bar{\nu}_\mu$ sample for any of the vertex regions unlike in the ν_μ sample. For the $\bar{\nu}_\mu$ sample, the VA peaks at a lower region than the ν_μ VA, because the $\bar{\nu}_\mu$ contains a neutron in the final state. The different vertex regions also show that the mean VA shifts towards the high VA region as the vertex box increases in size, a larger box size means there will be more contributions from particles.

The data and MC agreement in the $\bar{\nu}_\mu$ sample is better as neutron interactions, having no associated charge, have a negligible contribution to the VA. The data and MC agreement observed in the ν_μ sample is worse as proton nuclear interactions produce VA contributions and will affect the FSI; the proton will have a different momentum than observed. The likelihood is that the proton nuclear interaction modelling is not correct in generators therefore there is a discrepancy in low VA for the ν_μ sample.

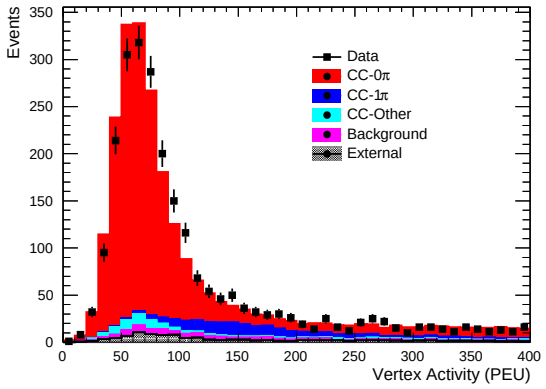

(a)

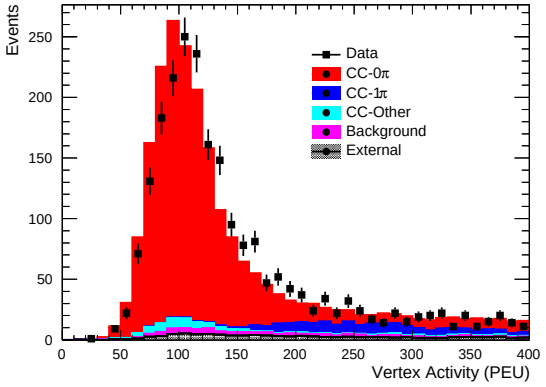

(b)

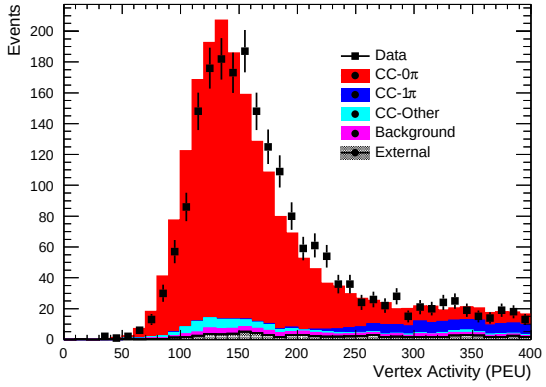

(c)

Figure 6.8: The vertex activity for the muon antineutrino sample separated into different box sizes: (a) 3x3x3 (b) 5x5x5 (c) 7x7x7. The MC generator used to produce these plots is NEUT. There is no clear data and MC disagreement for this sample, unlike in the muon neutrino sample.

6.2.3 Detector Response Studies

Once the low VA excess in the ν_μ sample was discovered and the $\bar{\nu}_\mu$ sample was investigated, the next stage was to evaluate whether or not the discrepancy occurs due to a detector effect. Many different studies were performed, some of which are included in the next section, including varying the number of TPC tracks, momentum, pull, and other variables.

Varying the Number of Selected Tracks

The first study involved varying the number of TPC and FGD-only tracks, in order to see if there are indications of extra tracks contributing towards the overall charge and making a difference to the overall VA. As mentioned previously, (Section 6.2.1), the default for the VA analysis was to select on 1 TPC track only, as this allows events that would have had a relatively low momentum proton in the CC-inclusive sample to be removed. By varying the number of TPC and FGD-only tracks, one can assess the impact that low momentum protons have on the VA.

The VA distributions with the number of TPC and FGD-only tracks varied is shown by Figure 6.9, and it can be seen that selecting the number of TPC tracks to be > 0 causes the low VA discrepancy to disappear, regardless of the FGD-only track selection cut. This suggests that the discrepancy is present for multi-track events as there is a proton present in the VA region that is misidentified. There is an overshoot in data for the higher VA regions, shown by Figures 6.9 (b) and (d), which is likely to occur due to the MC underestimating the number of particles contributing to high VA values.

After applying the cuts, selecting 1 TPC track and zero FGD-only tracks, the discrepancy in the low VA regions appears to worsen. This is expected to happen if there is a further veto on FGD1 tracks, so the overall charge contribution from the FGD1 is less, therefore the discrepancy appears to be greater.

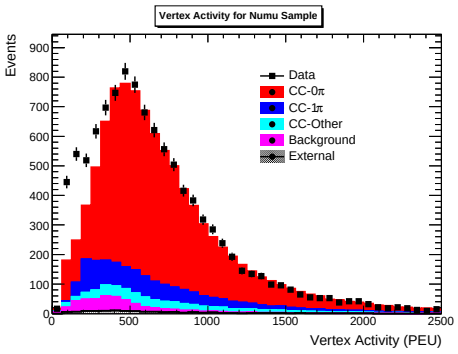

(a) TPC tracks = 1 **(default)**

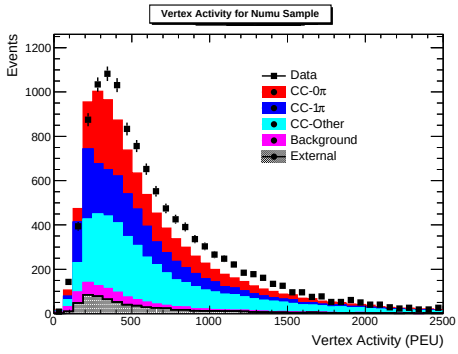

(b) TPC tracks > 1

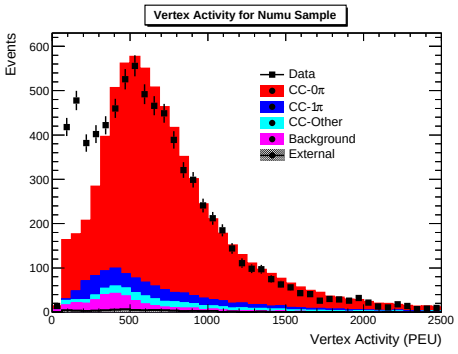

(c) TPC tracks = 1 and FGD-only tracks = 0

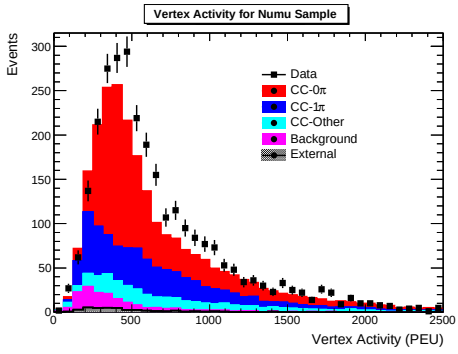

(d) TPC tracks = 1 and FGD-only tracks > 0

Figure 6.9: The impact of varying the number of TPC and FGD-only tracks on the VA distributions. Figure (a) represents the default VA track selection where the low VA discrepancy is observed, as shown previously. Adjusting the number of tracks selected has an impact on the VA distributions observed. All plots use NEUT MC.

Z Position

The +Z direction of ND280, often referred to as downstream, denotes the direction of the incoming neutrino beam. The FGD1 contains layers of alternating XZ and YZ layers of extruded plastic scintillator bars and 5760 readout channels, Section 4.7.5 describes the FGD in further detail. The purpose of this study is to investigate the VA of different FGD1 Z positions in order to see if there is any effect caused by the detector. FGD1 was separated into four equally spaced regions as shown by Figure 6.10 and Table 6.7.

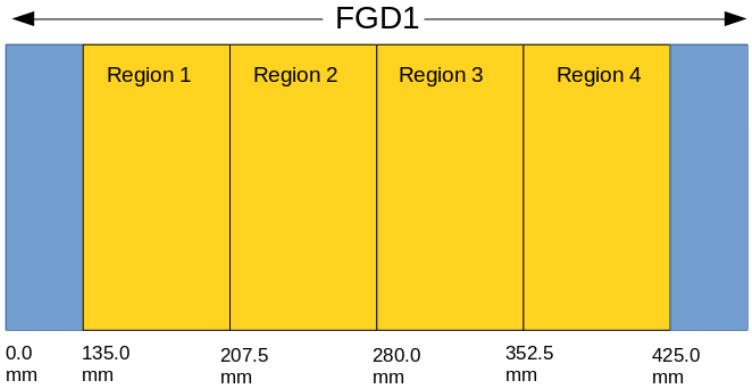

Figure 6.10: Schematic of FGD1 separated into different equally spaced Z regions. The FGD1 was separated after the FGD1 FV cut was applied, which was described in Section 6.2.1.

Region	size (mm)
1	135.0 - 207.5
2	207.5 - 280.0
3	280.0 - 352.5
4	352.5 - 425.0

Table 6.7: This table shows the values for the FGD1 Z region, separated into equally spaced sections.

Figure 6.11 shows how the VA distribution varies for each FGD1 Z position; for both MC samples the discrepancy seems to be more pronounced from region 3 onwards.

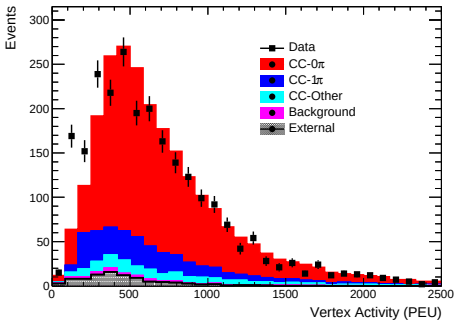

(a) Region 1: 135.0 - 207.5 mm

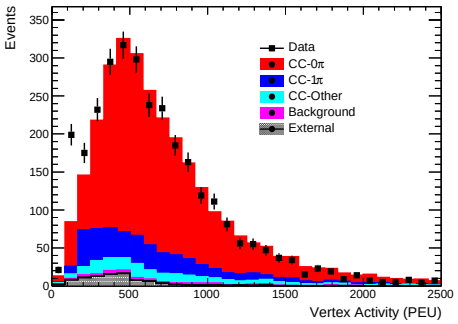

(b) Region 2: 207.5 - 280.0 mm

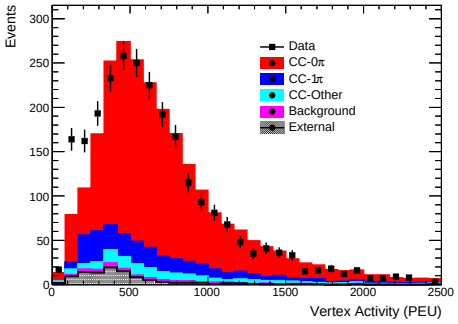

(c) Region 3: 280.0 - 352.5 mm

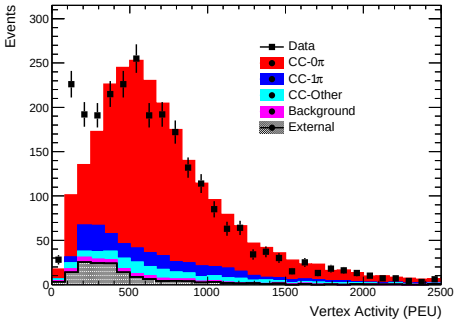

(d) Region 4: 352.5 - 425.0 mm

Figure 6.11: VA distributions for the FGD1 separated into the four different Z positions as outlined by Table 6.7. The MC used for these distributions is NEUT.

In order to see if the difference in the low VA discrepancy for each region is significant, a χ^2 test was performed for each pair of regions, and the resulting p-values can be seen in Table 6.8. The p-values suggest that there are no clear differences between any two region distributions which indicates that there is no significant issue with the detector. In addition, there are more events in region 2 (shown by Figure 6.12) than compared to the other regions which could have an effect on the VA distribution. As well as this, the number of external events is much higher for region 4, as it is closer to the edge of the detector, so this could also have an impact on the VA discrepancy. Finally, there could be additional contributing factors such as noise or certain readout channels not working as efficiently or further issues causing the discrepancy to be more pronounced as the beam travels further into FGD1.

Data regions	p-value
1 and 2	0.898303
1 and 3	0.446539
1 and 4	0.781232
2 and 3	0.847541
2 and 4	0.665813
3 and 4	0.171174

Table 6.8: This table shows the p-values comparing the data for different FGD1 Z regions.

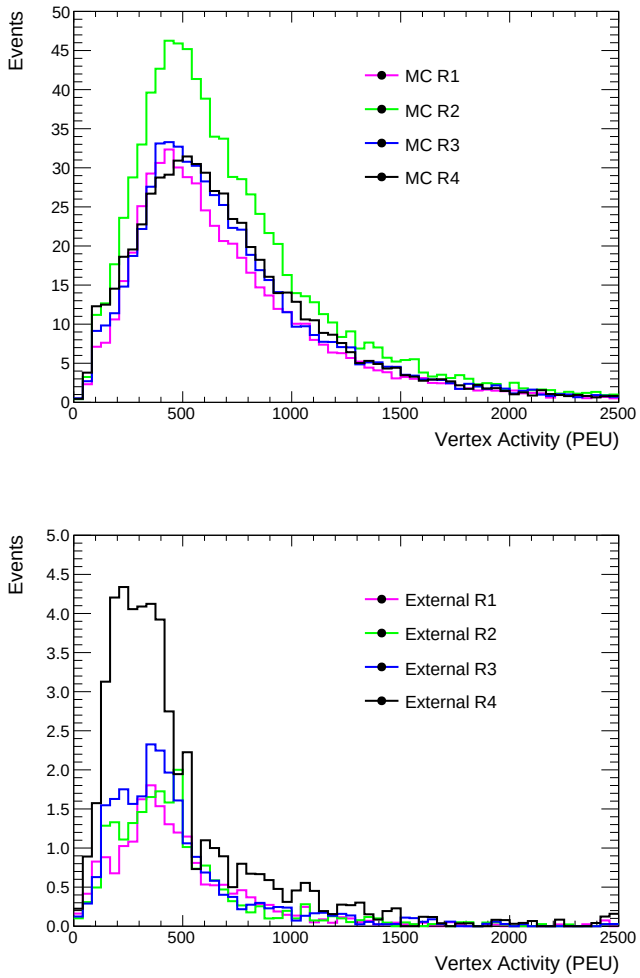

Figure 6.12: Plots showing the VA for FGD1 separated into four different z positions for NEUT, top is for all MC, bottom is for externals only. It can be seen that there are more MC events in region 2. The number of external events in region 4 is highest, this region is closest to the edge of the FGD so is more susceptible to external events.

Muon Momentum Distribution

The next study looked at the effect on the VA when the muon neutrino momentum was varied in different ranges from 200 MeV to greater than 700 MeV. The NEUT MC momentum plots are shown by Figure 6.13 and these plots show that there seems to be no clear effect on the discrepancy observed. At the lowest momentum range of 200-300 MeV there is a lack of statistics as there are less muons at this momentum range. The difference in the other momentum regions are due to the neutrino spectrum but overall there seems to be no obvious indication that the momentum affects the data and MC disagreement.

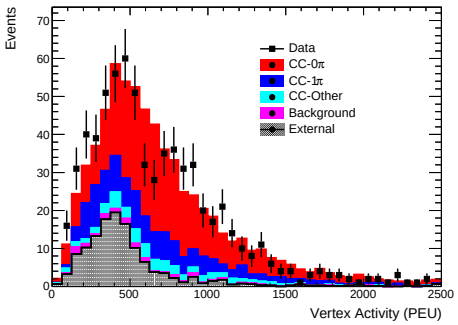

(a) Momentum = 200 - 300 MeV

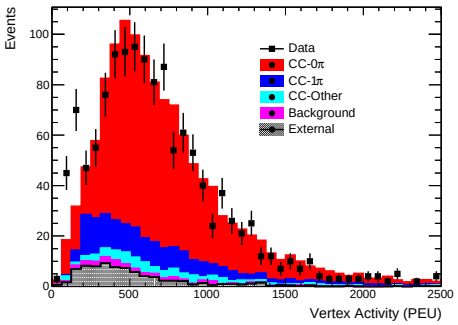

(b) Momentum = 300 - 400 MeV

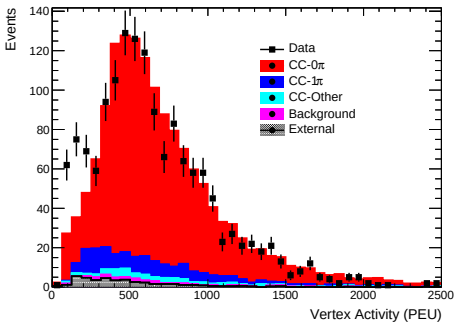

(c) Momentum = 400 - 500 MeV

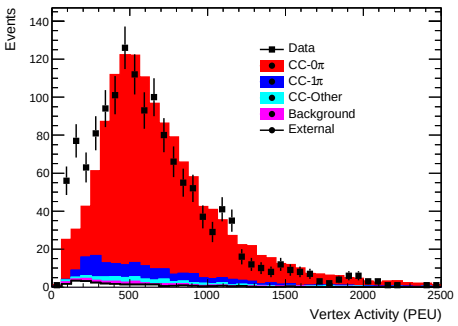

(d) Momentum = 500 - 600 MeV

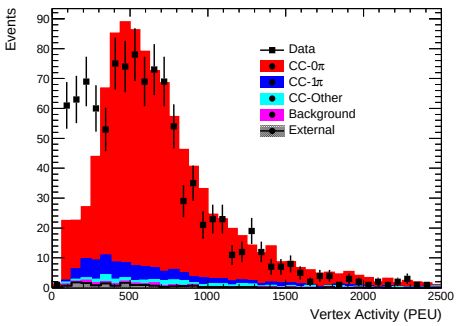

(e) Momentum = 600 - 700 MeV

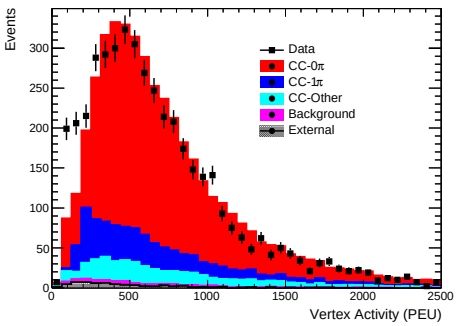

(f) Momentum $>$ 700 MeV

Figure 6.13: The VA distributions separated into different momentum regions, there is no clear sign that the momentum has an effect on the VA discrepancy.

Muon PID

The muon pull, δ_μ, is used to quantify particle identification and is defined as:

$$\delta_\mu = \frac{\frac{de}{dx}measured - \frac{de}{dx}expected}{\sigma_{\frac{dedx_{measured}}{dedx_{expected}}}} \tag{6.5}$$

The muon pull was varied for values between -0.5 and +0.5 to -2.0 and +2.0. Increasing the pull to a wider value increases the chances of being further away from the mean, so although there will be more muon events, the likelihood of incorporated particles that are not muons increases. Cutting harder on the muon PID improves the muon purity in a way that is independent of the neutrino interaction, in case the discrepancy observed is caused by pions, protons or electrons being selected as the primary track. The resulting VA distributions for these pull ranges are given by Figure 6.14 and they show that varying the muon pull had no discernible effect on the VA observed; the excess was present for all pull values.

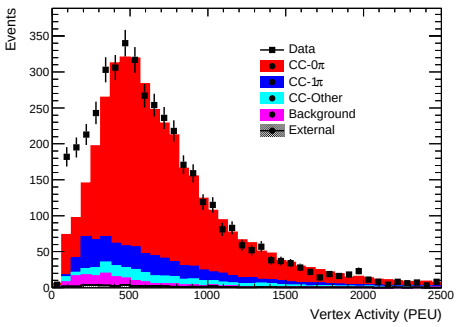

(a) Pull = -0.5 - 0.5

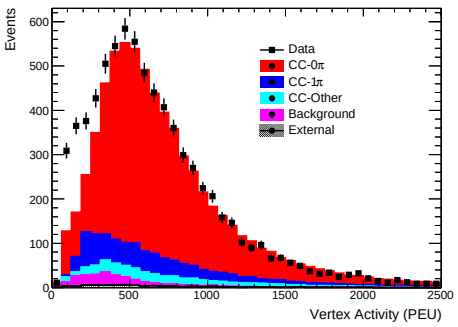

(b) Pull = -1.0 - 1.0

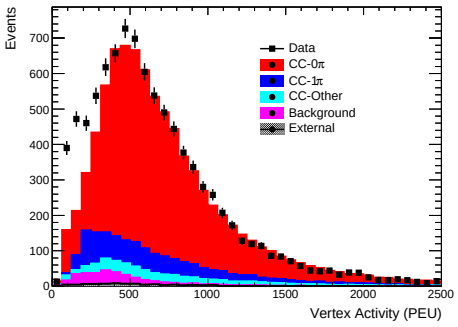

(c) Pull = -1.5 - 1.5

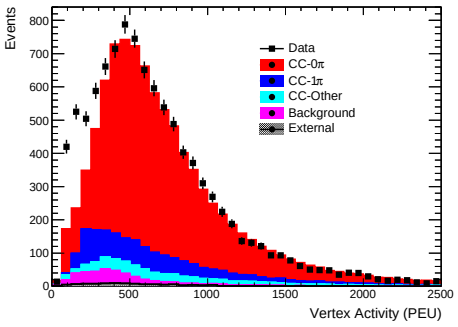

(d) Pull = -2.0 - 2.0

Figure 6.14: The VA distributions separated into different pull values, the MC used for these distributions is NEUT. Adjusting the pull seems to have no clear effect on the VA discrepancy.

6.3 GENIE MC Sample

The detector studies seem to suggest that the muon neutrino VA discrepancy is unlikely to be caused by a problem with the detector itself, so the next step was to look at a different MC generator to see if this behaved in the same way as NEUT MC. GENIE was used as the next MC sample, the details of the version of GENIE used were described in Section 6.2 and the momentum distribution of the sample is shown by Figure 6.15.

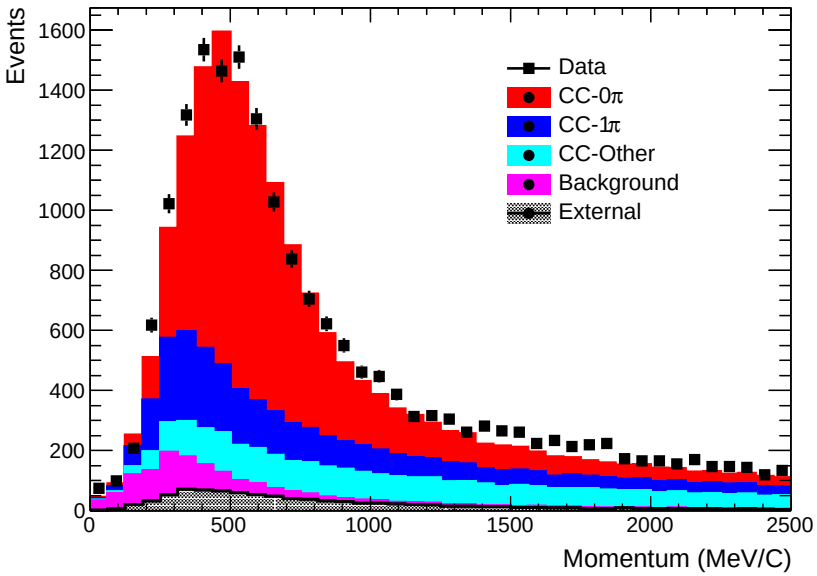

Figure 6.15: The ν_μ momentum distribution for runs 2-4 where GENIE is used as the MC sample.

Figure 6.16 gives the VA distributions of different box sizes for the GENIE MC muon neutrino sample separated into topologies, Figure 6.17 shows the VA for different GENIE interaction modes and Table 6.9 lists the interaction percentages. For GENIE, just like NEUT, a discrepancy in the data and MC is observed but the discrepancy of the two generators is quite different. At the low VA region, GENIE tries to add extra VA (unlike the low VA region of NEUT) but the amount added is too much, and the MC peak is far higher than the data. Looking at the VA of a different generator also gives us a discrepancy but the fact that GENIE is quite different to NEUT leads to the assumption that the discrepancy is due to poor modelling of low energy particles in the generators.

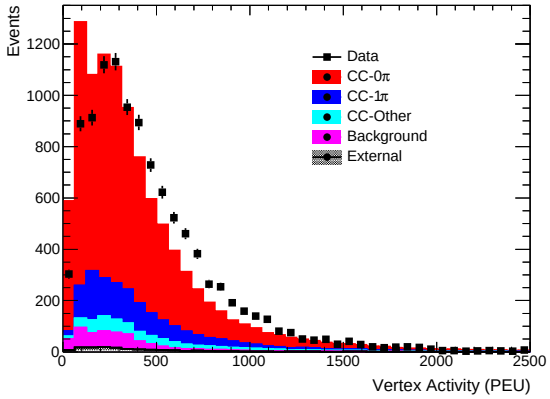

(a)

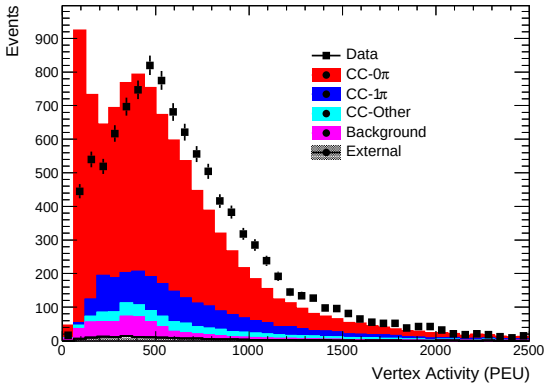

(b)

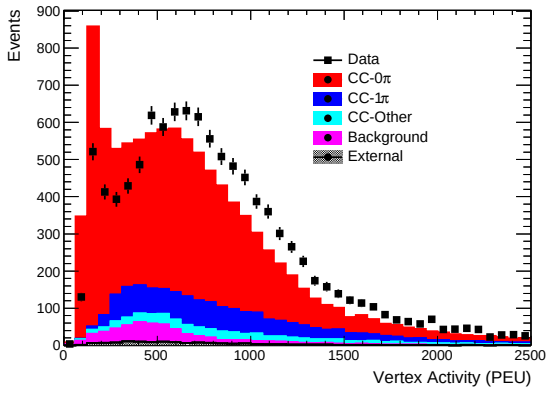

(c)

Figure 6.16: Distribution of the vertex activity for the ν_μ sample. The MC used is GENIE, and each vertex region is shown: (a) 3x3x3 (b) 5x5x5 (c) 7x7x7. There is a disagreement in data and MC observed.

Interaction mode	GENIE (%)
QEL	71.84
COH	0.44
RES	22.93
DIS	0.35
BG	4.45
2p2h	N/A

Table 6.9: The breakdown in percentage of interaction modes for GENIE MC.

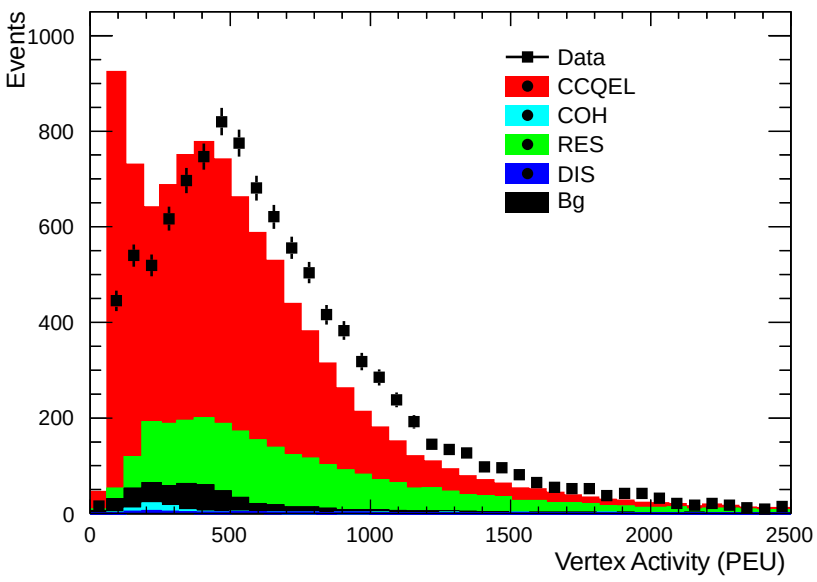

Figure 6.17: The 5x5x5 vertex activity distribution of the ν_μ sample using GENIE MC, separated by interaction modes.

6.3.1 Discrepancy Conclusions

The VA discrepancy in data and MC was observed in the muon neutrino sample for both NEUT and GENIE MC, and the way the discrepancy behaved in both of these samples was very different. This effect is unexpected as one would presume that the two generators would behave in a similar manner, however neither of the generators agree with the data and the way they differ with data is very different.

Whilst the studies were ongoing, a bug in the NEUT 6B production (version 5.3.2) was discovered that affected the proton FSI as shown by Figure 6.18, where a threshold has been imposed at around 200 MeV/c. As low momentum protons contribute to the VA and the bug occured at the low proton momentum range, it was suggested that maybe this is the reason there is a difference in VA for data and MC. An updated version of NEUT without any truth information (production 6D, v5.3.2.2) was available during the analysis and a shape-only comparison plot of NEUT productions 6B and 6D as well as GENIE and data was produced, as shown by Figure 6.19. This figure shows that although the bug in NEUT 6B was fixed, there is still a discrepancy in the updated NEUT version and data, which means that further studies into generator models are required to improve low momentum simulation. This analysis only focused on the GENIE and NEUT MC generators, but other ones are available such as NuWro [117] and Giessen Boltzmann–Uehling–Uhlenbeck (GIBUU) [118] which may suggest alternative VA information.

The studies performed ultimately suggest that the reasons for the data and MC disagreement are unlikely due to the detector but are instead due to a lack of understanding of nuclear processes in generators. The way in which NEUT and GENIE simulate low momentum proton production vary and more work in developing the low energy theory of generators will greatly improve the understanding of multinucleon effects.

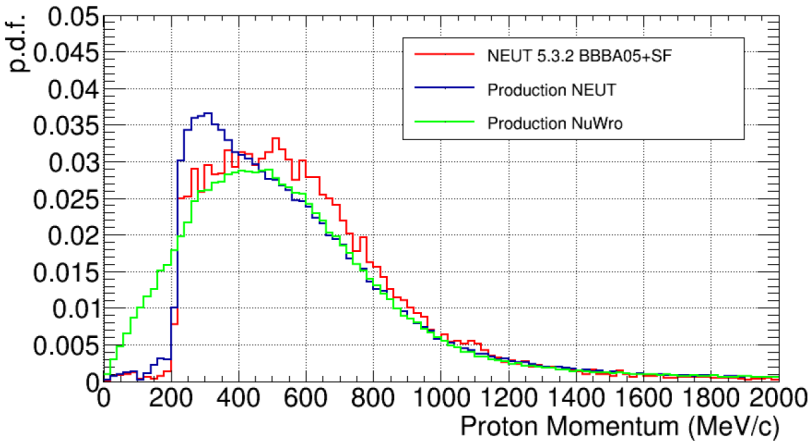

Figure 6.18: Plot showing the proton momentum for different MC samples. It is clear to see that there is a bug in proton momentum for the NEUT 6B production [119].

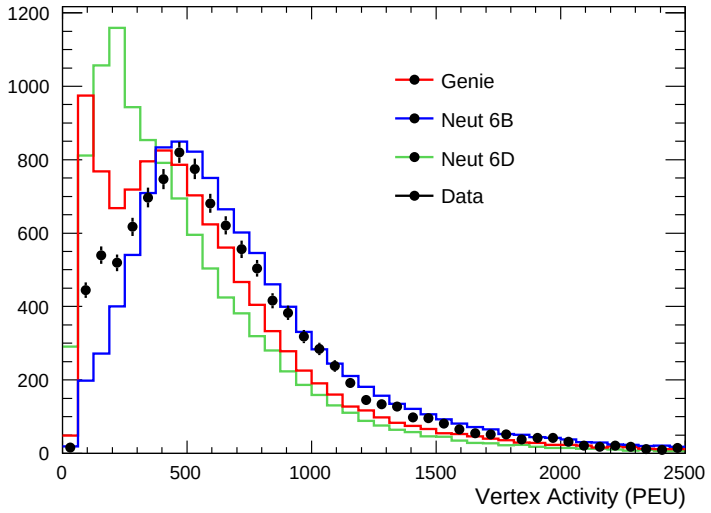

Figure 6.19: A comparison of the vertex activity for the NEUT 6B (blue), NEUT 6D (green), GENIE (red) and data (black) samples. There is a shape difference in each sample and the data does not agree with any of the MC at low vertex activity regions.

6.4 Detector Systematics

In order to investigate the detector bias on the VA, the data and MC of two control samples were compared. The VA of the FGD energy scale can be measured in two ways, either by the energy deposition of MIPs as they traverse through the FGD or by calorimetry of a stopping proton with a known momentum depositing its energy inside a box centered on a stopping point. This section discusses the control samples in further detail and provides systematic uncertainties for each sample.

The data used for the systematics came from runs 2-4 using Production 6L, and the MC used was NEUT Production 6B which equates to v5.3.2. Both samples used Highland2 v2r13 for FGD1 only, and all the plots in this section are POT normalised unless specified otherwise.

6.4.1 Stopping Protons

Protons are a good way to measure the FGD energy scale because if their momentum is known, it is possible to determine their energy deposition after they have stopped in a region. For the stopping proton control sample, good event quality is required, then the most energetic (Highest Momentum (HM) track) in a TPC with at least 18 TPC hits and either positive or negative charge is selected. Table 6.10 outlines the number of entries and POT values used for data and MC of the stopping proton sample and Table 6.11 lists the cuts that were used in order to select the stopping protons, the protons were required to pass the first 5 layers of FGD1, and then stop and deposit all of their energy in FGD1.

	Data	MC
no. of entries	326324	2082070
POT (10^{21})	0.580	4.935
DATA/MC POT ratio	0.118	

Table 6.10: The no. of entries and POT values for the stopping proton sample.

Figures 6.20 and 6.21 show the momentum distribution and dE/dx of the stopping proton sample respectively.

In order to deduce the systematic uncertainties for the stopping protons, a landau fit to data and MC of the dE/dx distribution was performed. It is possible to use the dE/dx value as an alternative definition of VA (the amount of charge (or energy deposited - dE) in a given region - dx). By measuring the difference in the means of data and MC, one can measure the systematic uncertainty due to mismodelling of VA, i.e. the

energy scale and then the differences in the width of data and MC gives a systematic due to resolution. Table 6.12 provides the values for the mean and sigma for both data and MC obtained from a landau fit, where the difference in data and MC mean is (0.60 $\pm$ 0.34) % and in σ is (1.12 $\pm$ 0.02) %.

Number	Name
0	Event quality
1	Postive candidate track
2	Candidate ends in FGD1 FV
3	No TPC2 track
4	No FGD2 tracks
5	No ECal tracks
6	Proton PID
7	HM track starts in PØD FV
8	NO other PØD tracks

Table 6.11: Cuts used for the stopping proton selection.

Stopping Proton	dE/dx
$\mu_{MC} \pm \delta\mu_{MC}$(PEU/mm)	0.653 $\pm$ 0.003
$\mu_{data} \pm \delta\mu_{data}$ (PEU/mm)	0.649 $\pm$ 0.003
$\sigma_{MC} \pm \delta\sigma_{MC}$(PEU/mm)	0.127 $\pm$ 0.002
$\sigma_{data} \pm \delta\sigma_{data}$ (PEU/mm)	0.126 $\pm$ 0.002

Table 6.12: Values for the mean and sigma of the stopping proton sample obtained from a landau fit.

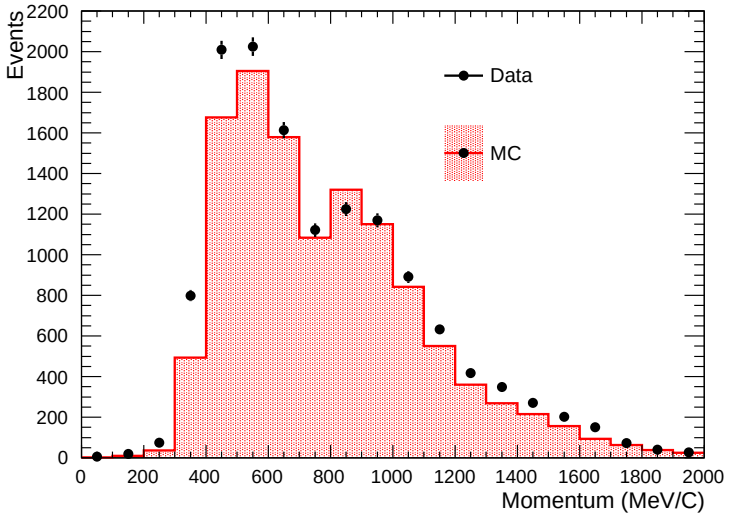

Figure 6.20: Momentum distribution of the stopping proton sample for data (black points) and NEUT MC (red).

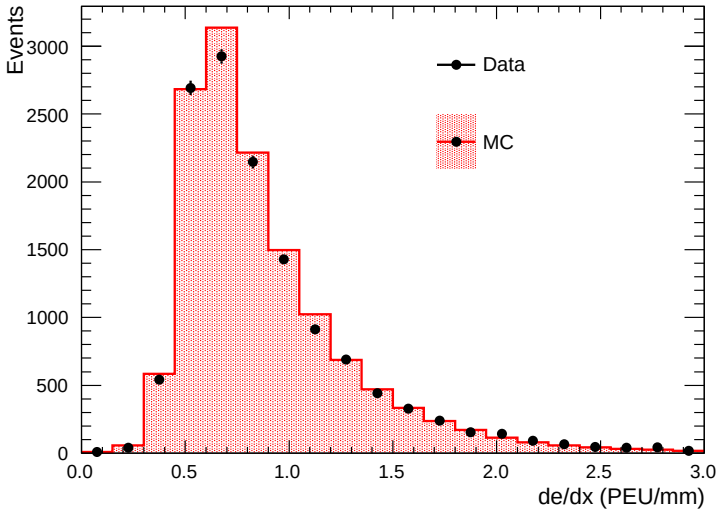

Figure 6.21: Distribution of dE/dx for the stopping proton sample for data (black points) and NEUT MC (red).

6.4.2 Throughgoing Muons

The throughgoing muon control sample is used to measure the FGD1 energy scale and cosmic or sand muons[5] are used for the muon sample as they behave like MIPs. Table 6.13 provides a list of the number of entries used for the throughgoing muon sample; there is no POT information as the muons came from background events and not from the beam. The throughgoing muon sample assumes good data quality, at least one reconstructed track in a TPC, and then the most energetic global track is selected. The selection requires that the muon must pass through all 3 TPCS as shown by Figure 6.22 and Table 6.14 provides a list of the cuts used in this selection.

	Data	MC
no. of entries	14792819	116476088

Table 6.13: The no. of entries for data and MC, for the throughgoing muon sample.

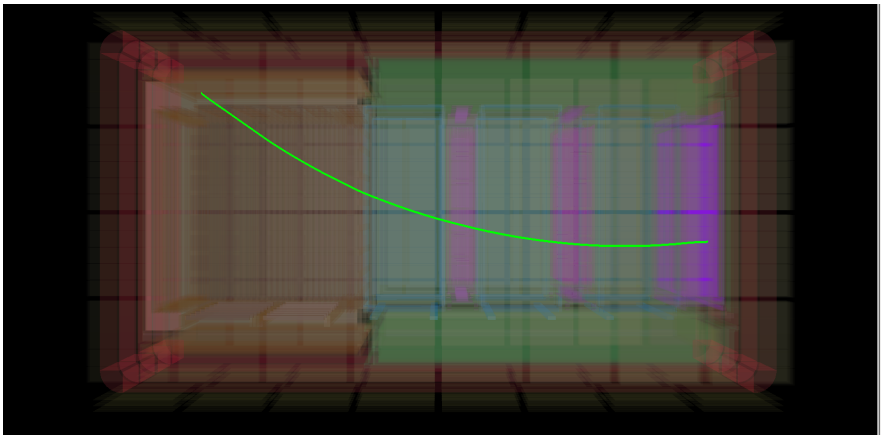

Figure 6.22: ND280 event display showing an example of a event used in the throughgoing muon sample. The muon (green) is seen traversing the entire ND280 detector.

Number	Name
0	Data quality
1	Negative candidate track
2	POD-TPC2 track
3	TPC2-DsECal track
4	TPC1-TPC3 track
5	Passes through all 3 TPCs
6	Muon PID

Table 6.14: Cuts used for the throughgoing muon selection.

Figures 6.23 and 6.24 show the momentum distribution and energy distribution of the

[5]Sand muons are muons that are produced in the external material that surrounds the ND280 detector.

throughgoing muon sample respectively.

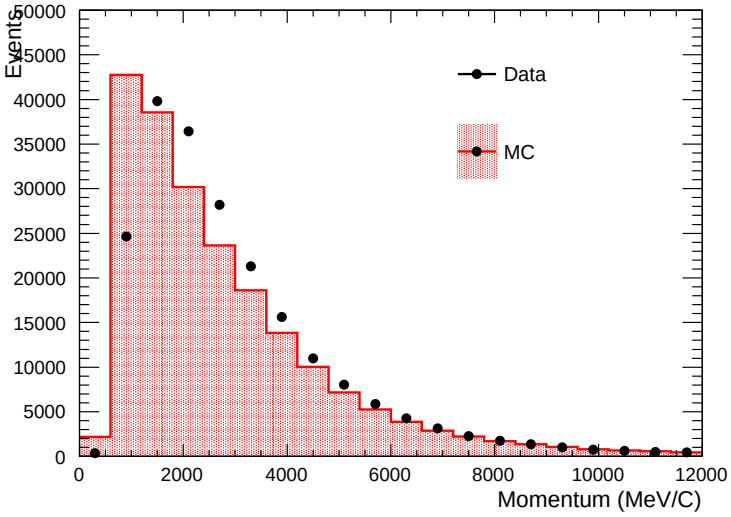

Figure 6.23: Momentum distribution of the throughgoing muon sample, the black points represent data and NEUT MC is shown in red.

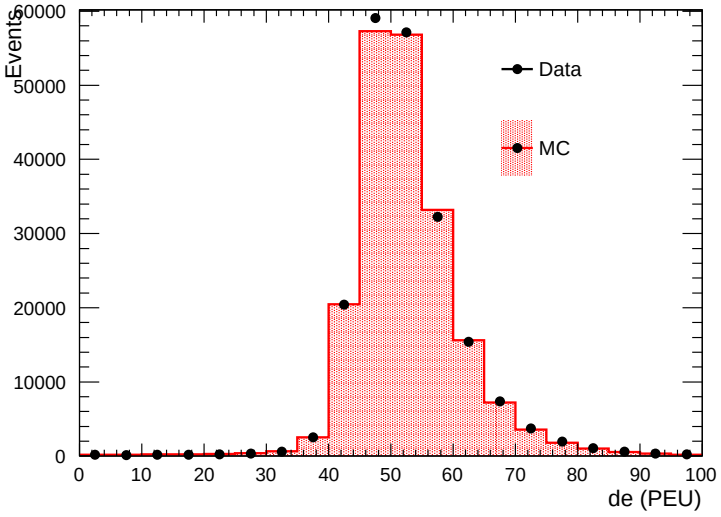

Figure 6.24: Energy distribution recorded in FGD1 using the throughgoing muons as they pass through the detector.

There is a discrepancy observed in data and MC for the momentum distribution, however this could be caused by sand muons being excluded from the MC sample which may mean that the excess is due to this alone. Secondly, the momentum distribution is normalised prior to the Beam And ND280 Flux extrapolation task Force (BANFF) fit [6] which means that the flux and cross section uncertainty itself is larger and does not benefit from the rescaling that would go into the oscillation analysis from the ND280 fit.

A similar procedure was applied to the throughgoing muons; a landau fit to data and MC of the energy distribution. This gives a difference in the means of data and MC of (0.27 $\pm$ 0.01) %, and a difference in σ of (3.87 $\pm$ 0.01) %; Table 6.15 lists the mean and sigma values for the throughgoing muon sample.

Throughgoing Muon	dE/dx
$\mu_{MC} \pm \delta\mu_{MC}$(PEU/mm)	48.45 $\pm$ 0.02
$\mu_{data} \pm \delta\mu_{data}$ (PEU/mm)	48.31 $\pm$ 0.02
$\sigma_{MC} \pm \delta\sigma_{MC}$(PEU/mm)	3.07 $\pm$ 0.01
$\sigma_{data} \pm \delta\sigma_{data}$ (PEU/mm)	2.95 $\pm$ 0.01

Table 6.15: Values for the mean and sigma of the throughgoing muon sample obtained from a landau fit.

Table 6.16 outlines the difference in the means and σs between data and MC for the stopping proton and the throughgoing muon sample. These results will be used to estimate the overall systematic uncertainty in Section 8.2.

	Stopping proton (%)	Throughgoing Muon (%)
Difference in $\bar{x}$	0.60	0.27
Difference in σ	1.12	3.87

Table 6.16: The difference in the mean and sigma values, for data and MC, for the stopping proton and throughgoing muon sample.

[6] The fit to the ND280 data to further constrain the flux and cross section uncertainties and provide them to the oscillation analyses is known as the BANFF fit [120].

Chapter 7

Response Functions

A response function is a way in which predictions can be made regarding the reconstruction of the detector, such as momentum or energy values, including all unknown effects. For the VA analysis, response functions were constructed to predict the VA for a given neutrino interaction. These were developed using a set of MC particles to produce VA distributions that were then fitted appropriately, (e.g. using a gaussian, landau-gaussian etc) in order to get a prediction for the VA for different particle types and momentum ranges.

The benefit of using a response function is that it allows VA predictions of interactions based on the MC which removes the need to undergo full GEANT reconstruction of any MC. It is also possible to investigate what will happen if particles are introduced in the final state such as extra low energy protons in order to reasonably assess the effect of different models on the nuclear processes that produce VA. A response function is necessary to predict the VA distribution from ND280 as low energy protons cannot be reconstructed so, instead particle guns[1] are used to simulate the response of particles in the detector.

This chapter will discuss how the response functions for different particles, such as electrons, muons and protons, were constructed, starting with simulations using MC particle guns, then moving onto fitting these different distributions, and finally to producing the response functions themselves. How this information can be used in order to understand the VA discrepancy observed in the muon sample, will also be discussed in this chapter.

[1] A particle gun is a way in which particles of a given type can be created to "shoot" in a given direction with a given kinetic energy or momentum. GEANT4 provides functions in which the user can adjust particle kinematics to reproduce events within the detector.

7.1 Monte Carlo

In order to investigate the behaviour of particles in the ND280 detector, a number of different particle gun MCs were run and distributions of the VA were produced. As the main focus of this analysis are muons and protons, these distributions will be described in further detail, however a brief discussion of how the electron particle guns behave has been included in Appendix 9.3 for completeness.

The VA is contingent upon a reconstructed track being present in the event, and the reconstruction of the VA comes from the vertex of that reconstructed track. After simulating a muon using a particle gun MC, one can deduce the muon's VA contribution straightforwardly; the track can be reconstructed and the VA can be calculated. Problems start to occur when the VA of an additional track is considered, as the VA is defined with respect to the reconstructed track, which will essentially be the reconstructed muon. In order to combat this issue, MCs of muons in addition to the particle to be investigated (in this case, protons) can be run and the VA contribution can be investigated. In other words, because it is possible to understand a single muon's contribution to the VA, one can then run a low energy proton from the same point as the muon and by fitting out the muon contribution, it is possible to understand the proton's VA contribution.

The following sections will show how it is possible to understand the VA behaviour of low energy protons using MC simulations and response functions.

7.1.1 Muon and Proton Particle Gun Studies

The particles simulated by the particle guns were centered in FGD1 at a position of 0.0 x 0.0 x 30.0 cm, and the vertex size was 2cm x 2cm x 2cm. These dimensions were used to ensure that the different VA box sizes encompassed the FGD FV and there were no edge-of-detector effects caused from the final few bars of FGD1 or the TPC.

The muons simulated for the particle gun studies were run with a kinetic energy of 500 MeV, isotropically and at an opening angle of 45°. The protons were run with a range of kinetic energies between 10 MeV and 200 MeV, the particles were isotropic and their opening angle was set at 360°. Figure 7.1 shows an event display of a single 500 MeV muon, in green, and a single 50 MeV proton, in blue; the proton, having a low momentum, is seen to deposit all its energy in FGD1 whereas the muon, with a greater momentum, is seen to reach the downstream ECal.

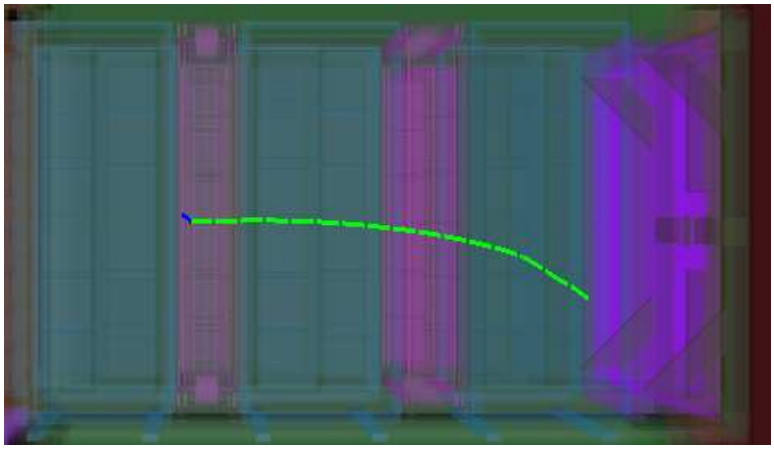

Figure 7.1: ND280 event display showing a single 500 MeV muon (green) and a single 50 MeV proton (blue), simulated from FGD1.

Figure 7.2 shows the VA distribution of muons with a kinetic energy between 100-800 MeV for different VA box sizes. These distributions show that although there is a slight dependency on the mean muon momentum and VA[2], when considering the VA contribution and uncertainty, the effect is not significant enough to worry about the value of muon momentum used. Therefore, only using a 500 MeV muon, for this analysis, is completely acceptable.

The next set of particle guns produced were muons with protons of various energies, and Figures 7.3 show the VA distribution for different vertex box regions for these sets of particles. It can be seen that the addition of a proton shifts the mean of the VA to higher values gradually with increasing KE up until a certain value, where the mean VA shifts to lower values. This occurs because the proton is now escaping the VA region, and depositing its energy outside of the VA region, thus the overall VA in the box is lowered. Figure 7.3 shows that this occurs at a different value for each VA region. For added clarity, the vertex activity for single muons and single muon plus single proton has in addition, been represented using a log y scale, as can be seen by Figure 7.4, and Table 7.1 shows a table of mean values.

[2]In Figure 7.2, the 5x5x5 muon momentum distribution gives a mean VA value for the 500 MeV muon of roughly 90-100 PEU, and the mean VA for the 200 MeV muon is around 110 PEU, which corresponds to a difference of 10-20 PEU. The VA value for a typical event (see Figure 7.6) is approximately 600-800 MeV, therefore the momentum dependence can be considered to be an insignificant effect.

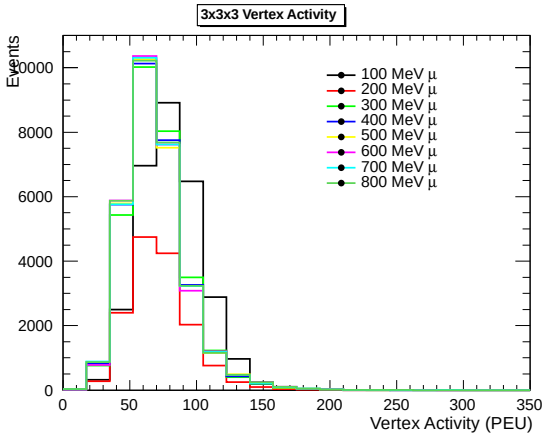

(a)

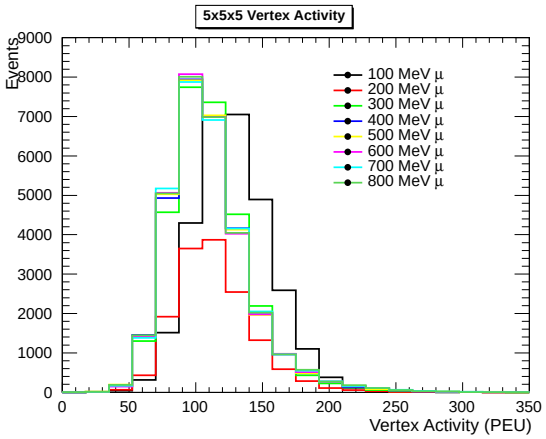

(b)

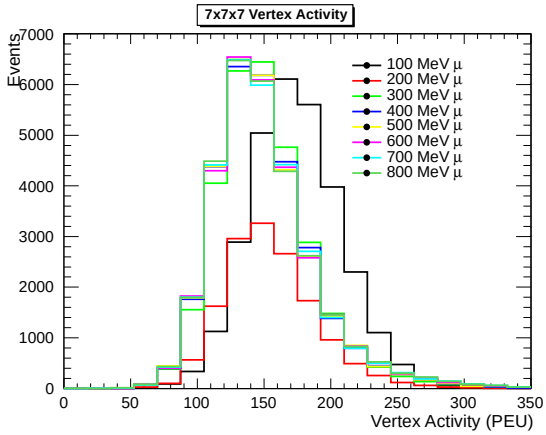

(c)

Figure 7.2: Distributions of vertex activity for the single 500 MeV muon at: (a) 3x3x3 (b) 5x5x5 (c) 7x7x7 vertex region.

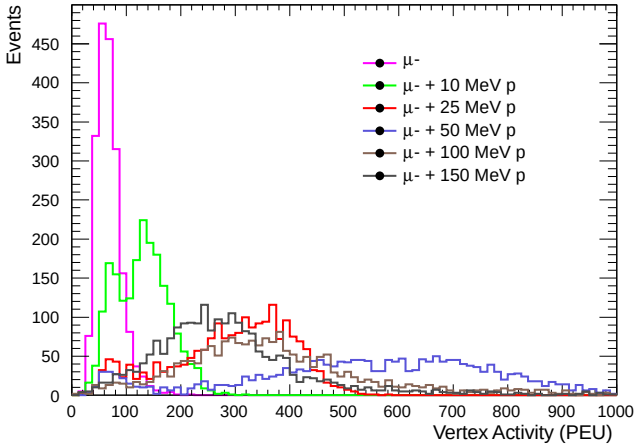

(a)

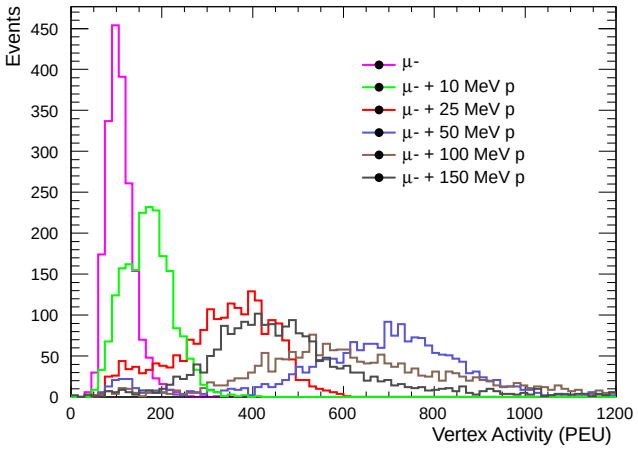

(b)

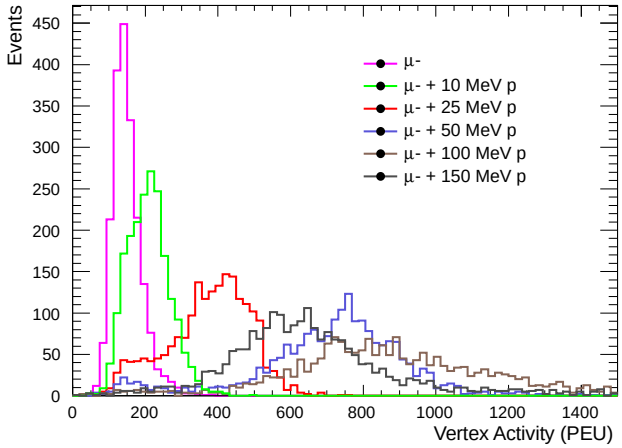

(c)

Figure 7.3: Distribution of vertex activity for the single 500 MeV muon and single 500 MeV muon + single (10 - 150 MeV) protons, for the vertex regions: (a) 3x3x3 (b) 5x5x5 (c) 7x7x7.

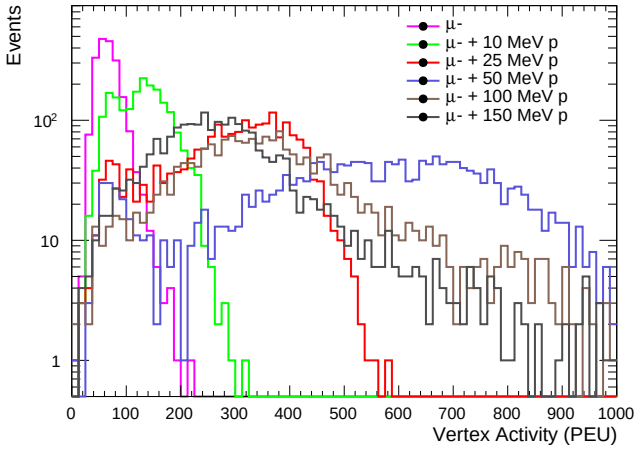

(a)

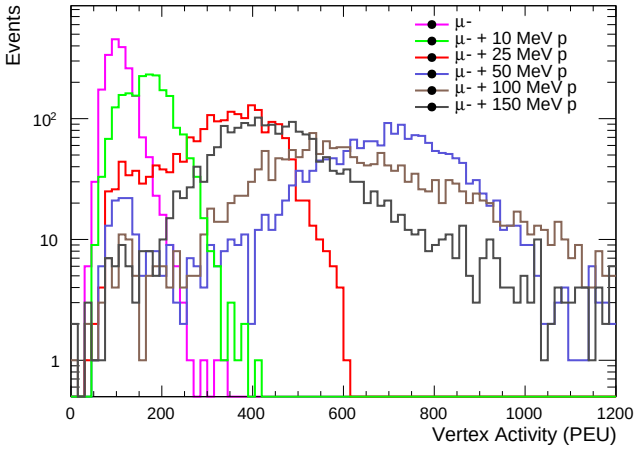

(b)

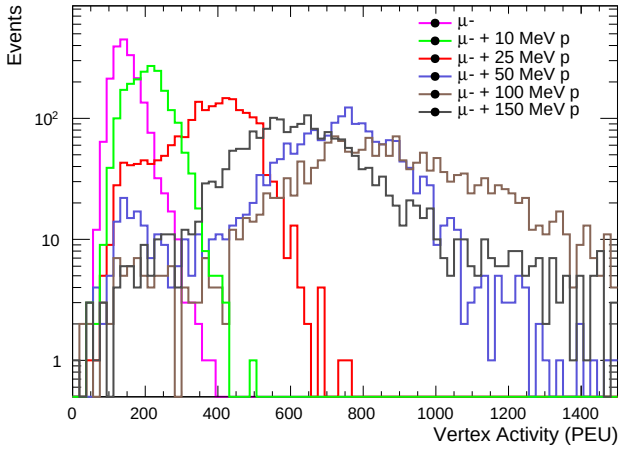

(c)

Figure 7.4: Distribution of vertex activity for the single 500 MeV muon and single 500 MeV muon + single (10 - 150 MeV) protons, using a loy y scale for the vertex regions: (a) 3x3x3 (b) 5x5x5 (c) 7x7x7.

	Mean Value (PEU)		
	3x3x3	5x5x5	7x7x7
Single μ	68.36	109.45	150.31
Single μ + 10 MeV p	291.73	334.85	374.57
Single μ + 25 MeV p	537.32	657.32	705.17
Single μ + 50 MeV p	370.01	624.21	858.85
Single μ + 100 MeV p	128.92	169.74	209.51
Single μ + 150 MeV p	288.63	479.94	653.76

Table 7.1: A table of means for each vertex activity value.

7.2 Building Response Functions

Response functions can be built from the particle gun plots by fitting the single muon only and single muon and single proton distributions and using the relevant fit values to construct a response function. As well as this, the single muon distributions can be fitted out from the single muon and proton distributions in order to create a single proton only distribution. This method is necessary as single proton distributions are not available as the momentum of the proton is too low for reconstruction in the ND280 software. This section will describe the methods used to build a response function, starting with Gaussian fits and eventually moving onto a combined Landau-Gaussian fit.

7.2.1 Gaussian Fits

As an initial, first order assumption the single muon, and single muon and proton distributions, were fitted with a Gaussian in order to extract the relevant information to develop the response functions.

The probability density function of a Gaussian fit is defined by

$$p(x;\mu,\sigma) = \frac{1}{\sqrt{2\pi}\sigma} e^{-} \frac{(x-\mu^2)}{2\sigma^2} \tag{7.1}$$

where μ is the mean, and σ is the width.

Figure 7.5 (a) shows the single muon sample fitted with a Gaussian and Figure 7.5 (b) shows the single muon and 100 MeV proton fitted with a Gaussian. It is clear to see that there are problems with the Gaussian fit to both of these samples and the fit does not match the data accurately. The Gaussian fit to the single muon and single 100 MeV proton is significantly worse than the single muon only distribution, the addition of low energy protons means that the distribution is no longer modelled well by the Gaussian.

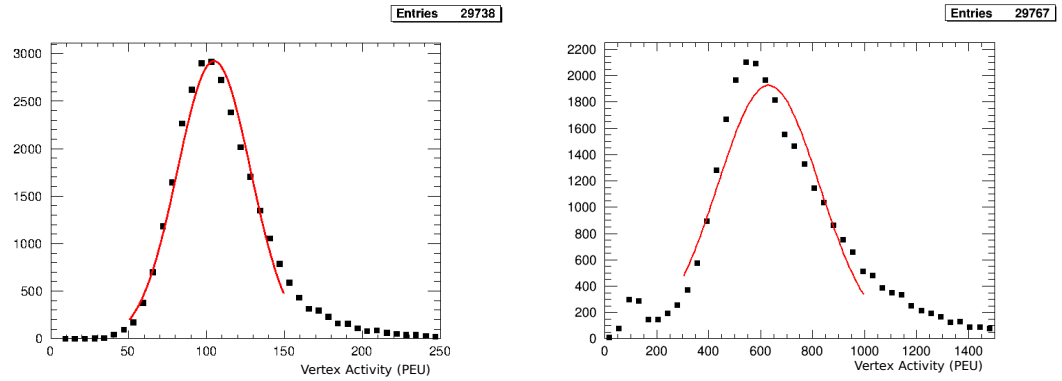

(a) Single 500 MeV muon. **(b)** Single muon and 100 MeV proton.

Figure 7.5: Single 500 MeV muon sample, as well as the single 500 MeV muon and 100 MeV proton, both fitted with Gaussian (red). It is clear that the Gaussian does not provide a good fit to these samples.

7.2.2 Landau-Gaussian Fits

As the Gaussian fits presented in the previous section do not fit the data accurately, the behaviour of Landau-Gaussian fits were investigated next. Landau fits are often used to describe the statistical fluctuations in energy loss of a charged particle passing through a thin layer of material as described by Landau [121]. The Landau distribution behaves similarly to a normal distribution but with a long upper tail caused by highly ionising electrons. The single muon distributions are fairly well modelled by a Gaussian but, the addition of low energy protons with energies far below the MIP energy mean that the Landau tail disappears and instead behaves more like a Gaussian distribution. In addition, the detector resolution of ND280 provides an additional resolution convolution which can be mapped better using a Gaussian, hence why a Landau-Gaussian convolution is considered more suitable for these fits.

The Landau fit can be described as

$$\phi^{'}\lambda = -\frac{1}{\pi}\int_0^\infty e^{-\lambda u}u^{1-u}\,sin\pi\,u\,du \tag{7.2}$$

and the resulting Landau-Gaussian function is a convoluted sum of Equation 7.1 and Equation 7.2.

Figure 7.6 shows the single 500 MeV μ, single 500 MeV μ + single 50 MeV proton, and finally single 500 MeV μ + single 100 MeV proton distributions, fitted with a Landau-Gaussian for the 5x5x5 vertex region. It is clear to see from these distributions that, using a Landau-Gaussian convolution provides a more successful fit than using a Gaussian alone.

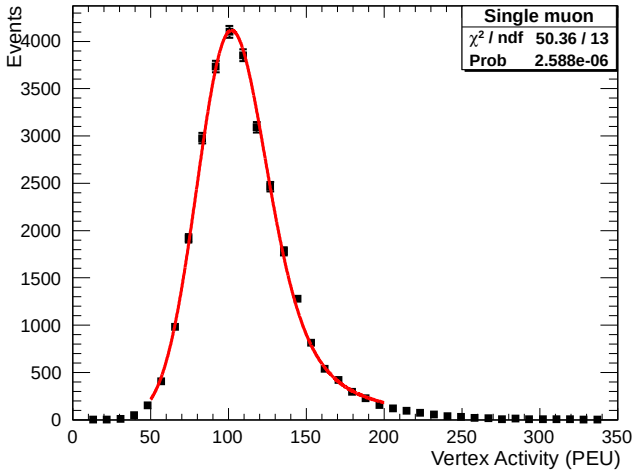

(a)

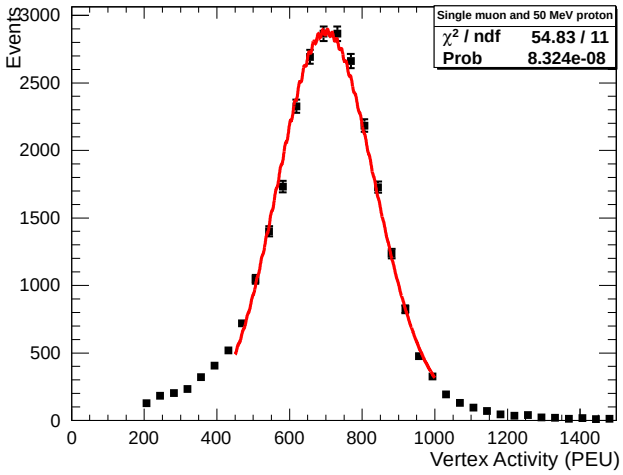

(b)

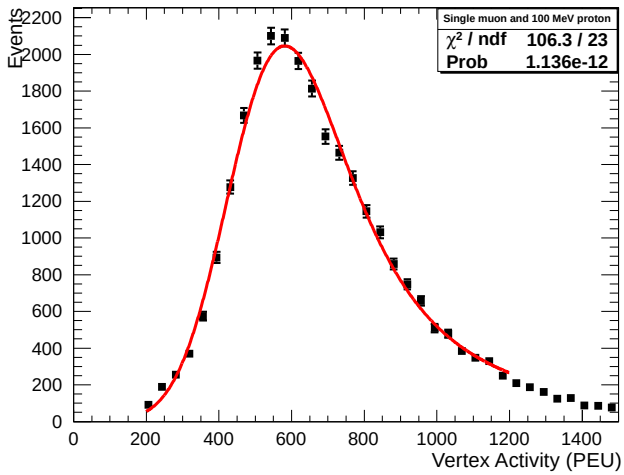

(c)

Figure 7.6: Distributions of the vertex activity, for the 5x5x5 vertex region, fitted with a Landau-Gaussian for: (a) single 500 MeV muon (b) single 500 MeV muon and a single 100 MeV proton (c) single 500 MeV muon and a single 50 MeV proton.

Single Muon MC

Using the Landau-Gaussian fit values from Figure 7.6, it is possible to recreate the single 500 MeV μ only histograms, by using a random number generator. Figure 7.7 shows a comparison of the new single μ distributions compared to the previous single 500 MeV μ MC (Figure 7.2), for different vertex regions.

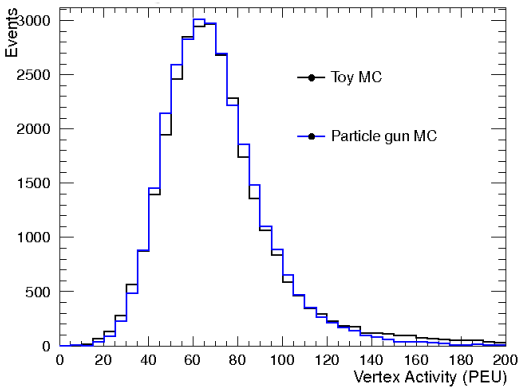

(a)

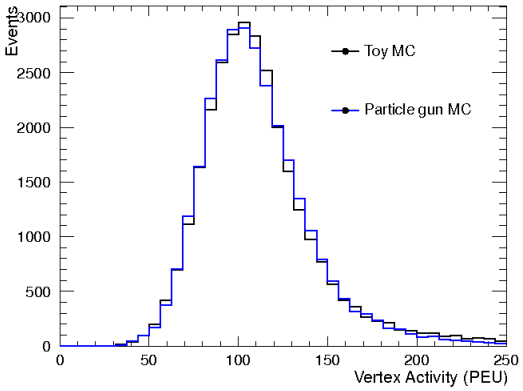

(b)

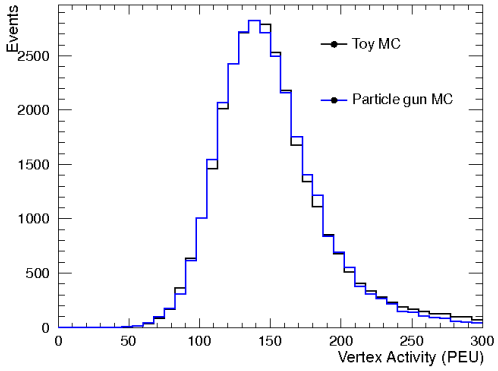

(c)

Figure 7.7: Comparisons of the original single μ MC (Particle gun MC) and the new μ MC (Toy MC) built using fit values from the original μ MC, for: (a) 3x3x3 (b) 5x5x5 (c) 7x7x7.

Single Muon with Single Proton Distribution

The similarities between the original μ MC and new single μ samples show that producing new distributions from fit values accurately gives us distributions matching the original MC. Therefore the next stage was to compare the original single 500 MeV μ + single proton particle gun MC to new particle gun distributions. The original distributions were fitted with a Landau-Gaussian and the fit parameters obtained were used to draw new distributions using a random number generator, in the same way as for muons only. Figure 7.8 shows the comparison between the original 500 MeV μ + 100 MeV proton (blue) and the new constructed 500 MeV μ + 100 MeV proton distribution (black) for each vertex region, and the χ^2 values for each distribution is given in Table 7.2. The two distributions behave in a similar manner, the tail is well modelled and the peak of both distributions is centered around the same value.

As it is possible to construct new single μ and single proton distributions that are similar to the original MC distributions, the next stage involved extending the single muon + single proton distributions for protons with an energy range between 10-200 MeV, at 10 MeV increments. This energy range was chosen by considering the distributions in Figure 7.3, and ensuring the energy at which the mean VA was decreasing for all vertex box sizes was encompassed in the full energy range. The same method to produce new distributions, as described previously, was repeated to construct new single muon + single proton distributions.

The full proton KE energy MC ranging from 10-200 MeV was used to produce a response function which is shown in Figure 7.9, along with the response function for the original MC. The error bars in the response functions represent the spread of the Landau-Gaussian that the distribution was drawn from.

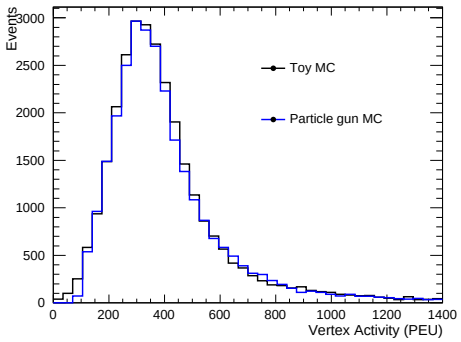

(a)

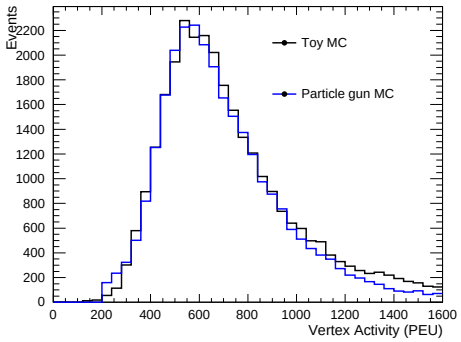

(b)

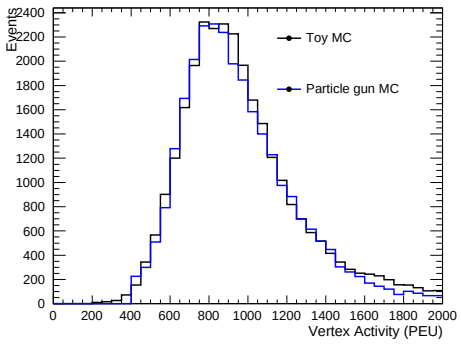

(c)

Figure 7.8: Comparison between the new MC (Toy MC) and particle gun MC (original MC) for a single 500 MeV muon with a single 100 MeV proton for (a) 3x3x3 (b) 5x5x5 and (c) 7x7x7. The two distributions behave in a similar manner, the mean is centered around the same value.

Vertex region	χ^2	χ^2/NDF
3x3x3	101.23	2.60
5x5x5	65.74	1.83
7x7x7	42.02	1.24

Table 7.2: A table showing the χ^2 and χ^2/NDF values for each of the vertex regions for the new MC and particle gun MC for a single 500 MeV μ with a single 100 MeV proton.

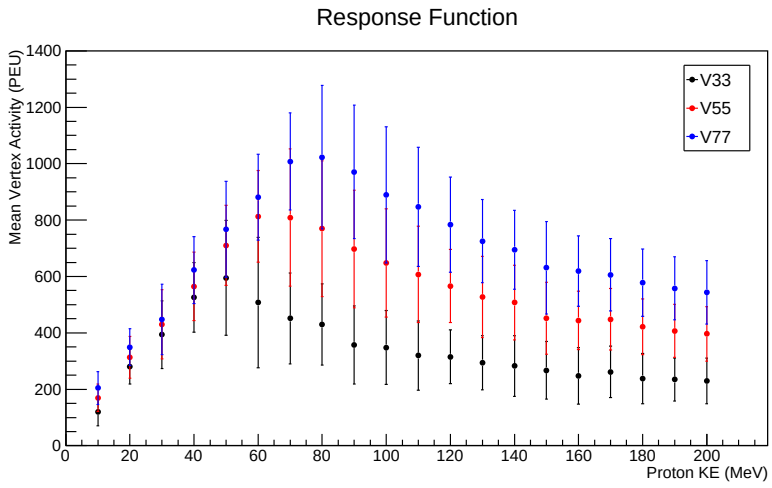

(a)

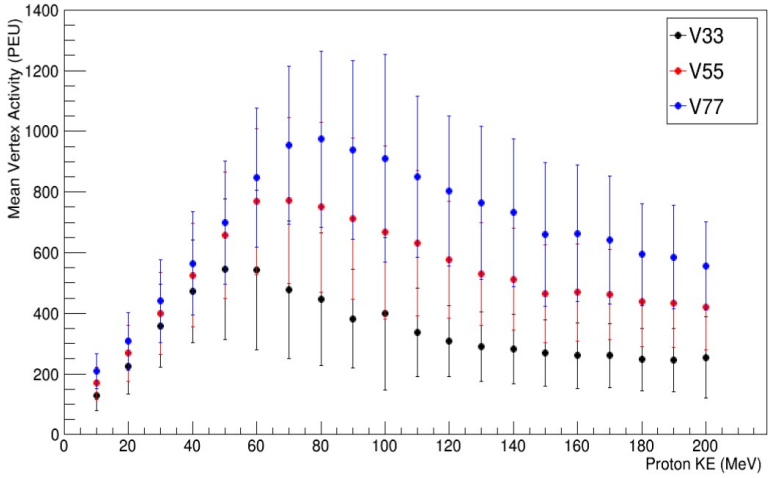

(b)

Figure 7.9: Response Functions for the single 500 MeV muon and single (10 - 200 MeV) proton distributions for: (a) the new MC (b) the original particle gun MC. The error bars represent the width of the Landau-Gaussian.

Single Proton Only Distribution

Now that it is possible to construct single muon and single proton distributions, the next stage involved constructing single proton only distributions. As mentioned before, this method is necessary as ND280 does not allow the reconstruction of low energy protons, therefore low energy single proton MC cannot be simulated but instead, they can be constructed from the single muon distributions being fitted out from the single muon plus single proton distribution.

The single proton toy MC can be built by using the fit parameters of the single 500 MeV muon (Figure 7.6 (a)) and the fit values from the single 500 MeV muon + single (10 - 200 MeV) proton and fitting the single muon contribution out, in order to construct a single proton only distribution. In effect, the single proton distributions are built by subtracting values randomly drawn from the single muon fit, from random values drawn from the random values drawn from the muon plus proton distributions. Figure 7.10 shows the new single proton only distributions for protons (including the 500 MeV single muon), for each vertex region. The distributions behave similarly to the distributions shown in Figure 7.3, and as observed previously, the VA values increase as the vertex box region increases, up until a point, where the VA values fall as the particles escape the vertex region.

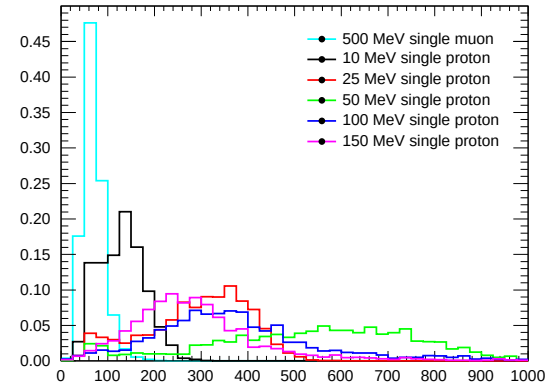

(a)

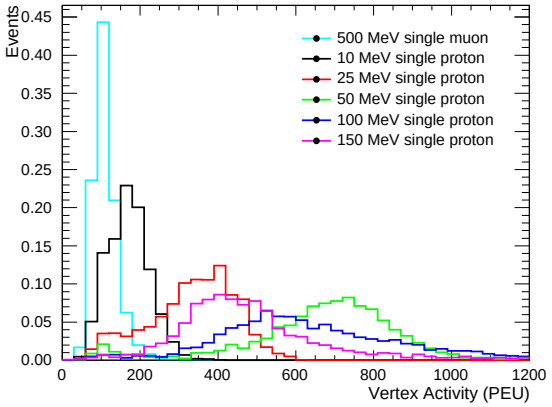

(b)

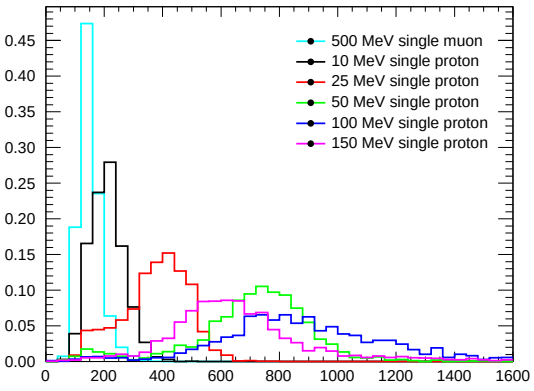

(c)

Figure 7.10: Vertex activity distribution for the 500 MeV single muon (blue), and the single protons (10 - 150 MeV) built using the Landau-Gaussian fit values for vertex regions: (a) 3x3x3 (b) 5x5x5 (c) 7x7x7.

Appendix 9.4 shows the single proton distributions, for the full proton energy range in increments of 10 MeV, starting from 10 MeV through to 200 MeV. Using the full proton distribution it is possible to create a response function for single protons only, as shown by Figure 7.11, where the error bars correspond to the spread of the Landau-Gaussian fit.

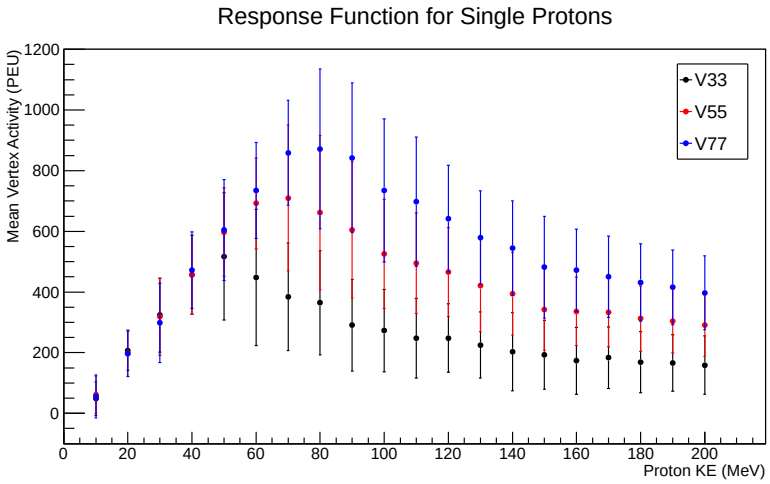

Figure 7.11: Response functions for single proton only distributions, created by fitting out the single 500 MeV muon from the single 500 MeV muon and single (10 - 200 MeV) proton MC. The error bars represent the spread of the Landau-Gaussian.

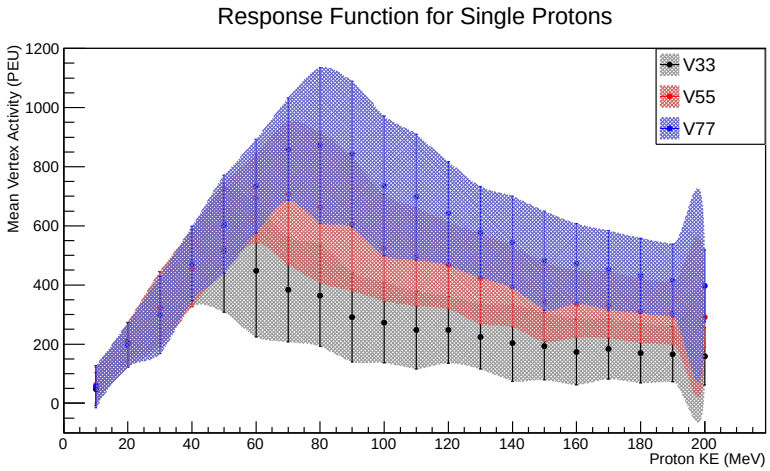

Figure 7.12: Response functions for single proton only distributions, similar to the plot above, but with shaded bars instead

Muon and Double Proton Distribution

As an additional study, distributions of single muon and double protons were produced and investigated. A single 500 MeV muon was simulated, along with two protons with a KE ranging from 5 MeV to 75 MeV, in order to compare to the single muon and single proton distributions described in the previous section. Figures 7.13 show the VA distributions for the single 500 MeV muon and double protons for each vertex region.

Figure 7.14 shows the distributions of the single 500 MeV muon and single proton compared to the single 500 MeV muon and double protons, where the overall energy of the protons in each plot is the same, for the 5x5x5 vertex region. There may be an assumption that going from 1 proton to 2 protons is straightforward and will only require a factorising effect, but as Figure 7.14 clearly shows, single protons do not behave in the same way as the double protons, especially towards higher proton energies. The distributions in Figures 7.14 (a) and (b) have a similar shape but the means are not centered around the same value. At higher proton energies, the distributions behave very differently. For example, whilst it may be assumed that one 100 MeV proton would behave the same as two 50 MeV protons, in reality the 100 MeV proton is likely to escape the vertex region, so its energy will be deposited outside of the 5x5x5 region. On the other hand, the two 50 MeV protons, being of a lower energy value, will deposit their energy in the vertex region and so their contribution towards the VA is larger than a single 100 MeV proton.

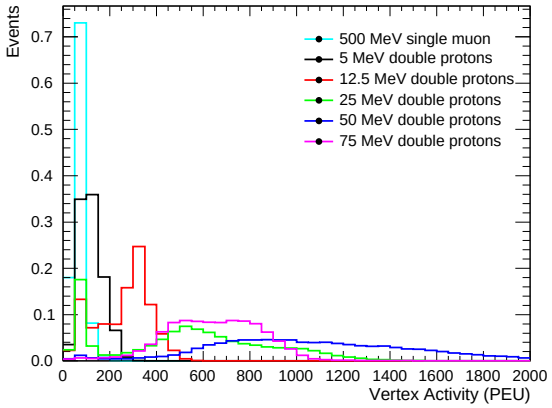

(a)

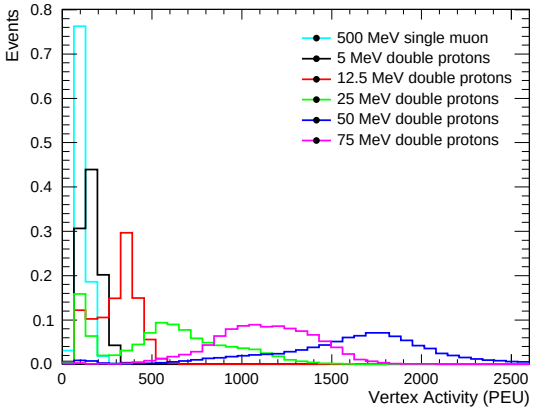

(b)

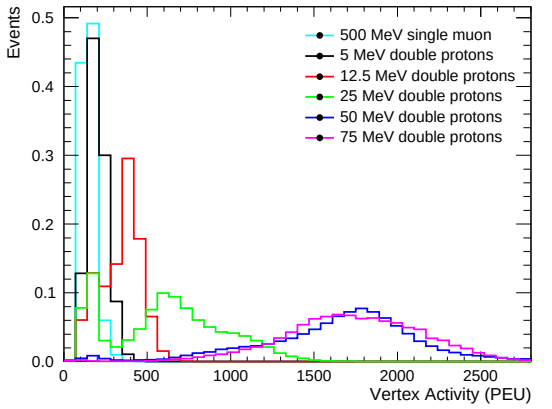

(c)

Figure 7.13: The vertex activity distribution for a single 500 MeV muon (cyan), as well as double protons, with an energy ranging from 5 MeV to 75 MeV, for the vertex regions: (a) 3x3x3 (b) 5x5x5 (c) 7x7x7.

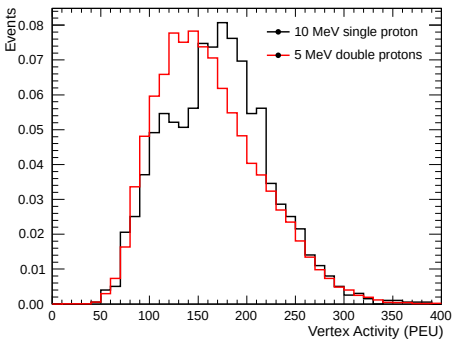

(a) Single 10 MeV proton and double 5 MeV protons

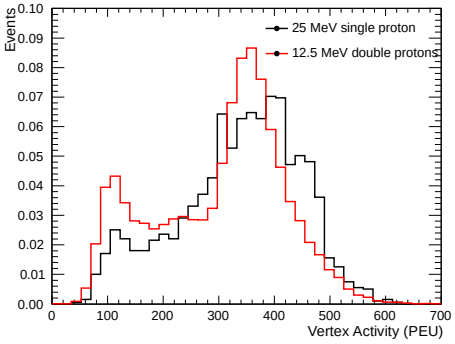

(b) Single 25 MeV proton and double 12.5 MeV protons

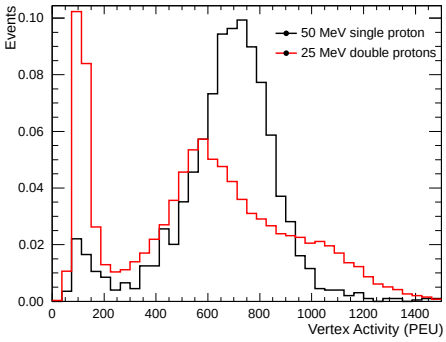

(c) Single 50 MeV proton and double 25 MeV protons

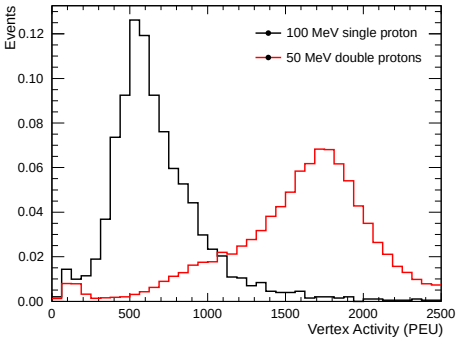

(d) Single 100 MeV proton and double 50 MeV protons

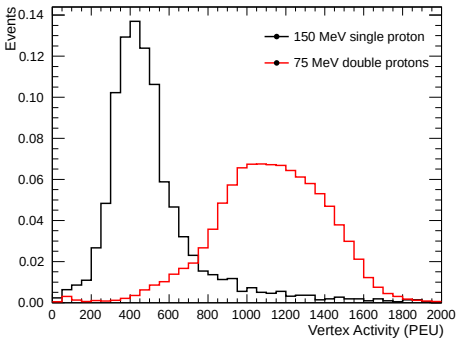

(e) Single 150 MeV proton and double 75 MeV protons

Figure 7.14: Vertex activity distributions for the single proton (black) compared to double proton (red) for the 5x5x5 vertex region. Up to 25 MeV, the single and double proton distributions similarly, but as the proton energy increases the distributions behave very differently. This effect is expected as higher energy protons will not remain in the 5x5x5 vertex region but will escape and deposit their energy elsewhere. The lower energy protons will deposit their energy in the vertex region and so will contribute more towards the VA. This effect is reflected most obviously for an overall proton energy $>$ 100 MeV.

7.3 Summary

This chapter has demonstrated that response functions can provide a lot of information regarding low energy particle production and can also be used to produce many different, and useful distributions, that cannot be easily determined otherwise. Single muon contributions to the VA are straightforward to calculate, as the muon track can be easily reconstructed in ND280 and the VA will be the reconstructed track. Moving towards additional interactions, such as a single proton is more complicated but possible, as has been shown in this chapter, if a single muon is simulated along with the proton. Using the information from these single muon and single proton distributions, one can create response functions, which allow predictions, such as VA values, of the single proton only MC.

As it is not possible to reconstruct low energy protons in ND280, the ability to use response functions is extremely important, as they allow single proton only distributions to be constructed.

The next chapter will discuss how the single proton response function can be used in order to investigate the low VA discrepancy present in the muon neutrino sample and whether adding low energy protons can help improve the data and MC disagreement.

Chapter 8

Proton Vertex Activity Analysis

Chapter 6 concluded that the low VA discrepancy seen in the muon sample (Section 6.2.1) is likely to be caused by low energy production of protons that are not simulated correctly by NEUT or GENIE. MINERνA also saw a similar problem in the agreements between data and MC, and investigations into the effect of adding low energy protons to the MC were performed [78].

For the MINERνA analysis, the MC generator used is GENIE v2.8.4 using the RFG nuclear model with a dipole axial form factor of M_A = 0.99 GeV, and the vertex region was defined as a sphere around the vertex point of dimensions of 30 g/cm^2 of material centered on the vertex. MINERνA found that adding protons with a momentum range of 0 - 225 MeV, 25 $\pm$ 1 (stat) $\pm$ 9 (sys) % of the time improved the data and MC agreement, and Figure 8.1 shows the improvement in the vertex energy distribution with the additional protons.

The CC ν-induced pion coherent production analysis using the proton module used GENIE v2.8.0 with a vertex region of $\pm$ 15cm, and this analysis found that adding protons with a momentum range of 0-100 MeV, 25% of the time improved the VA data and MC agreement. It should be noted that the proton module analysis is not a completed result yet, therefore there are no uncertainties associated with this measurement, and the analysis from MINERνA will be used as the main comparison in this chapter.

This chapter discusses whether adding single low momentum protons will improve the ND280 VA distributions, by reducing the low VA discrepancy.

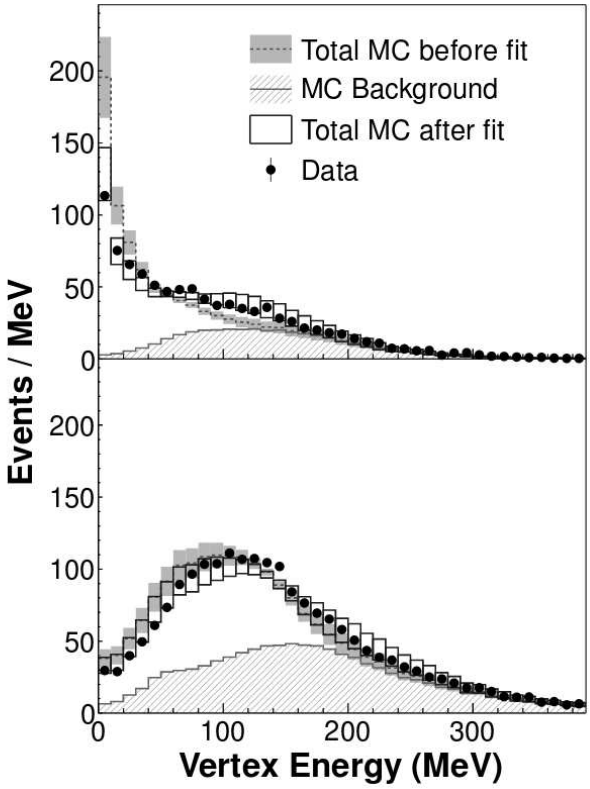

Figure 8.1: Result from MINERνA showing the reconstructed vertex energy of events passing the selection criteria in the data (points with statistical errors) compared to the GENIE RFG model (shown with systematic errors). The top plot is for: $Q^2_{QE} < 0.2$ GeV^2/c^2 and the bottom is for: $Q^2_{QE} > 0.2$ GeV^2/c^2 [78].

All the single proton fits in Section 7.11 were stored in a ROOT file and different combinations of their energies were added to the GENIE MC [1] at different fractions of the time. The χ^2 value between the data and new MC with additional proton contribution was determined, and the χ^2 value versus the percentage of proton added is shown by Figure 8.3 and in a 3D view in Figure 8.4 for each vertex box size. The distributions were fitted with a quadratic in order to extract the minimum χ^2 value to determine what percentage of proton added gives the best fit. The quadratic formula used to calculate the fit values is given by

$$y = a(x - b)^2 + c \tag{8.1}$$

where a is a constant, b is the x-axis value of the minimum χ^2 and c is the y-axis value of the minimum χ^2.

In terms of the energy range, it was found that imposing a limit on the proton energy below 200 MeV made no significant difference to the best fit value, for any of the vertex regions, as is shown by Figure 8.2. The optimal percentage of protons added for each vertex region, is listed in Table 8.1 for protons with an energy range between 10 - 200 MeV.

Vertex region	Optimal % $\pm$ error on %
3x3x3	62.694 $\pm$ 0.103
5x5x5	69.497 $\pm$ 0.123
7x7x7	71.762 $\pm$ 0.156

Table 8.1: The optimal percentage values after protons of energy 10 - 200 MeV were added to the GENIE MC.

The full best fit values can be found in the Results in Section 8.3.

VA plots for the optimal percent of events with protons to be added for data and MC are given by Figure 8.5 for GENIE MC.

[1] Only GENIE will be investigated in this chapter as it will allow for comparisons with the result seen at MINERνA. Unfortunately it was not possible to study NEUT, due to the fact that NEUT 6B contained a proton FSI bug at low momentum, and there was no truth information available with NEUT 6D at the time of the analysis.

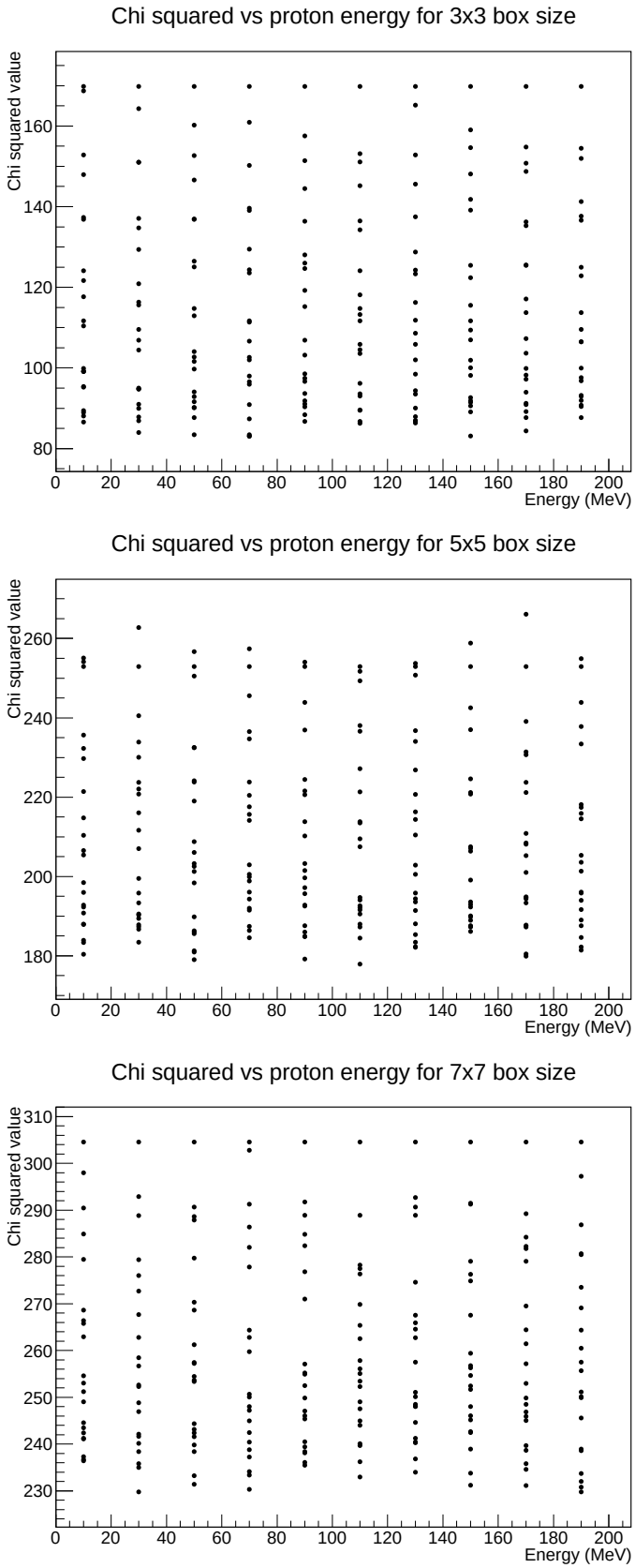

Figure 8.2: Chi squared value versus energy range for (a) 3x3x3 (b) 5x5x5 (c) 7x7x7. There is no obvious minimum for any of the vertex regions, suggesting that there is no energy dependence on the (10-200 MeV) protons added to the MC. It should be noted that the y-axis has been adjusted, compared to the previous χ^2 plots, in order to clearly show the χ^2 distribution across the energy range.

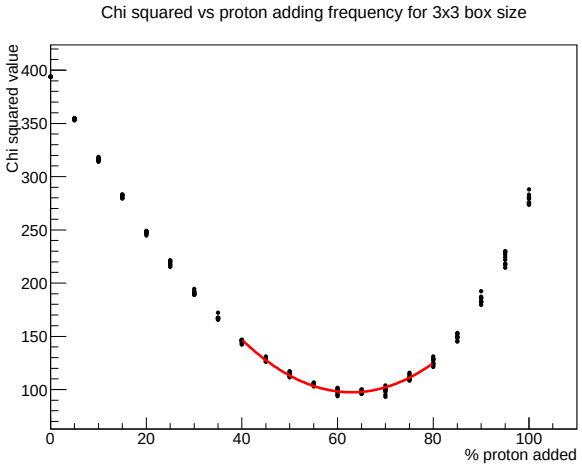

(a)

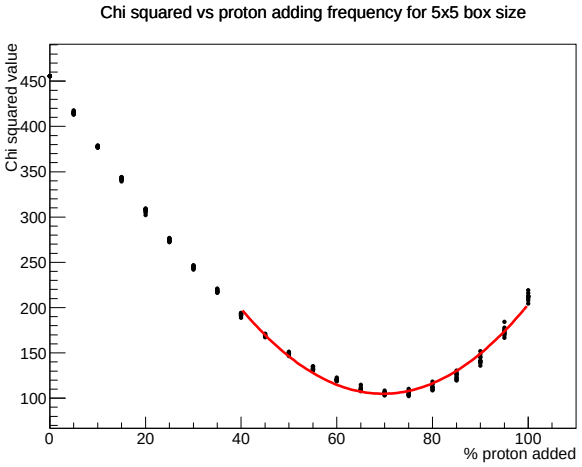

(b)

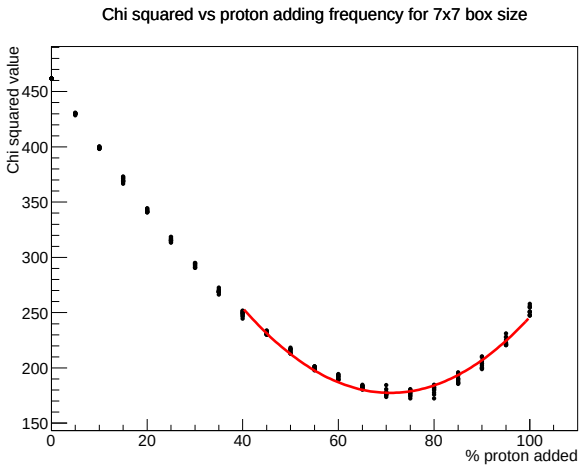

(c)

Figure 8.3: Chi square versus percent of proton added for vertex regions: (a) 3x3x3 (b) 5x5x5 (c) 7x7x7.

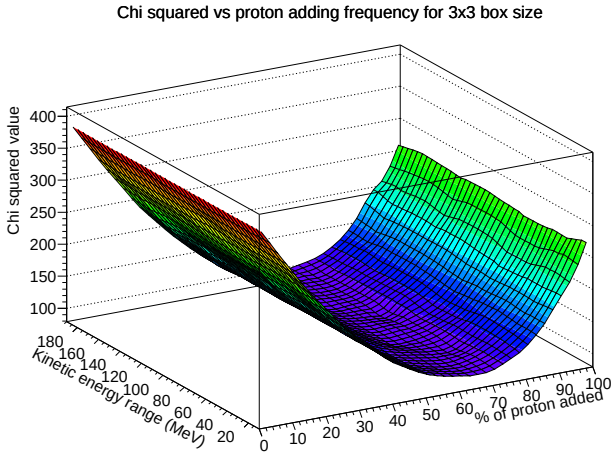

(a)

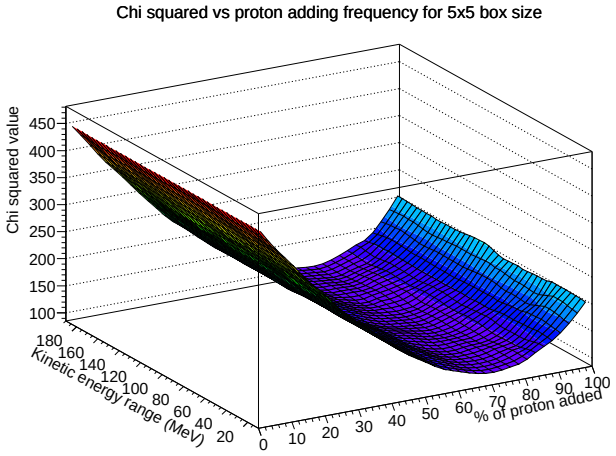

(b)

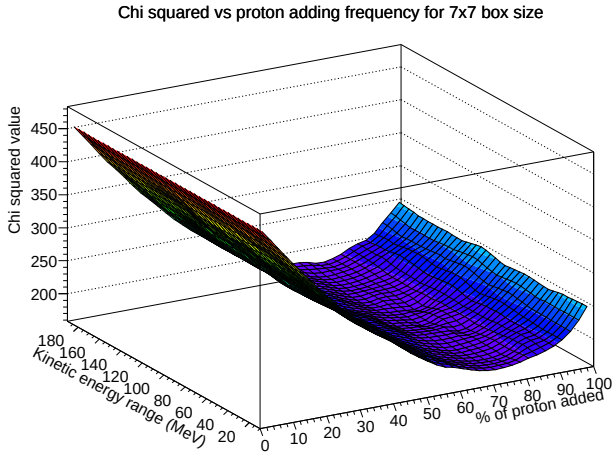

(c)

Figure 8.4: Chi squared values versus percentage of protons added versus KE (MeV) for vertex regions: (a) 3x3x3 (b) 5x5x5 (c) 7x7x7.

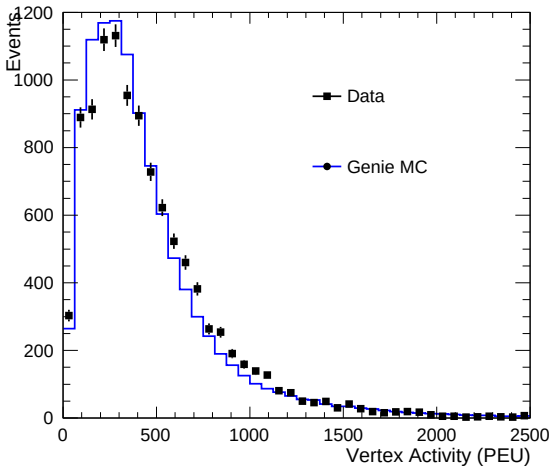

(a)

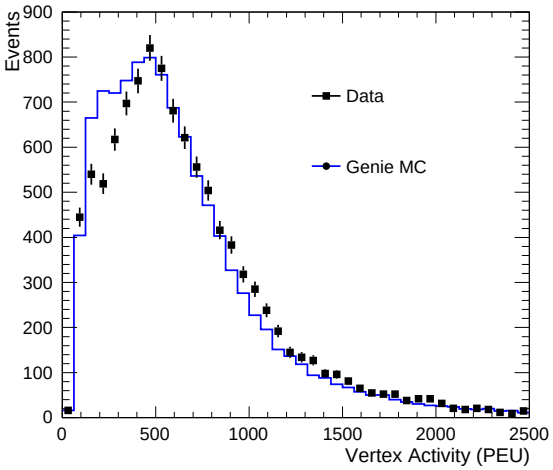

(b)

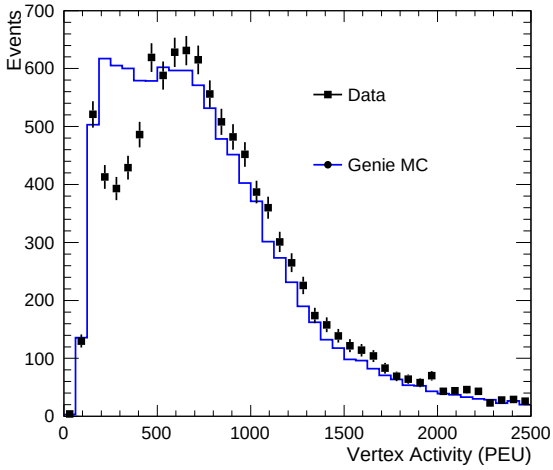

(c)

Figure 8.5: Vertex activity distribution after the optimal percentage of protons were added to Genie MC at vertex regions: (a) 3x3x3, 63% of the time (b) 5x5x5, 70% of the time (c) 7x7x7, 71% of the time.

8.1 Adding Protons Comparison

Having determined the best value for the percentage of protons to add to the MC, the VA distributions for the full data and MC were remade with the new proton contribution for each vertex region.

The original GENIE VA distributions were compared to the new samples with additional protons, and these are shown for each VA region by Figures 8.6, 8.7 and 8.8. The VA distributions show that by adding low energy protons a certain fraction of the time, depending on vertex size, to the MC, improves the data and MC agreement significantly. The high peak observed at low VA values in the original plot disappears, and there is clear improvement for each vertex region.

In addition, Tables 8.2, 8.3 and 8.4 show a comparison of the χ^2 values for the original distributions, when no protons are added, and after protons have been added to the MC, at the optimal percentage, for the 3x3x3, 5x5x5 and 7x7x7 vertex regions respectively; there is a clear improvement on the χ^2 value for all vertex regions after protons are added a certain fraction of the time.

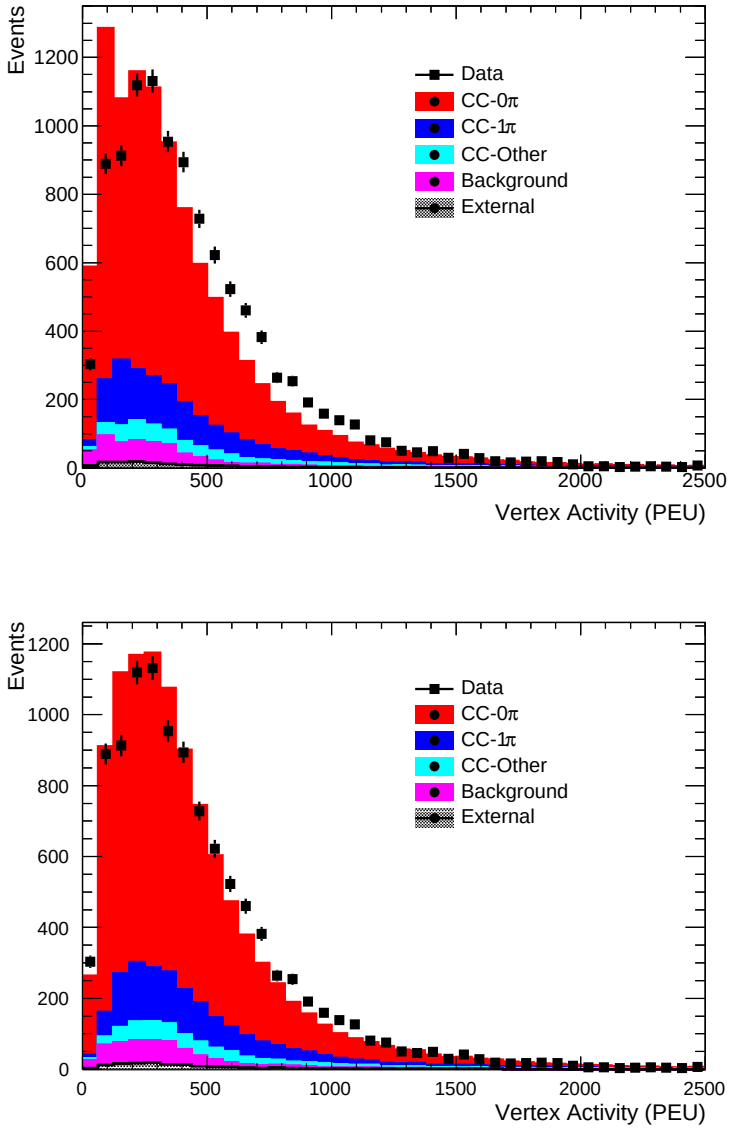

Figure 8.6: A comparison of the vertex activity distributions for the 3x3x3 vertex region, where the top plot is the original ν_μ GENIE MC sample and the bottom plot is the ν_μ GENIE MC sample with protons added 63% of the time with an energy range between 0-200 MeV. The bottom plot shows a clear improvement in the data and MC agreement after low energy protons are added to the MC.

Vertex region	χ^2/NDF	χ^2/NDF
	no protons added	protons added 63% of the time (optimal)
3x3x3	10.05	2.57

Table 8.2: A comparison of the χ^2 values when no protons have been added to the MC, and after the optimal percent of protons have been added to the MC. For the 3x3x3 region, the best fit percentage value was 63%, and a clear improvement on the χ^2 value is observed.

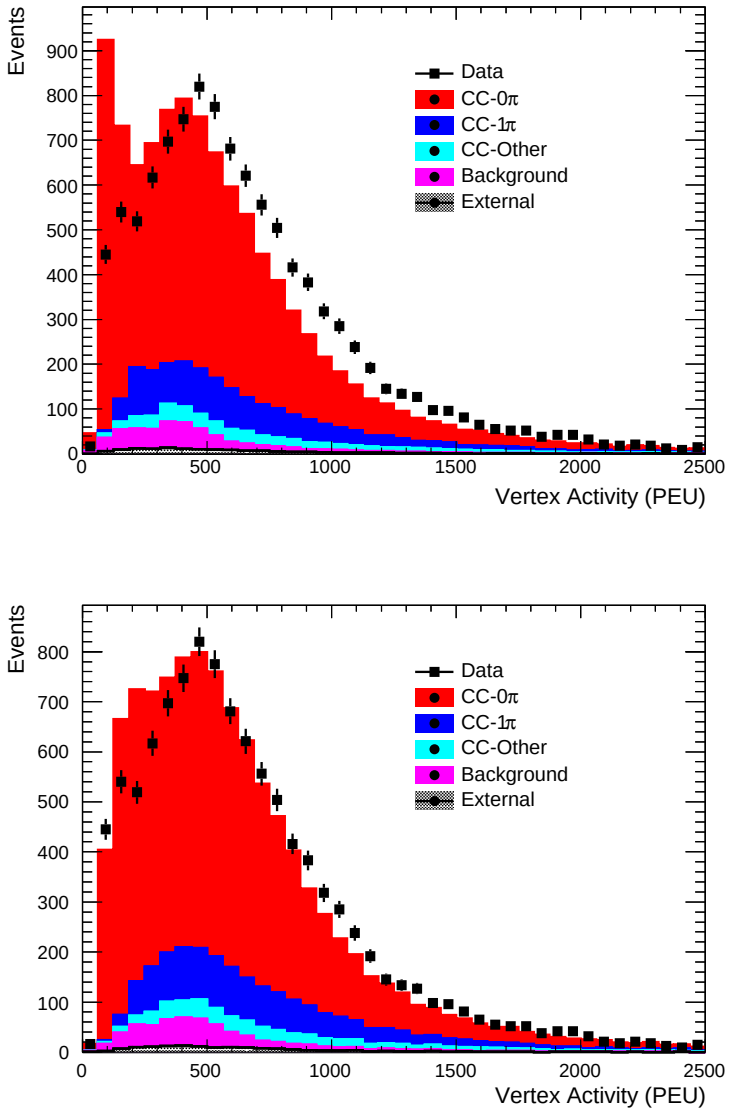

Figure 8.7: A comparison of the vertex activity distributions for the 5x5x5 vertex region. The top plot is the original ν_μ GENIE MC sample and the bottom plot is the ν_μ GENIE MC sample with protons added 70% of the time with an energy range between 0-200 MeV. The bottom plot shows a clear improvement in the data and MC agreement after low energy protons are added to the MC.

Vertex region	χ^2/NDF no protons added	χ^2/NDF protons added 70% of the time (optimal)
5x5x5	11.43	2.68

Table 8.3: A comparison of the χ^2 values when no protons have been added to the MC, and after the optimal percent of protons have been added to the MC. For the 5x5x5 region, the best fit percentage value was 70%, and a clear improvement on the χ^2 value is observed.

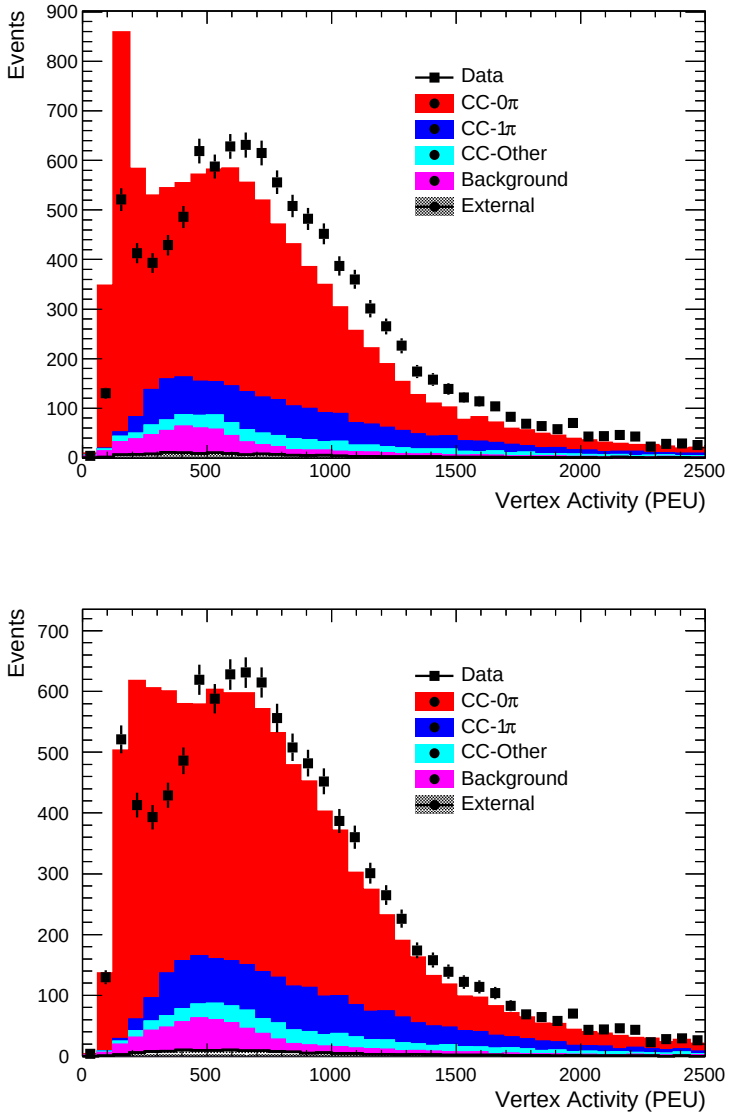

Figure 8.8: A comparison of the vertex activity distributions for the 7x7x7 vertex region. The top plot is the original ν_μ GENIE MC sample and the bottom plot is the ν_μ GENIE MC sample with protons added 71% of the time with an energy range between 0-200 MeV. The bottom plot shows a clear improvement in the data and MC agreement after low energy protons are added to the MC.

Vertex region	χ^2/NDF	χ^2/NDF
	no protons added	protons added 71% of the time (optimal)
7x7x7	11.53	4.44

Table 8.4: A comparison of the χ^2 values when no protons have been added to the MC, and after the optimal percent of protons have been added to the MC. For the 7x7x7 region, the best fit percentage value was 71%, and a clear improvement on the χ^2 value is observed.

8.2 Uncertainties

The statistical uncertainty on the proton vertex activity analysis was determined by the value when the minimum χ^2 increases by 1. This was deduced by using a fitted curve function as defined in Eq 8.1.

In terms of the systematic uncertainties, it is important to consider what has contributed to the final result and what could have affected this. The first systematic to consider is how accurately the MC matches the data. This is calculated using the control samples described in Section 6.4, where values for the systematic uncertainty on energy scale (mean) and resolution (sigma) of the FGD1 were obtained for a sample of stopping protons and throughgoing muons. Using these values, the mean of the single 500 MeV muon and the single 500 MeV muon plus single (10-200 MeV) proton distributions were adjusted. The difference in the data and MC of the mean and sigma values of the throughgoing muon and stopping proton sample in Section 6.4, were used to adjust the muon and proton distributions in order to account for any systematic uncertainty in the MC and data modelling. The difference in the mean and sigma for data and MC from the throughgoing muon sample was used to adjust the mean and sigma of the single 500 MeV muon sample only. For the single muon and single proton distributions, the differences in the data and MC for both the mean and sigma of the throughgoing muon and stopping proton samples were added in quadrature, and each mean and sigma of the single 500 MeV muon and (10-200 MeV) proton distribution was adjusted using these values. New single proton distributions were then built following the same procedure described previously, and protons from these adjusted single proton distributions were added to the MC as described in Section 7.2.2 to produce new VA distributions for each region, similar to those shown by Figures 8.6 to 8.8.

The muon and proton sample were treated differently to account for any effects caused by Birks Law [122], which describes the effect of light yield quenching for highly-ionising particles and can be expressed by the following equation which relates the light yield, dL to the energy loss dE:

$$dL = S.\frac{dE}{1 + k_B de/dx} \tag{8.2}$$

Incorporating the MIP to the muon component, and applying separately the stopping proton, to all of the stopping proton distributions is covering the variation from Birk's law as it's possible to distinguish between the different particles in the model. The stopping protons are giving a representative measure of what it's like for a proton

style dE/dx, and the muon provides a representative measure for the muon dE/dx. If further particles were introduced to the VA model, it would be possible to incorporate them, as pions are also minimum ionising so would be covered by the muon contributions, and electrons are heavily ionising so could use the proton contribution.

The same procedure, of adding low energy protons, as outlined in Section 8 was repeated, having adjusted the means and sigma to account for any systematic uncertainties, and new values for the optimal percent of protons added were determined by fitting the new χ^2 curves with a quadratic in the same way as previously. The difference in the new values compared to the previous percentages was taken as the systematic uncertainty for each vertex region.

Figure 8.9 shows a comparison for the 100 MeV single proton MC that has been adjusted to account for the systematic uncertainties compared to the normal 100 MeV single proton MC for the 5x5x5 vertex region.

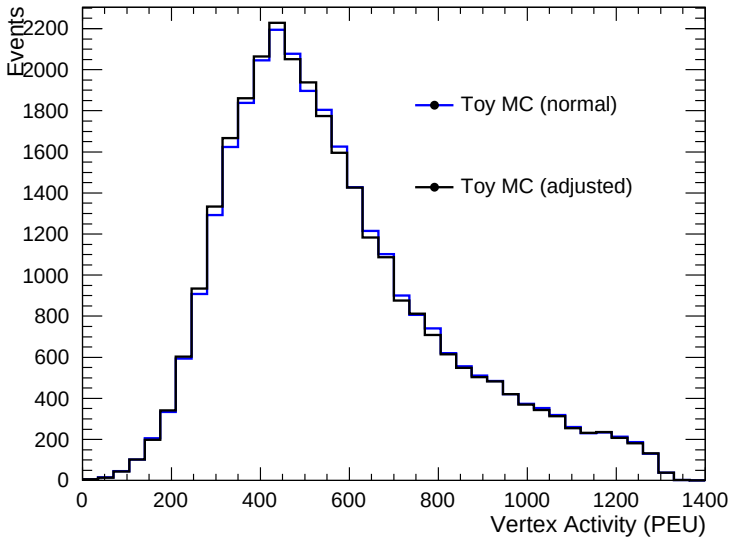

Figure 8.9: A comparison of the 100 MeV single proton MC after the mean and sigma have been adjusted according to the throughgoing muon and stopping proton systematic values (Toy MC (adjusted)), compared to the normal 100 MeV single proton MC (Toy MC (adjusted)) for the 5x5x5 vertex region.

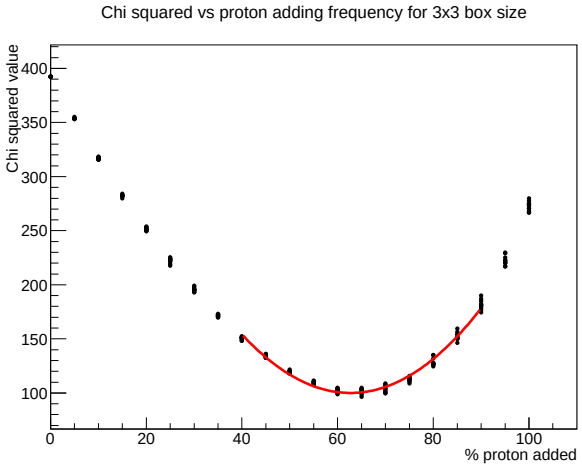

(a)

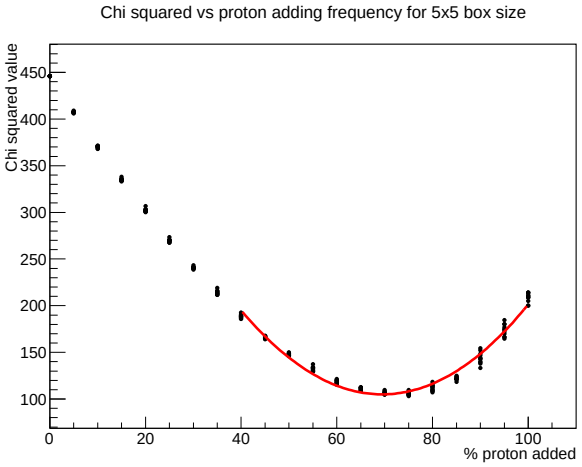

(b)

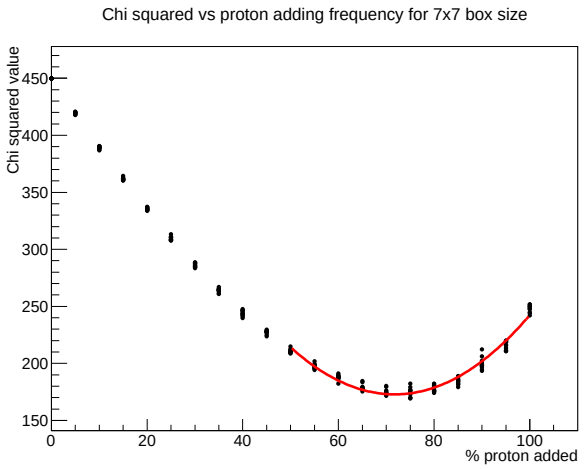

(c)

Figure 8.10: Chi square versus percent of proton added, adjusting for the systematic uncertainty, for vertex region: (a) 3x3x3 (b) 5x5x5 (c) 7x7x7.

Table 8.5 shows the systematic value for the normal χ^2 distribution (Figure 8.3) and the χ^2 distribution adjusted for the systematic values (Figure 8.10). The small differences between data and MC shown in Section 6.4 suggest that the MC is modelling the energy scale and resolution well, and this is reflected in a low systematic uncertainty resulting from these differences.

Vertex size	Fit min (normal)	Fit min (adjusted)	Difference
3x3x3	62.9	62.7	0.2
5x5x5	69.6	69.5	0.1
7x7x7	70.9	71.8	0.9

Table 8.5: Table outlining the minimum fit value for the normal distribution, as well as the adjusted distribution, and the difference between the two.

8.3 Results

The analysis determined that there was no dependence on the energy thus protons with the full energy range of 10-200 MeV were used. There is a clear dependence on the percentage of protons added into the MC and values for each vertex region were determined.

The final percentage values, as well as the statistical and systematic errors, for each vertex region are:

3x3x3: (62.9 $\pm$ 3.3 (stat) $\pm$ 0.2 (syst)) %

5x5x5: (69.6 $\pm$ 3.1 (stat) $\pm$ 0.1 (syst)) %

7x7x7: (70.9 $\pm$ 3.5 (stat) $\pm$ 0.9 (syst)) %.

MINERνA Comparison

MINERνA report that protons with an energy of 0-225 MeV added 25$\pm$1(stat) $\pm$ 9(syst) % of the time to the final state improves the excess of energy near the vertex.
Combining the statistical and systematic uncertainties from the MINERνA result gives a value of: (25 $\pm$ 9.1) %.

For the purposes of comparison between the MINERνA and ND280 result, the 5x5x5 vertex region of ND280 was selected as it provides the best compromise of allowing enough particles within the vertex region for a suitable VA measurement (the 3x3x3 region might not be representative of low energy particle production), but not too

many particles that it saturates the VA result, which might occur with the 7x7x7 region. Combining the 5x5x5 ND280 result in quadrature gives: (69.6 $\pm$ 3.1) %.

Using a standard consistency check

$$\sigma_{agreement} = \frac{|x_1 - x_2|}{\sqrt{\Delta x_1{}^2 + \Delta x_2{}^2}} \tag{8.3}$$

shows a discrepancy between the results of 4.6σ.

This difference is not entirely unexpected, as there are many reasons why the MINERνA and ND280 results may differ, including but not limited to:

- peak beam energy difference; 3 GeV (MINERνA) and 0.6 GeV (T2K)
- target material; 95% CH, 5% other material (MINERνA) and 86%(C), 7%(H), 4%(O), 2%(Ti), 1%(Si) (T2K)
- GENIE model used; v2.8.4 (MINERνA) and v2.8.0 (T2K)
- definition of vertex size; sphere around the vertex with a radius sufficient to contain a proton with 225 MeV KE (MINERνA) and layers deep x bars high x bars wide of 5x5x5 (T2K)
- KE range of protons; 0-225 MeV (MINERνA) and 10-200 MeV (T2K)

However it is clear that both experiments observe an underprediction of the production of low energy protons in the GENIE models used, leading to a discrepancy in the low VA distribution, which is greatly improved by artificially adding single proton contributions to the MC.

Chapter 9

Conclusions

The current state of understanding of multinucleon effects still requires further study and development of the theory. Future experiments will use much more complicated models therefore there needs to be a better comprehension behind these low energy theories.

The VA measurement gives an extra piece of information regarding the low energy particle production and is the only way for T2K and other experiments to assess the low energy particles that are produced during neutrino-nucleon interactions. As neutrino models become more sophisticated and uncertainties decrease, the VA will become increasingly important, as any added information regarding particles that are sensitive to the nuclear effects will become important for the generators.

During the analysis chapters, a use of VA has been demonstrated and via the response functions a mechanism in which MC models can start to be verified has been provided. The GENIE model examined during the proton VA analysis in Chapter 8, has been shown to have a clear underprediction of low energy proton production, both at MINERνA and ND280, in the results presented in this thesis. The VA study demonstrates that although the low energy protons cannot be reconstructed, their effect is visible in the data and that a new handle can, in the future, be used to further tune the cross section models.

This thesis demonstrates the first step in the use of VA in ND280, and shows for the first time that viable information regarding low energy proton production can be provided by the VA. The future outlook for the VA would be to utilise this information further, in order to assess different MC generators and their models. The VA has been shown to be a useful tool in the verification of generator models, and as these models are improved further, the systematic uncertainties of oscillation parameters will ultimately be reduced.

Appendix A

9.1 Full list of Mismapped Channels

Module	RMM	TFB	Channel ID	Bar	Layer
Top Left	3	6	2283301920	0	24
Top Left	3	6	2283301928	2	24
Top Left	3	6	2283301952	0	16
Top Left	3	6	2283301961	2	18
Top Left	3	6	2283301984	4	16
Top Left	3	6	2283301989	5	18
Top Left	3	6	2283301957	1	18
Top Left	3	6	2283301965	3	18
Top Left	3	6	2283301985	4	18
Top Left	3	6	2283301991	5	22
Bottom Left	4	4	2283818026	77	0
Bottom Left	4	4	2283818027	77	6
Bottom Left	4	34	2283940896	71	2
Bottom Left	4	34	2283940911	68	4
Bottom Left	4	34	2283940897	71	4
Bottom Left	4	34	2283940910	68	2
Bottom Left	4	34	2283940898	71	6
Bottom Left	4	34	2283940909	68	0
Bottom Left	4	34	2283940899	71	0
Bottom Left	4	34	2283940908	68	6
Bottom Left	4	34	2283940900	70	2
Bottom Left	4	34	2283940907	69	2
Bottom Left	4	34	2283940901	70	4
Bottom Left	4	34	2283940905	69	4
Bottom Left	4	34	2283940902	70	6
Bottom Left	4	34	2283940906	69	0
Bottom Left	4	34	2283940903	70	0
Bottom Left	4	34	2283940904	69	2

Module	RMM	TFB	Channel ID	Bar	Layer
Side Left	5	0	2284325996	23	0
Side Left	5	0	2284325997	23	2
Side Left	5	17	2284395563	82	30
Side Left	5	17	2284395564	83	24
Side Left	5	17	2284395596	83	16
Side Left	5	17	2284395597	83	18
Side Left	5	19	2284403822	19	5
Side Left	5	19	2284403823	19	7
Side Left	5	23	2284420165	29	19
Side Left	5	23	2284420167	29	23
Side Right	8	4	2285915137	48	3
Side Right	8	4	2285915140	49	1
Side Right	8	14	2285956162	42	29
Side Right	8	14	2285956164	43	27
Side Right	8	21	2285984843	30	15
Side Right	8	21	2285984845	31	11
Side Right	8	22	2285988928	87	8
Side Right	8	22	2285988929	87	10
Side Right	8	23	2285992996	86	16
Side Right	8	23	2285992997	86	18
Side Right	9	1	2286427213	7	11
Side Right	9	1	2286427214	7	13
Side Right	9	20	2286505067	30	15
Side Right	9	20	2286505069	31	11
Side Right	10	24	2287045667	32	14
Side Right	10	24	2287045669	33	10
Side Right	10	36	2287094857	10	18
Side Right	10	26	2287094858	10	20
DsECal	0	23	2281798661	27	8
DsECal	0	23	2281798663	29	8
DsECal	1	0	2282228748	7	19
DsECal	1	0	2282228780	5	23
DsECal	1	5	2282249325	21	19
DsECal	1	5	2282249327	26	21

Table 9.1: Full list of the mismapped channels, including module type, RMM, TFB, bar and layer numbers.

Appendix B

9.2 GENIE plots

The detector study plots were extended to the GENIE MC, to further discredit the discrepancy in the ν_μ being related to the detector. Figure 9.1 shows that selecting the number of TPC tracks to be 0 causes the low VA discrepancy to disappear, regardless of the FGD-only track selection cut, which is the same effect as seen in NEUT.

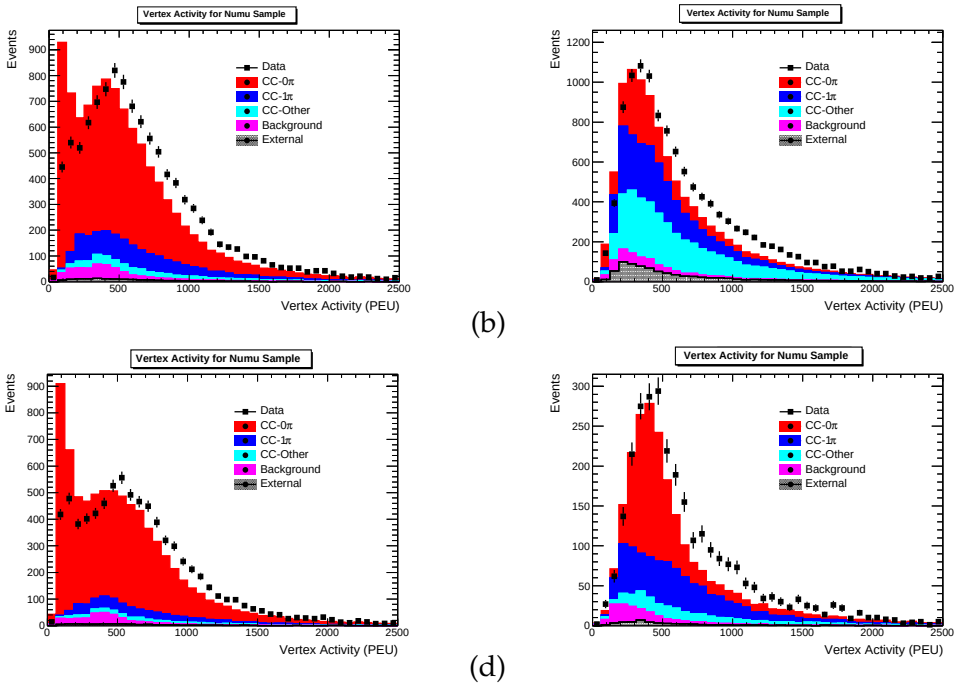

Figure 9.1: Varying the number of TPC tracks for GENIE (a) no. of TPC tracks = 1 (b) no. of TPC tracks $>$ 1 (c) no. of TPC tracks = 1 and no. of fgd only tracks = 0 (d) no. of TPC tracks = 1 and no. of fgd only tracks $>$ 0.

Figure 9.2 shows the effect on the VA after the FGD1 is separated into equally spaced z regions. There is no clear indication that altering the z position has an effect on the VA.

The final study varied the muon momentum form 200 MeV to greater than 700 MeV and the GENIE plots are given by Figure 9.3. There seems to be no obvious indication that the momentum affects the data and MC disagreement.

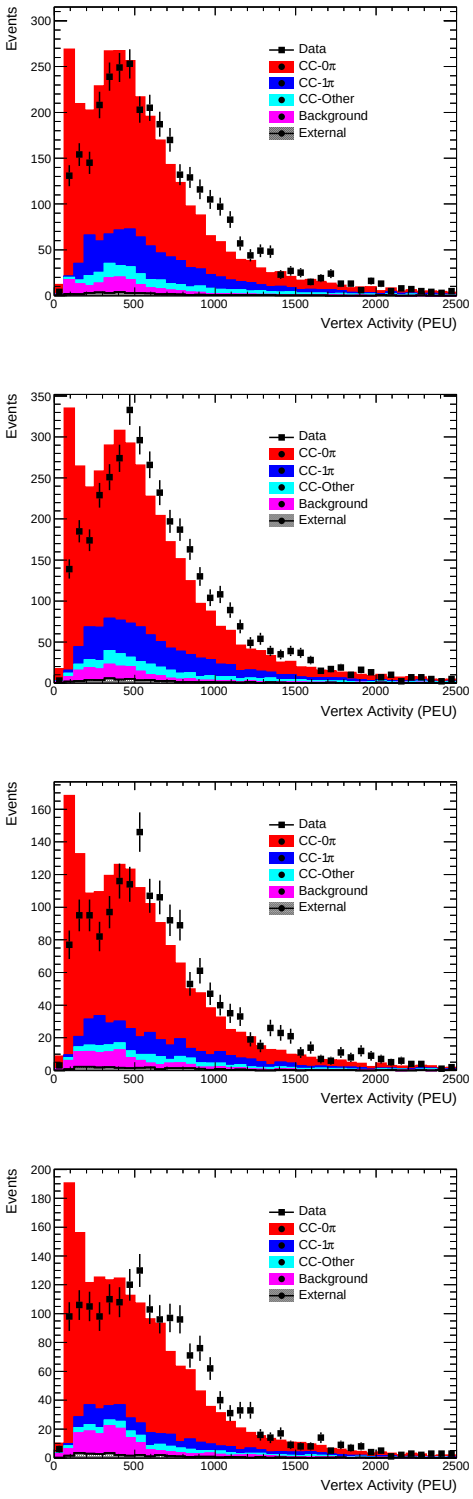

Figure 9.2: Plots showing the VA for FGD1 separated into four different z positions for GENIE MC.

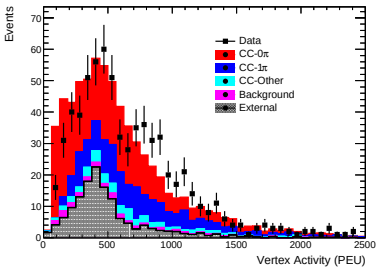

(a) Momentum = 200 - 300 MeV

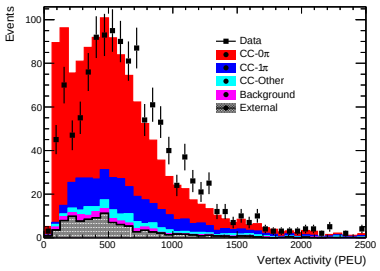

(b) Momentum = 300 - 400 MeV

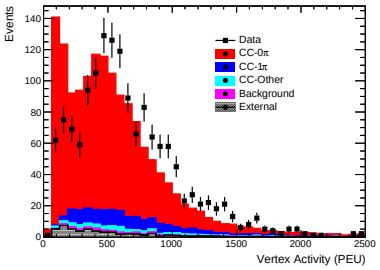

(c) Momentum = 400 - 500 MeV

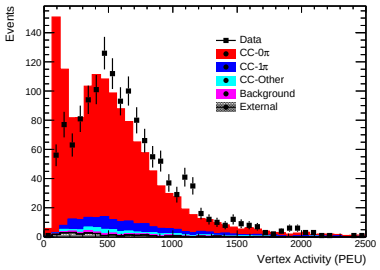

(d) Momentum = 500 - 600 MeV

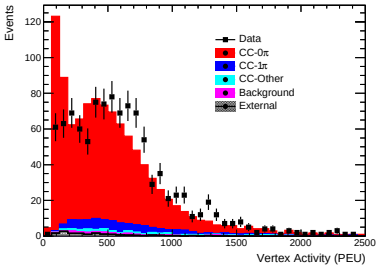

(e) Momentum = 600 - 700 MeV

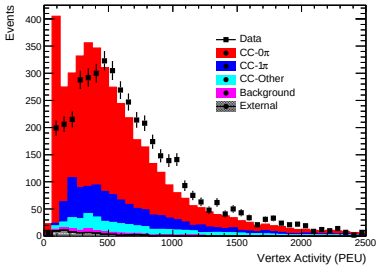

(f) Momentum = greater than 700 MeV

Figure 9.3: The vertex activity distributions separated into different momentum regions, the MC used for these distributions is GENIE.

Appendix C

9.3 Electron MC

Figure 9.4 shows an event display of a single 500 MeV electron (pink) simulated isotropically in the centre of FGD1. Electrons are likely to undergo bremstrahhlung as in this example shown by the spirals, and photons can also be produced which are shown by the yellow lines.

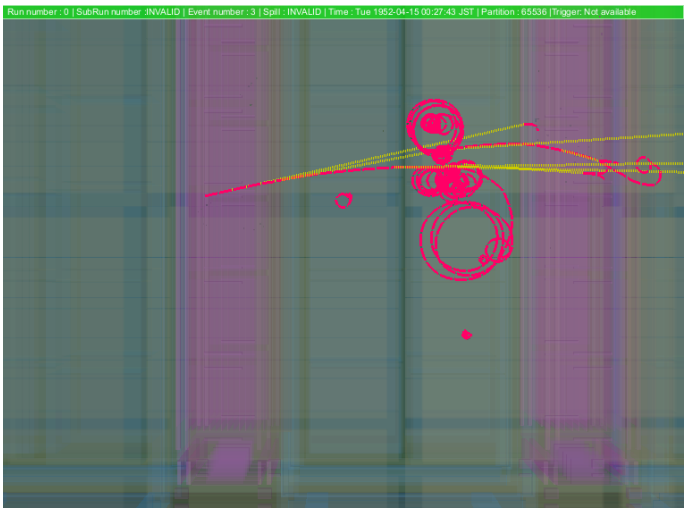

Figure 9.4: Event display showing a single 500 MeV electron (pink) undergoing bremstrahhlung and the resulting gammas (yellow) produced.

Figure 9.5 has been included in order to show the VA distribution for a single 500 MeV electron as well as a single 500 MeV electron plus single proton of varying energies, for the 5x5x5 vertex region.

Figure 9.6 shows a comparison of a single electron with two 50 MeV protons and a single muon with two 50 MeV protons. The difference between the electron and muon distributions is negligible; at low VA there is a slight difference between the low energy protons, however this is likely to be a statistical error.

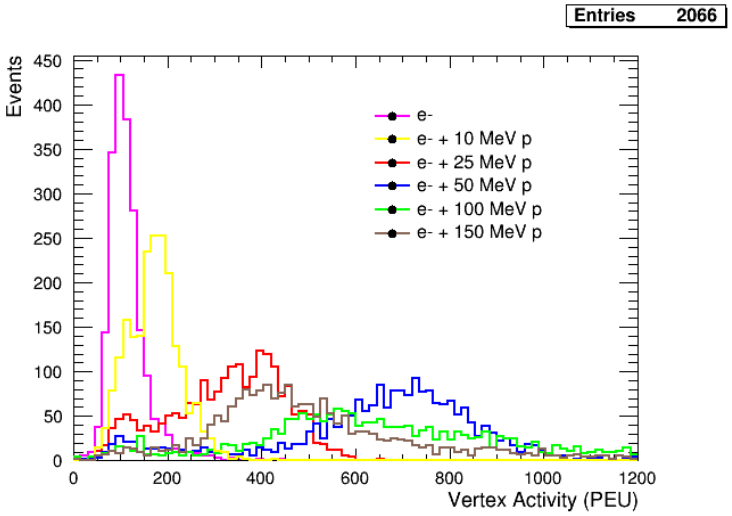

Figure 9.5: Single electron and single electron with single proton particle gun showing the vertex activity.

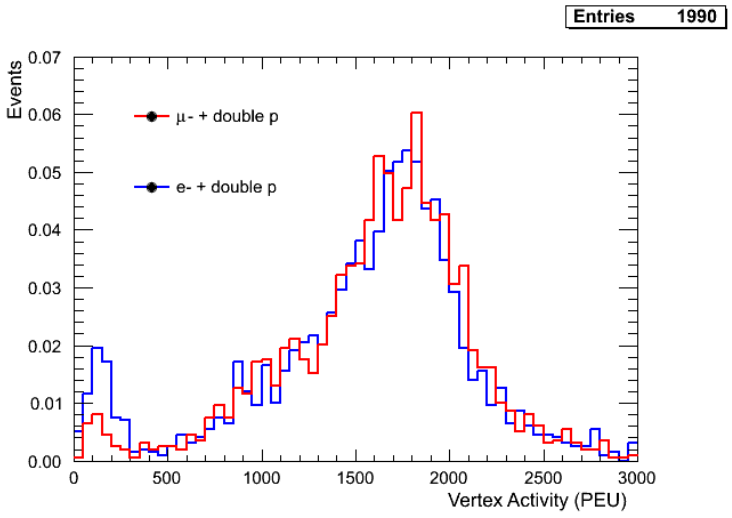

Figure 9.6: Vertex activity distribution of a single 500 MeV electron with two 50 MeV protons and a single 500 MeV muon with two 50 MeV protons.

Appendix D

9.4 Landau-gauss fits, V55

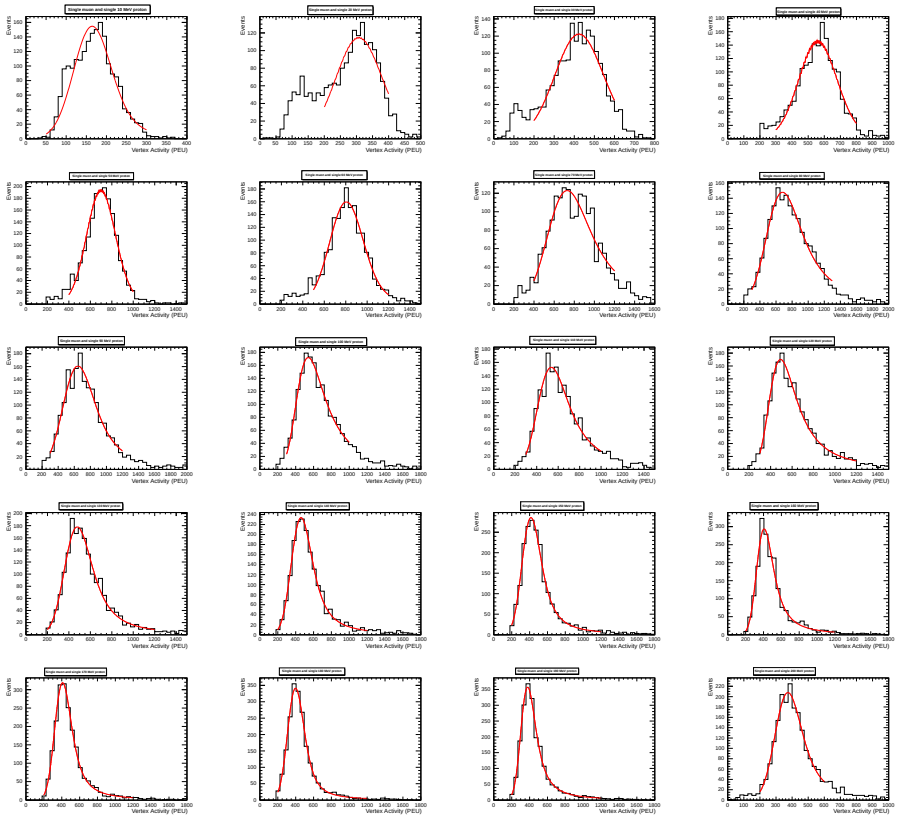

Figure 9.7: 500 MeV muon and single proton with energy 10-200 MeV fitted with a Landau-Gaussian for the 5x5x5 vertex region.

Appendix E

9.5 Single Proton Toy MC, V3x3x3

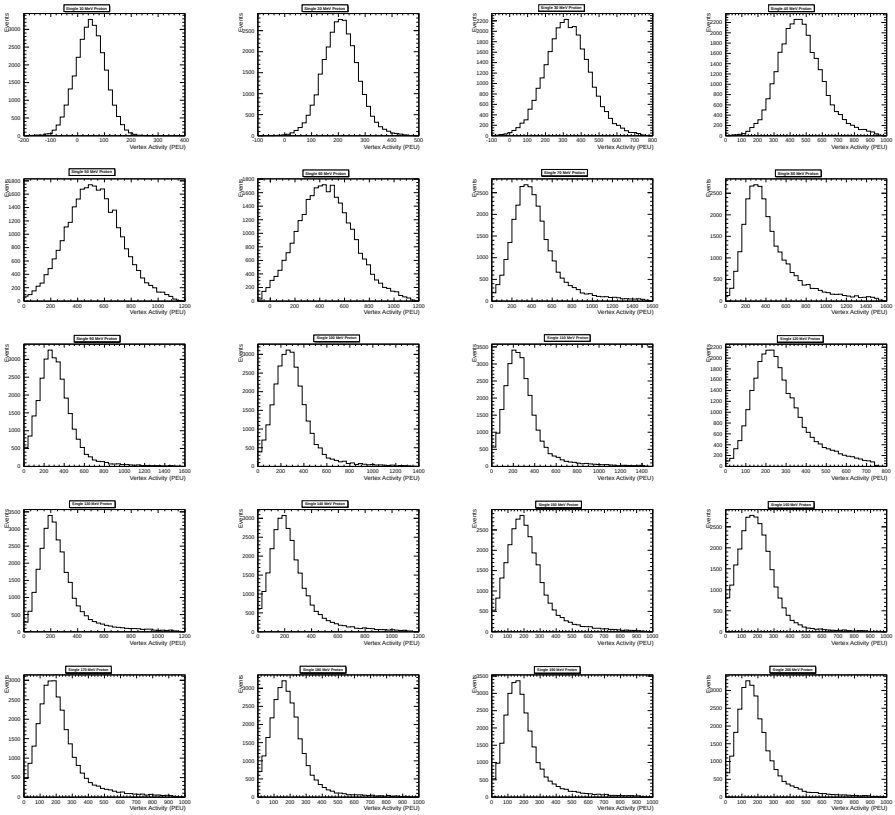

Figure 9.8: Single proton with energy 10-200 MeV for the 3x3x3 vertex region.

9.6 Single Proton Toy MC, V5x5x5

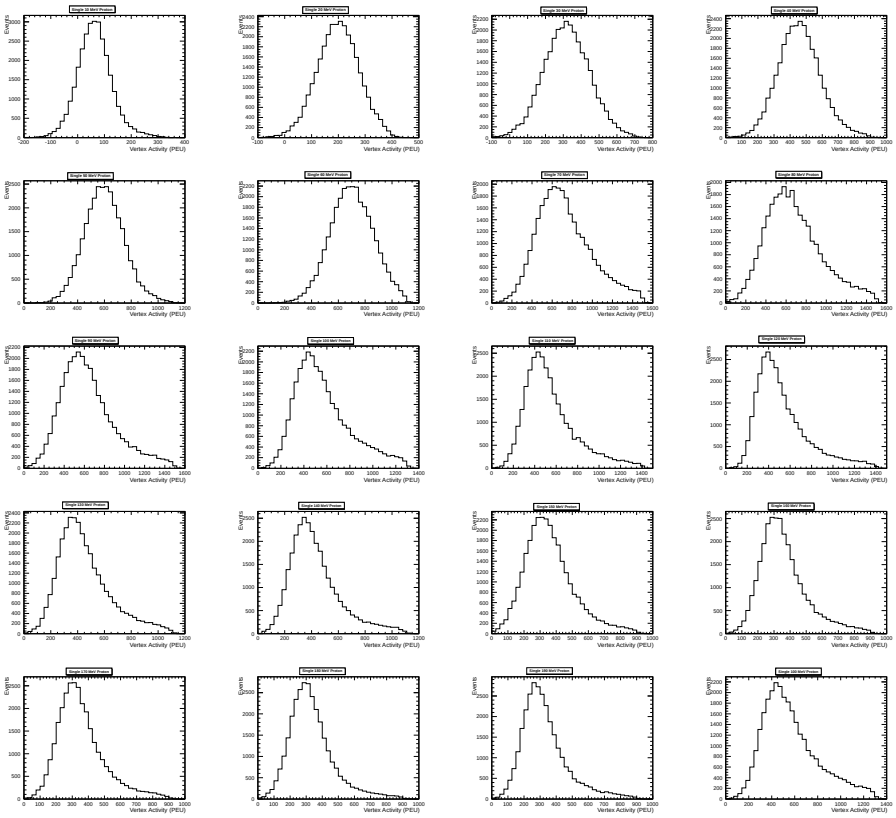

Figure 9.9: Single proton with energy 10-200 MeV for the 5x5x5 vertex region.

9.7 Single Proton Toy MC, V7x7x7

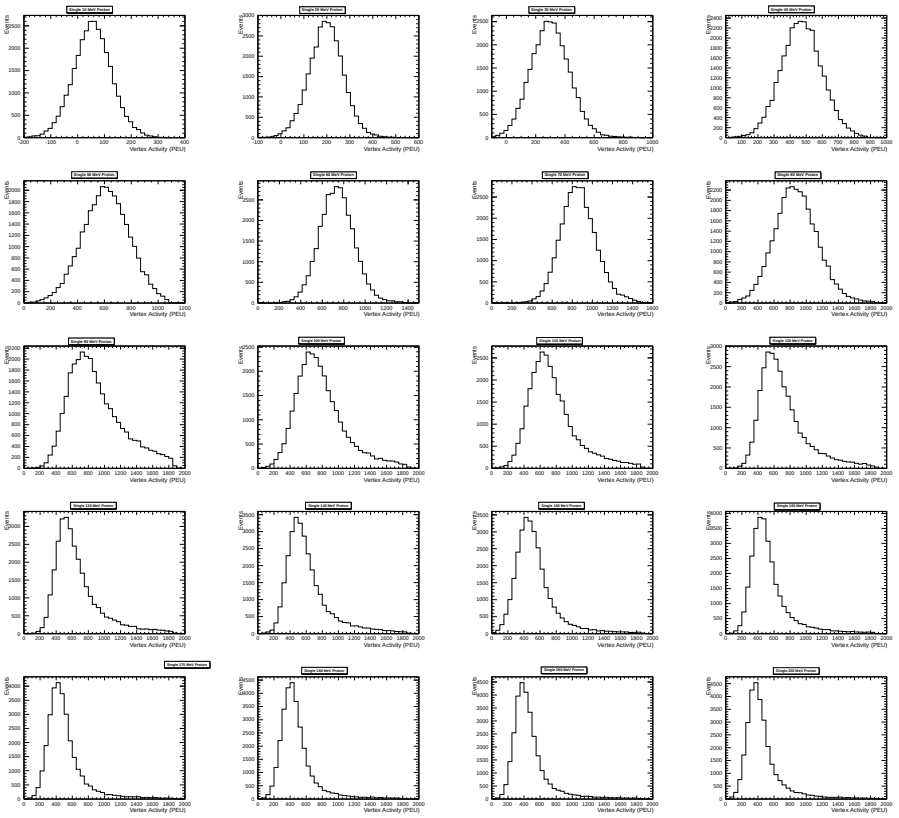

Figure 9.10: Single proton with energy 10-200 MeV for the 7x7x7 vertex region.

Appendix F

9.8 Particle gun and Toy MC comparison, V3x3x3

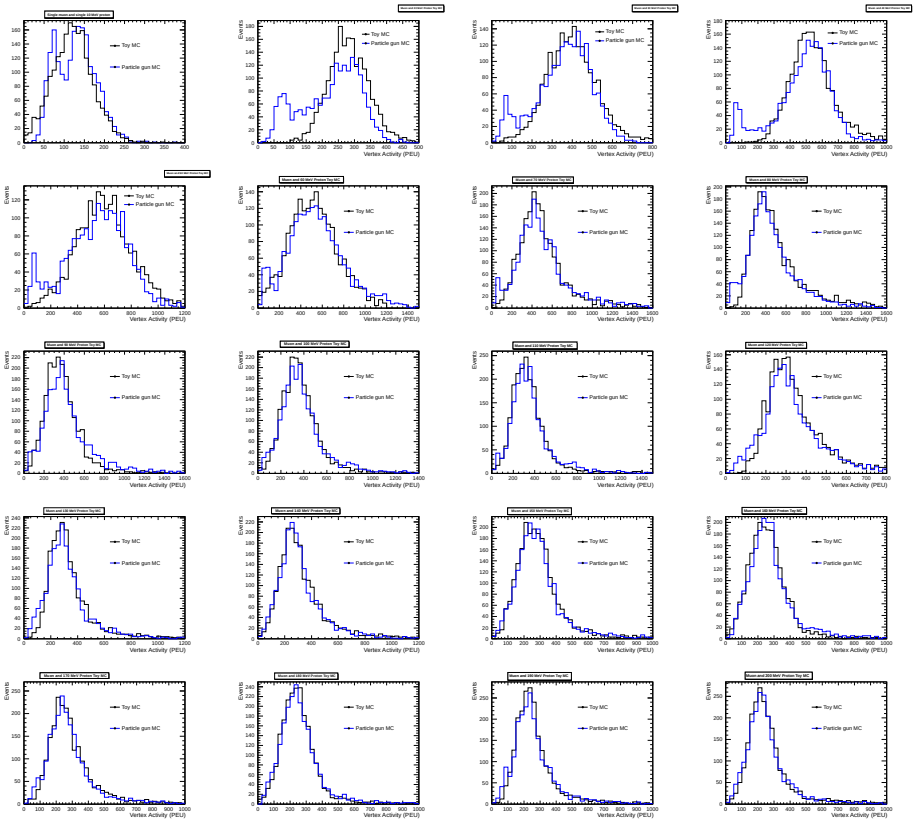

Figure 9.11: Original MC (Particle gun MC, blue) and new toy MC (black) comparison for a 500 MeV single muon with a 10-200 MeV single proton in the 3x3x3 vertex region.

9.9 Particle gun and Toy MC comparison, V5x5x5

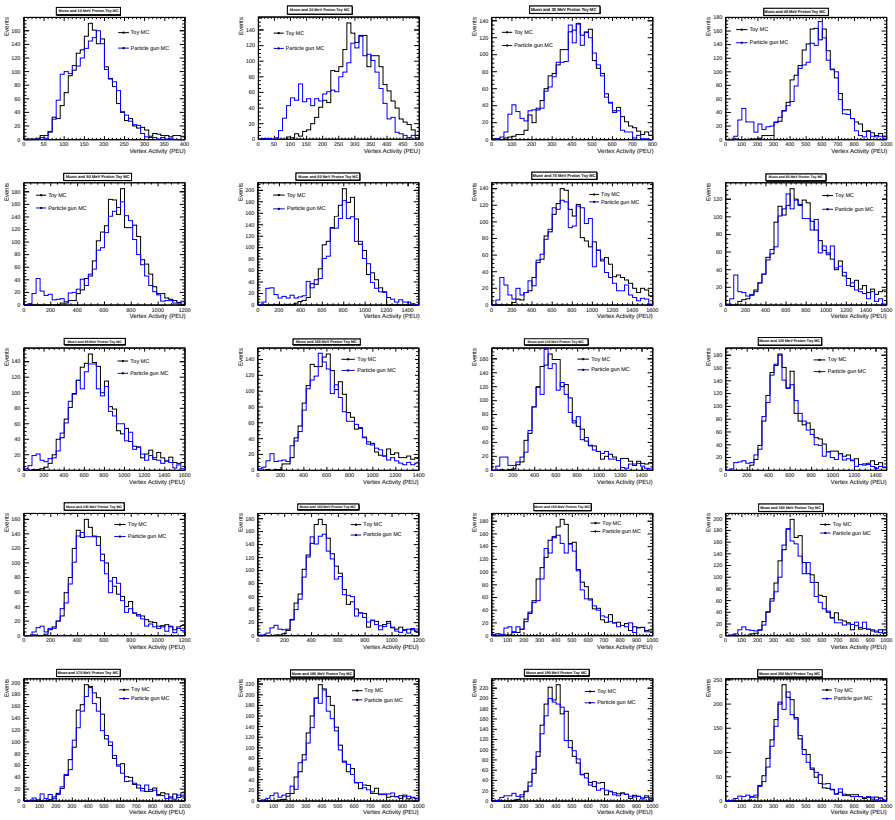

Figure 9.12: Original MC (Particle gun MC, black) and new toy MC (black) comparison for a 500 MeV single muon with a 10-200 MeV single proton in the 5x5x5 vertex region.

9.10 Particle gun and Toy MC comparison, V7x7x7

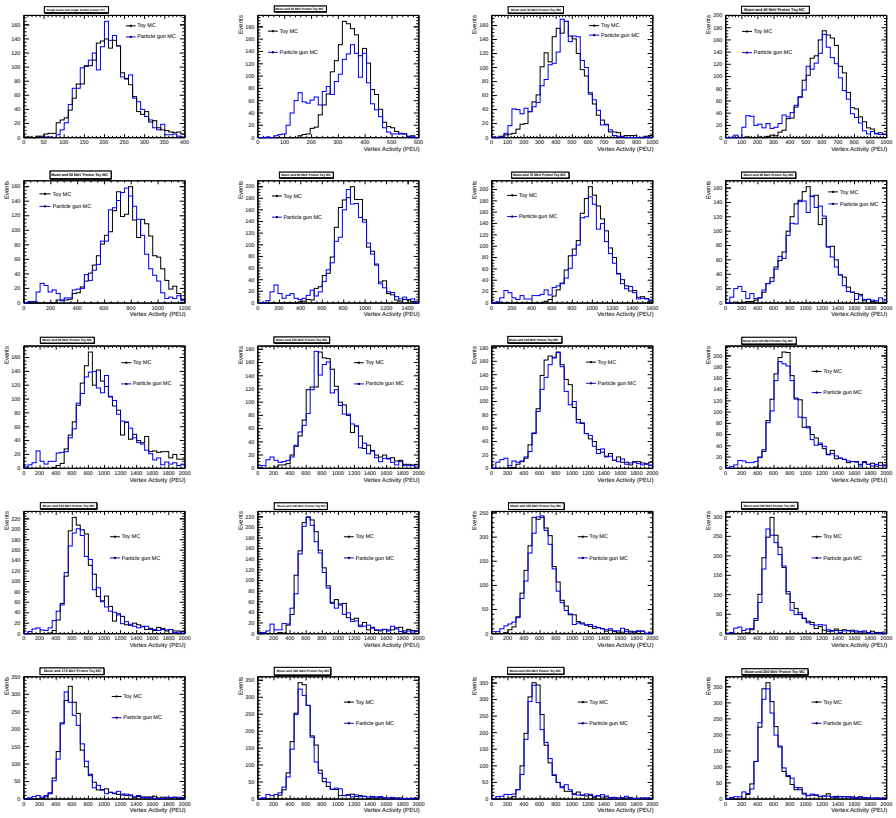

Figure 9.13: Original MC (Particle gun MC, blue) and new toy MC (black) comparison for a 500 MeV single muon with a 10-200 MeV single proton in the 7x7x7 vertex region.

Bibliography

[1] Georges Aad et al. Observation of a new particle in the search for the Standard Model Higgs boson with the ATLAS detector at the LHC. *Phys. Lett.*, B716:1–29, 2012.

[2] Beringer, J. and others. Review of Particle Physics. *Phys. Rev. D*, 86:010001, Jul 2012.

[3] Henri Becquerel. On the rays emitted by phosphorescence. *Compt. Rend. Hebd. Seances Acad. Sci.*, 122(8):420–421, 1896.

[4] E. Rutherford M.A. B.Sc. Viii. uranium radiation and the electrical conduction produced by it. *The London, Edinburgh, and Dublin Philosophical Magazine and Journal of Science*, 47(284):109–163, 1899.

[5] J. Chadwick. Intensitätsverteilung im magnetischen Spektrum der Beta-Strahlen von Radium B+C,. *Verhandlungen der Deutschen Physikalischen Gesellschaft*, 16:383–391, 1914.

[6] W. Pauli. Public letter to the group of the Radioactives at the district society meeting in Tubingen. *Cambridge Monogr. Part. Phys. Nucl. Phys. Cosmol.*, 14(1), Dec 2000.

[7] E. Fermi. Versuch einer Theorie der β-Strahlen. I. *Zeitschrift für Physik*, 88(3):161–177, Mar 1934.

[8] G. Danby, J. M. Gaillard, Konstantin A. Goulianos, L. M. Lederman, Nari B. Mistry, M. Schwartz, and J. Steinberger. Observation of High-Energy Neutrino Reactions and the Existence of Two Kinds of Neutrinos. *Phys. Rev. Lett.*, 9:36–44, 1962.

[9] Perl, M. L. and others. Evidence for Anomalous Lepton Production in $e^+ - e^-$ Annihilation. *Phys. Rev. Lett.*, 35:1489–1492, Dec 1975.

[10] K. Kodama et al. Observation of tau neutrino interactions. *Physics Letters B*, 504(3):218 – 224, 2001.

[11] Patricia R. Burchat. Review of the decay of the tau lepton. *AIP Conference Proceedings*, 150(1):981–986, 1986.

[12] A. Aguilar-Arevalo et al. Evidence for neutrino oscillations from the observation of anti-neutrino(electron) appearance in a anti-neutrino(muon) beam. *Phys. Rev.*, D64:112007, 2001.

[13] A. A. Aguilar-Arevalo and others. Search for electron neutrino appearance at the $\Delta m^2 \sim 1$ ev^2 scale. *Phys. Rev. Lett.*, 98:231801, Jun 2007.

[14] A. A. Aguilar-Arevalo et al. Observation of a Significant Excess of Electron-Like Events in the MiniBooNE Short-Baseline Neutrino Experiment. 2018.

[15] B. T. Cleveland, Timothy Daily, Raymond Davis, Jr., James R. Distel, Kenneth Lande, C. K. Lee, Paul S. Wildenhain, and Jack Ullman. Measurement of the solar electron neutrino flux with the Homestake chlorine detector. *Astrophys. J.*, 496:505–526, 1998.

[16] J. N. Bahcall et al. Solar Neutrino Flux. *Astrophysical Journal*, 137:344–346, 1963.

[17] John N. Bahcall and Carlos Pena-Garay. Solar models and solar neutrino oscillations. *New J. Phys.*, 6:63, 2004.

[18] Y. Fukuda et al. Atmospheric muon neutrino, electron neutrino ratio in the multi-gev energy range. *Physics Letters B*, 335(2):237 – 245, 1994.

[19] K.S. Hirata et al. Observation of B-8 solar neutrinos in the Kamiokande-II detector. *Physical Review Letters*, 63:16–19, July 1989.

[20] M. Cribier et al. Results of the whole GALLEX experiment. *Nuclear Physics B - Proceedings Supplements*, 70(1):284 – 291, 1999. Proceedings of the Fifth International Workshop on topics in Astroparticle and Underground Physics.

[21] M. Altmann et al. Complete results for five years of GNO solar neutrino observations. *Physics Letters B*, 616(3):174 – 190, 2005.

[22] J. N. Abdurashitov et al. Solar neutrino flux measurements by the Soviet-American gallium experiment (SAGE) for half the 22-year solar cycle. *Journal of Experimental and Theoretical Physics*, 95(2):181–193, Aug 2002.

[23] S. et al. Fukuda. Solar ^8b and hep neutrino measurements from 1258 days of super-kamiokande data. *Phys. Rev. Lett.*, 86:5651–5655, Jun 2001.

[24] Ahmad, Q. R. and others. Direct Evidence for Neutrino Flavor Transformation from Neutral-Current Interactions in the Sudbury Neutrino Observatory. *Phys. Rev. Lett.*, 89:011301, Jun 2002.

[25] B. Aharmim et al. Electron energy spectra, fluxes, and day-night asymmetries of B-8 solar neutrinos from measurements with NaCl dissolved in the heavy-water detector at the Sudbury Neutrino Observatory. *Phys. Rev.*, C72:055502, 2005.

[26] C.V. Achar, M.G.K. Menon, V.S. Narasimham, P.V.Ramana Murthy, B.V. Sreekantan, K. Hinotani, S. Miyake, D.R. Creed, J.L. Osborne, J.B.M. Pattison, and A.W. Wolfendale. Detection of muons produced by cosmic ray neutrinos deep underground. *Physics Letters*, 18(2):196 – 199, 1965.

[27] Reines, F. and Crouch, M. F. and Jenkins, T. L. and Kropp, W. R. and Gurr, H. S. and Smith, G. R. and Sellschop, J. P. F. and Meyer, B. Evidence for High-Energy Cosmic-Ray Neutrino Interactions. *Phys. Rev. Lett.*, 15:429–433, Aug 1965.

[28] K.S. Hirata et al. Experimental study of the atmospheric neutrino flux. *Physics Letters B*, 205(2):416 – 420, 1988.

[29] D. Casper and others. Measurement of atmospheric neutrino composition with the imb-3 detector. *Phys. Rev. Lett.*, 66:2561–2564, May 1991.

[30] Fukuda, Y. and others. Evidence for Oscillation of Atmospheric Neutrinos. *Phys. Rev. Lett.*, 81:1562–1567, Aug 1998.

[31] Y. Ashie et al. Evidence for an oscillatory signature in atmospheric neutrino oscillation. *Phys. Rev. Lett.*, 93:101801, 2004.

[32] M. Apollonio et al. Limits on neutrino oscillations from the CHOOZ experiment. *Phys. Lett.*, B466:415–430, 1999.

[33] F. Boehm et al. Final results from the palo verde neutrino oscillation experiment. *Phys. Rev. D*, 64:112001, Nov 2001.

[34] T. Araki et al. Measurement of neutrino oscillation with kamland, evidence of spectral distortion. *Phys. Rev. Lett.*, 94:081801, Mar 2005.

[35] F. P. An et al. Observation of electron antineutrino disappearance at daya bay. *Phys. Rev. Lett.*, 108:171803, Apr 2012.

[36] Y. Abe et al. Indication of reactor $\overline{\nu}_e$ disappearance in the double chooz experiment. *Phys. Rev. Lett.*, 108:131801, Mar 2012.

[37] J. K. Ahn et al. Observation of reactor electron antineutrinos disappearance in the reno experiment. *Phys. Rev. Lett.*, 108:191802, May 2012.

[38] Fengpeng An et al. Neutrino Physics with JUNO. *J. Phys.*, G43(3):030401, 2016.

[39] F. P. An et al. New Measurement of Antineutrino Oscillation with the Full Detector Configuration at Daya Bay. *Phys. Rev. Lett.*, 115(11):111802, 2015.

[40] M. H. Ahn et al. Measurement of neutrino oscillation by the k2k experiment. *Phys. Rev. D*, 74:072003, Oct 2006.

[41] P. Adamson et al. Measurement of neutrino oscillations with the minos detectors in the numi beam. *Phys. Rev. Lett.*, 101:131802, Sep 2008.

[42] K. Abe et al. The T2K Experiment. *Nucl. Instrum. Meth.*, A659:106–135, 2011.

[43] K. Abe et al. Evidence of Electron Neutrino Appearance in a Muon Neutrino Beam. *Phys. Rev.*, D88(3):032002, 2013.

[44] K Abe et al. Observation of electron neutrino appearance in a muon neutrino beam. *Physical review letters*, 112(6):061802, 2014.

[45] P. Adamson et al. Measurement of the neutrino mixing angle θ_{23} in nova. *Phys. Rev. Lett.*, 118:151802, Apr 2017.

[46] R. Acciarri et al. Long-Baseline Neutrino Facility (LBNF) and Deep Underground Neutrino Experiment (DUNE). 2015.

[47] K. Abe et al. A Long Baseline Neutrino Oscillation Experiment Using J-PARC Neutrino Beam and Hyper-Kamiokande. 2014.

[48] B. Pontecorvo. Mesonium and anti-mesonium. *Sov. Phys. JETP*, 6:429, 1957. [Zh. Eksp. Teor. Fiz.33,549(1957)].

[49] B. Pontecorvo. Neutrino Experiments and the Problem of Conservation of Leptonic Charge. *Sov. Phys. JETP*, 26:984–988, 1968. [Zh. Eksp. Teor. Fiz.53,1717(1967)].

[50] J. A. Formaggio and G. P. Zeller. From eV to EeV: Neutrino Cross Sections Across Energy Scales. *Rev. Mod. Phys.*, 84:1307–1341, 2012.

[51] S. F. King . Neutrino mass. *Contemporary Physics*, 48(4):195–211, 2007.

[52] M. Tanabashi et al. Particle data group. *Phys. Rev.*, D 98:030001, 2018.

[53] K. Abe et al. Combined analysis of neutrino and antineutrino oscillations at t2k. *Phys. Rev. Lett.*, 118:151801, Apr 2017.

[54] K. Abe et al. Search for CP Violation in Neutrino and Antineutrino Oscillations by the T2K Experiment with 2.2×10^{21} Protons on Target. *Phys. Rev. Lett.*, 121(17):171802, 2018.

[55] Yoshinari Hayato. A neutrino interaction simulation program library NEUT. *Acta Phys. Polon.*, B40:2477–2489, 2009.

[56] C. Andreopoulos et al. The GENIE Neutrino Monte Carlo Generator. *Nucl. Instrum. Meth.*, A614:87–104, 2010.

[57] C. Andreopoulos et al. The genie neutrino monte carlo generator. *Nuclear Instruments and Methods in Physics Research Section A: Accelerators, Spectrometers, Detectors and Associated Equipment*, 614(1):87 – 104, 2010.

[58] Omar Benhar, Adelchi Fabrocini, and Stefano Fantoni. The nucleon spectral function in nuclear matter. *Nuclear Physics A*, 505(2):267 – 299, 1989.

[59] R. A Smith and E. J Moniz. Neutrino reactions on nuclear targets. *Nuclear Physics B*, 101(43):605 – 622, 1972.

[60] A. Bodek and J. L. Ritchie. Further studies of fermi-motion effects in lepton scattering from nuclear targets. *Phys. Rev. D*, 24:1400–1402, Sep 1981.

[61] C. H. Llewellyn Smith. Neutrino Reactions at Accelerator Energies. *Phys. Rept.*, 3:261–379, 1972.

[62] Anthony William Thomas. CVC in particle physics. In *Non-nucleonic degrees of freedom detected in nuclei. Proceedings, International Symposium, NNDF'96, Osaka, Japan, September 2-5, 1996*, pages 142–149, 1996.

[63] M. Gell-Mann and M. Lévy. The axial vector current in beta decay. *Il Nuovo Cimento (1955-1965)*, 16(4):705–726, May 1960.

[64] S. J. Barish et al. Study of neutrino interactions in hydrogen and deuterium: Description of the experiment and study of the reaction $\nu + d \rightarrow \mu^- + p + p_s$. *Phys. Rev. D*, 16:3103–3121, Dec 1977.

[65] Veronique Bernard, Latifa Elouadrhiri, and Ulf-G. Meissner. Axial structure of the nucleon: Topical Review. *J. Phys.*, G28:R1–R35, 2002.

[66] Dieter Rein and Lalit M Sehgal. Neutrino-excitation of baryon resonances and single pion production. *Annals of Physics*, 133(1):79 – 153, 1981.

[67] R. Gran et al. Measurement of the quasi-elastic axial vector mass in neutrino-oxygen interactions. *Phys. Rev.*, D74:052002, 2006.

[68] A. A. Aguilar-Arevalo et al. First measurement of the muon neutrino charged current quasielastic double differential cross section. *Phys. Rev. D*, 81:092005, May 2010.

[69] Jose Luis Alcaraz-Aunion and Joseph Walding. Measurement of the nu(mu)-CCQE cross-section in the SciBooNE experiment. *AIP Conf. Proc.*, 1189:145–150, 2009.

[70] V. Lyubushkin and others. A study of quasi-elastic muon neutrino and antineutrino scattering in the nomad experiment. *The European Physical Journal C*, 63(3):355–381, Oct 2009.

[71] Nathan Mayer. Results for ccqe scattering with the minos near detector. *Journal of Physics: Conference Series*, 312(7):072010, 2011.

[72] K. Abe et al. Measurement of the ν_μ charged current quasielastic cross section on carbon with the T2K on-axis neutrino beam. *Phys. Rev.*, D91(11):112002, 2015.

[73] K. Gallmeister, U. Mosel, and J. Weil. Neutrino-induced reactions on nuclei. *Phys. Rev. C*, 94:035502, Sep 2016.

[74] J. Nieves, I. Ruiz Simo, and M. J. Vicente Vacas. Inclusive charged-current neutrino-nucleus reactions. *Phys. Rev. C*, 83:045501, Apr 2011.

[75] M. Martini, M. Ericson, G. Chanfray, and J. Marteau. Unified approach for nucleon knock-out and coherent and incoherent pion production in neutrino interactions with nuclei. *Phys. Rev. C*, 80:065501, Dec 2009.

[76] J. Nieves, I. Ruiz Simo, and M.J. Vicente Vacas. Two particle–hole excitations in charged current quasielastic antineutrino-nucleus scattering. *Physics Letters B*, 721(1):90 – 93, 2013.

[77] M. Martini, M. Ericson, and G. Chanfray. Neutrino quasielastic interaction and nuclear dynamics. *Phys. Rev. C*, 84:055502, Nov 2011.

[78] L. Fields et al. Measurement of Muon Antineutrino QE scattering on a Hydrocarbon Target at Ev around 3.5 GeV. *Phys. Rev. Lett.*, 111(2):022501, 2013.

[79] Costas Andreopoulos et al. The GENIE Neutrino Monte Carlo Generator: Physics and User Manual. 2015.

[80] Matthew Bass. The Short Baseline Neutrino Oscillation Program at Fermilab. *PoS*, ICHEP2016:481, 2016.

[81] K. Abe et al. Neutrino oscillation physics potential of the T2K experiment. *PTEP*, 2015(4):043C01, 2015.

[82] T2K. T2K Collaboration Photos, 2018.

[83] T. Sekiguchi et al. Development and operational experience of magnetic horn system for t2k experiment. *Nuclear Instruments and Methods in Physics Research Section A: Accelerators, Spectrometers, Detectors and Associated Equipment*, 789:57 – 80, 2015.

[84] Abe, K. and others. T2K neutrino flux prediction. *Phys. Rev. D*, 87:012001, Jan 2013.

[85] Carter, A. A. and others. Pion-Nucleon Total Cross Sections from 0.5 to 2.65 GeV/c. *Phys. Rev.*, 168:1457–1465, Apr 1968.

[86] Ferrari, Alfredo and Sala, Paola R. and Fasso, Alberto and Ranft, Johannes. FLUKA: A multi-particle transport code. *CERN Yellow Reports*, 2005.

[87] René Brun, F. Bruyant, Federico Carminati, Simone Giani, M. Maire, A. McPherson, G. Patrick, and L. Urban. GEANT Detector Description and Simulation Tool. *CERN Program Library*, 1994.

[88] C. Zeitnitz and T. A. Gabriel. The GEANT - CALOR interface and benchmark calculations of ZEUS test calorimeters. *Nucl. Instrum. Meth.*, A349:106–111, 1994.

[89] S. Fukuda et al. The super-kamiokande detector. *Nuclear Instruments and Methods in Physics Research Section A: Accelerators, Spectrometers, Detectors and Associated Equipment*, 501(2):418 – 462, 2003.

[90] Evgeny K. Akhmedov, A. Dighe, P. Lipari, and A. Y. Smirnov. Atmospheric neutrinos at Super-Kamiokande and parametric resonance in neutrino oscillations. *Nucl. Phys.*, B542:3–30, 1999.

[91] Anon. Super-Kamiokande Official Website, 2018.

[92] J. Timmer. The UA1 Detector. In *ANTI-PROTON PROTON PHYSICS AND THE W DISCOVERY. PROCEEDINGS, INTERNATIONAL COLLOQUIUM OF THE CNRS, 3RD MORIOND WORKSHOP, LA PLAGNE, FRANCE, MARCH 13-19, 1983*, pages 593–608, 1983.

[93] F. Vannucci. The NOMAD Experiment at CERN. *Adv. High Energy Phys.*, 2014:129694, 2014.

[94] S. Aoki et al. The T2K Side Muon Range Detector (SMRD). *Nucl. Instrum. Meth.*, A698:135–146, 2013.

[95] P.-A. Amaudruz et al. The T2K fine-grained detectors. *Nuclear Instruments and Methods in Physics Research Section A: Accelerators, Spectrometers, Detectors and Associated Equipment*, 696:1 – 31, 2012.

[96] R. Frühwirth. Application of kalman filtering to track and vertex fitting. *Nuclear Instruments and Methods in Physics Research Section A: Accelerators, Spectrometers, Detectors and Associated Equipment*, 262(2):444 – 450, 1987.

[97] N. Abgrall et al. Time Projection Chambers for the T2K Near Detectors. *Nucl. Instrum. Meth.*, A637:25–46, 2011.

[98] D. Allan et al. The Electromagnetic Calorimeter for the T2K Near Detector ND280. *JINST*, 8:P10019, 2013.

[99] S. Assylbekov et al. The T2K ND280 Off-Axis Pi-Zero Detector. *Nucl. Instrum. Meth.*, A686:48–63, 2012.

[100] R. Brun and F. Rademakers. ROOT: An object oriented data analysis framework. *Nucl. Instrum. Meth.*, A389:81–86, 1997.

[101] S. Agostinelli et al. GEANT4: A Simulation toolkit. *Nucl. Instrum. Meth.*, A506:250–303, 2003.

[102] K. Olchanski S Ritt, P. Amaudruz. MIDAS (Maximum Integration Data Acquisition System), 2001.

[103] David Axmark and Michael Widenius. Mysql introduction. *Linux J.*, 1999(67es), November 1999.

[104] Dave Shaw and Helen O'Keeffe. Mis-mapped channels in the ecal and methods used to rectify this issue, 2016.

[105] D. Beznosko, A. Bross, A. Dyshkant, A. Pla-Dalmau, and V. Rykalin. FNAL-NICADD extruded scintillator. *IEEE Symposium Conference Record Nuclear Science 2004*, 2005.

[106] Per Jonsson. Aging studies of the ND280 scintillator detectors , 2016.

[107] Caio Licciardi and Mauricio Barbi. Particle Identification with the Fine Grained Detectors, 2012.

[108] Daniel Scully. FGD Vertex Activity Diagrams, 2012.

[109] Yoshinari Hayato. Overview of neutrino-nucleus interactions, 2016.

[110] Omar Benhar, Patrick Huber, Camillo Mariani, and Davide Meloni. Neutrino–nucleus interactions and the determination of oscillation parameters. *Phys. Rept.*, 700:1–47, 2017.

[111] K. Abe et al. Measurement of the numu charged-current quasielastic cross section on carbon with the ND280 detector at T2K. *Phys. Rev.*, D92(11):112003, 2015.

[112] Omar Benhar and Adelchi Fabrocini. Two nucleon spectral function in infinite nuclear matter. *Phys. Rev.*, C62:034304, 2000.

[113] A. Bodek and J. L. Ritchie. Fermi-motion effects in deep-inelastic lepton scattering from nuclear targets. *Phys. Rev. D*, 23:1070–1091, Mar 1981.

[114] Melody Ravonel Anthony Hillairet, Justyna Lagoda. numu CC event selections in the ND280 tracker using Run 2+3+4, 2015.

[115] Maria-Gabriella Catanesi Lorenzo Magaletti. CC muon antineutrino event selection in the ND280 tracker using Run 5c anti-neutrino beam data, 2014.

[116] Andrea Longhin and Ajmi Ali. Double differential inclusive charged-current numu cross section in plastic using the ND280 tracker, 2018.

[117] Tomasz Golan, Cezary Juszczak, and Jan T. Sobczyk. Effects of final-state interactions in neutrino-nucleus interactions. *Phys. Rev. C*, 86:015505, Jul 2012.

[118] O. Buss, T. Gaitanos, K. Gallmeister, H. van Hees, M. Kaskulov, O. Lalakulich, A.B. Larionov, T. Leitner, J. Weil, and U. Mosel. Transport-theoretical description of nuclear reactions. *Physics Reports*, 512(1):1 – 124, 2012. Transport-theoretical Description of Nuclear Reactions.

[119] Joanna Zalipska. Simulating low momentum protons in Neut and NuWro, 2018.

[120] Mark Hartz. Constraining Flux and Cross Section Parameters with a Fit to ND280 Tracker NuMu, 2012.

[121] K.S. Kölbig and B. Schorr. A program package for the landau distribution. *Computer Physics Communications*, 31(1):97 – 111, 1984.

[122] T. Matulewicz. Quenching of scintillation in baf2 for light charged particles. *Nuclear Instruments and Methods in Physics Research Section A: Accelerators, Spectrometers, Detectors and Associated Equipment*, 325(1):365 – 366, 1993.